

**MEASUREMENT OF THE NEUTRINO MASS ORDERING
WITH 9.28 YEARS OF ICECUBE DEEPCORE DATA**

by

Maria Veronica Prado Rodriguez

A dissertation submitted in partial fulfillment of
the requirements for the degree of

Doctor of Philosophy

(Physics)

at the

UNIVERSITY OF WISCONSIN–MADISON

2024

Date of final oral examination: 05/24/2024

The dissertation is approved by the following members of the Final Oral Committee:

Francis Halzen, Gregory Breit Professor & Hilldale Professor, Department of Physics

Albrecht Karle, Professor, Department of Physics

Vernon Barger, Vilas Research Professor & Van Vleck Professor, Department of Physics

Jessica Cisewski-Kehe, Assistant Professor, Department of Statistics

ABSTRACT

Although the Standard Model is our current best theory for describing the building blocks of the universe, there are still several important questions that it does not answer. Some of these include: How does gravity, dark matter, and dark energy fit into the Standard Model? Why is the universe made up of more matter than anti-matter? More importantly for this work, the Standard Model predicts that neutrinos should be massless particles. However, with the discovery of neutrino oscillations, it was confirmed that neutrinos have non-zero mass. But why does this happen? To be able to answer this question, the ordering of the neutrino masses became a crucial piece of the puzzle as all theories and some experiments (e.g. neutrinoless double beta decay) depend greatly on whether the mass ordering is normal ($m_3 > m_2 > m_1$) or inverted ($m_2 > m_1 > m_3$). IceCube is an ice-Cherenkov neutrino detector deployed about 1.5 kilometers below the surface of the South Pole. Using DeepCore, a more densely instrumented volume of ice near the bottom of the detector, this work studies the neutrino mass ordering (NMO) through a measurement of the oscillation patterns of a 9.28-year sample of atmospheric neutrinos using a frequentist statistical analysis. A goal of this work is to deliver a more robust result of the mass ordering preference in comparison to the previous 3-year IceCube DeepCore measurement [40]. Furthermore, this work aims to provide a unique contribution in answering the mass ordering question through DeepCore's ability to produce a result that is both independent of the δ_{CP} phase (currently creating a tension in existing NMO results) and generated at neutrino energies greater than those observed by any other experiment. The analysis observes a preference for the normal ordering at $2\Delta\text{LLH}_{\text{NO-IO}} = -4.398$, leading to a disfavoring of the inverted ordering at a 93.7% exclusion level, or 1.86σ .

Table of Contents

| | |
|--|------------|
| Abstract | i |
| Table of Contents | ii |
| List of Figures | vii |
| List of Tables | xi |
| Acknowledgements | xii |
| 1 Introduction | 1 |
| 1.1 Discovery of the Neutrino | 1 |
| 1.2 Neutrinos in the Standard Model | 2 |
| 1.2.1 Questions Still Unanswered by the Standard Model | 2 |
| 1.3 Neutrino Oscillations | 5 |
| 1.3.1 Neutrino Oscillation Probability | 6 |
| 1.4 Neutrino Interactions | 9 |
| 1.4.1 Interaction Models | 10 |
| 1.4.1.1 Elastic and Quasi-Elastic | 10 |
| 1.4.1.2 Resonant | 11 |
| 1.4.1.3 Deep-Inelastic Scattering | 11 |
| 1.5 Matter Effects | 12 |

| | | |
|----------|---|-----------|
| 1.6 | Neutrino Oscillation Experiments | 14 |
| 1.6.1 | Atmospheric Neutrinos | 16 |
| 1.7 | Neutrino Mass Ordering | 19 |
| 1.8 | Status of Neutrino Oscillation Measurements | 22 |
| 2 | The IceCube Neutrino Observatory | 25 |
| 2.1 | The IceCube Array | 25 |
| 2.1.1 | The DeepCore Subarray | 25 |
| 2.1.2 | Digital Optical Modules | 26 |
| 2.2 | Event Detection in the Ice | 28 |
| 2.2.1 | Cherenkov Radiation | 29 |
| 2.2.2 | Event Signatures | 30 |
| 2.2.2.1 | Track-like Events | 30 |
| 2.2.2.2 | Cascade-like Events | 32 |
| 2.3 | Optical Ice Properties | 34 |
| 2.3.1 | Bulk Ice Properties | 34 |
| 2.3.2 | Hole Ice Properties | 35 |
| 3 | The Data Sample | 37 |
| 3.1 | Monte Carlo (MC) Simulation | 37 |
| 3.1.1 | Neutrino Events | 38 |
| 3.1.2 | Atmospheric Muon Background | 39 |
| 3.1.3 | Photon Propagation and Detector Response | 39 |
| 3.1.3.1 | Noise Hits | 40 |
| 3.2 | Data Processing | 40 |
| 3.2.1 | Event Trigger (Level 1) | 41 |
| 3.2.2 | Onsite Filter (Level 2) | 41 |
| 3.2.3 | Data-MC Agreement Cuts (Level 3) | 42 |

| | | |
|----------|---|-----------|
| 3.2.4 | Background Rejection BDTs (Level 4) | 43 |
| 3.2.5 | Corridor and Containment Muon Cuts (Level 5) | 44 |
| 3.2.6 | Pre-Reconstruction Checks (Level 6) | 45 |
| 3.3 | Reconstruction | 45 |
| 3.3.1 | Fast Low-Energy Reconstruction using CNNs (FLERCNN) | 46 |
| 3.3.1.1 | Convolutional Neural Networks (CNNs) | 47 |
| 3.3.1.2 | FLERCNN Training | 48 |
| 3.3.2 | FLERCNN Performance | 51 |
| 3.3.2.1 | Energy and Zenith Reconstruction | 51 |
| 3.3.2.2 | Particle Identification (PID) | 51 |
| 3.3.2.3 | Vertex Reconstruction and Muon Classification | 52 |
| 3.4 | Final Level Cuts | 53 |
| 3.4.1 | Low Resolution and Background Rejection Cuts | 54 |
| 3.4.2 | Default Energy and Zenith Cuts | 56 |
| 4 | Analysis of the Neutrino Mass Ordering | 57 |
| 4.1 | Premise of the Analysis | 57 |
| 4.2 | 9.28-Year Analysis Sample | 59 |
| 4.2.1 | Binning | 59 |
| 4.2.2 | MC Simulation Templates | 61 |
| 4.2.3 | Muon Template Smoothing | 63 |
| 4.3 | Uncertainties | 63 |
| 4.3.1 | Systematic Uncertainties | 64 |
| 4.3.1.1 | Atmospheric Neutrino Flux | 65 |
| 4.3.1.2 | Neutrino Cross-Section | 66 |
| 4.3.1.3 | Detector Properties | 67 |
| 4.3.2 | Oscillation and Normalization Uncertainties | 71 |
| 4.3.3 | Atmospheric Muon Uncertainties | 73 |

| | | |
|----------|---|------------|
| 4.4 | Test Statistic | 73 |
| 4.4.1 | Treatment of limited MC Statistics | 74 |
| 4.5 | Optimization | 75 |
| 4.6 | Parameter Impact | 77 |
| 4.6.1 | Systematic Impact Test | 77 |
| 4.6.2 | Barr Parameter Correlations Test | 82 |
| 5 | Gauging the Analysis Response | 87 |
| 5.1 | Inject-Recover Test | 87 |
| 5.2 | Parameter Ensemble Test | 88 |
| 5.3 | Ensemble Test | 92 |
| 6 | Sensitivity to the Neutrino Mass Ordering | 96 |
| 6.1 | Methodology | 96 |
| 6.1.1 | The Pseudotrial Method | 100 |
| 6.1.2 | The Asimov Method | 101 |
| 6.2 | Expected Sensitivity | 103 |
| 6.2.1 | Pseudotrial Distributions | 107 |
| 6.2.2 | δ_{CP} Dependence | 107 |
| 6.3 | Comparison to the 3-Year DeepCore Sensitivity | 107 |
| 7 | Blind Fit to the Data | 110 |
| 7.1 | Blind Fit Procedure | 110 |
| 7.2 | Blind Fit Results | 110 |
| 7.2.1 | Parameter and Bin-wise Pulls | 111 |
| 7.2.1.1 | Bin-wise Pulls Stop Condition | 114 |
| 7.2.2 | Goodness of Fit | 114 |
| 7.2.3 | Post Fit Data-MC Agreement | 115 |
| 7.2.4 | Unphysical Fit Check | 116 |

| | | |
|----------|--|------------|
| 8 | Analysis Results | 118 |
| 8.1 | Unblinding Procedure | 118 |
| 8.2 | Results | 122 |
| 9 | Conclusion and Outlook | 127 |
| A | Lowering the Analysis Energy Range | 129 |
| A.1 | MC Simulation Threshold | 129 |
| A.2 | Study on Cross-Section Systematics | 129 |
| B | Check on the Hypersurfaces | 132 |
| | Bibliography | 133 |

List of Figures

| | | |
|------|--|----|
| 1.1 | Standard Model of Particle Physics | 3 |
| 1.2 | Diagram of Neutrinoless Double Beta Decay | 4 |
| 1.3 | Neutrino oscillations diagram | 6 |
| 1.4 | Charged-Current and Neutral-Current Interactions | 9 |
| 1.5 | Neutrino Interaction Models | 10 |
| 1.6 | Resonant Interaction | 11 |
| 1.7 | Charge-Current Coherent Forward Scattering | 12 |
| 1.8 | Neutrino Oscillation Experiments | 15 |
| 1.9 | Cosmic Ray Interaction Particle Shower | 17 |
| 1.10 | Atmospheric Neutrino Flux at the South Pole Lab | 18 |
| 1.11 | Zenith Angle Definition | 19 |
| 1.12 | Seasonal Atmospheric Flux Dependence | 20 |
| 1.13 | Concept for Measuring Neutrino Mass | 21 |
| 1.14 | Neutrino Mass Ordering Diagram | 22 |
| 1.15 | Mass Ordering Preference by NOvA and T2K | 24 |
| 2.1 | Diagram of the IceCube Experiment | 26 |
| 2.2 | Diagram of the DeepCore Subarray | 27 |
| 2.3 | Diagram of a Digital Optical Module | 28 |
| 2.4 | Cherenkov Radiation Principle | 30 |
| 2.5 | DeepCore Event Topologies | 31 |

| | | |
|------|---|----|
| 2.6 | Muon Energy Loss in Ice | 32 |
| 2.7 | Veto Region for DeepCore | 33 |
| 2.8 | The Birefringence Ice Model | 35 |
| 2.9 | Hole Ice Optical Efficiency | 36 |
| 3.1 | FLERCNN Sample Processing Chain | 38 |
| 3.2 | FLERCNN Sample Processing Level Event Rates | 41 |
| 3.3 | Level 3 Data - MC Full Time Length Cut | 43 |
| 3.4 | Level 4 BDT Cuts | 44 |
| 3.5 | Architecture of the FLERCNN Model | 46 |
| 3.6 | FLERCNN Input Images | 48 |
| 3.7 | FLERCNN Input Strings | 49 |
| 3.8 | Channels in a CNN | 50 |
| 3.9 | Energy and Zenith FLERCNN Loss | 51 |
| 3.10 | Energy and Zenith Reconstruction Performance | 52 |
| 3.11 | Particle Identification Classifier Performance | 53 |
| 3.12 | FLERCNN Performance on the Radial Vertex and Muon Classifier | 54 |
| 3.13 | Final Level Muon BDT Performance | 55 |
| 4.1 | Matter-Enhanced Oscillation Probabilities for NO and IO | 58 |
| 4.2 | PID Distribution by Event Type | 61 |
| 4.3 | Analysis-Level MC Simulation Templates for NO and IO | 62 |
| 4.4 | True Energy and Zenith MC Template Assuming True NO | 62 |
| 4.5 | Atmospheric Muon Template With and Without a KDE Implementation | 64 |
| 4.6 | Pion and Kaon Production Barr Blocks | 65 |
| 4.7 | Relative Percentage Difference for the Axial Mass Parameters | 66 |
| 4.8 | Hypersurface Example | 69 |
| 4.9 | Hypersurfaces Reduced χ^2 /DOF 1D Distributions | 70 |

| | | |
|------|--|-----|
| 4.10 | Hypersurfaces Reduced χ^2 /DOF 3D Distributions | 71 |
| 4.11 | Preliminary Reference Earth Model | 72 |
| 4.12 | Optimized Bin-wise Event Difference of the NO and IO MC Templates | 76 |
| 4.13 | Optimized bin-wise LLH of the NO and IO MC Templates | 76 |
| 4.14 | Systematic Impact Test Procedure | 78 |
| 4.15 | Reference Sensitivity Across All Analysis Parameters | 79 |
| 4.16 | Systematic Impact Test Assuming True NO | 80 |
| 4.17 | Systematic Impact Test Assuming True IO | 81 |
| 4.18 | Barr Parameter Ensemble Test | 82 |
| 4.19 | Barr Parameter Correlations Test Procedure | 84 |
| 4.20 | Barr Parameter Correlations Test Sensitivity Mismodeling | 85 |
| 5.1 | Inject-Recover Test Outcome | 88 |
| 5.2 | Mass-Ordering-Octant Degeneracy Pattern | 89 |
| 5.3 | Parameter Ensemble Test Outcome for a Fit of the Same Ordering | 90 |
| 5.4 | Parameter Ensemble Test Outcome for a Fit of the Opposite Ordering | 91 |
| 5.5 | Ensemble Test Goodness of Fit Distributions | 92 |
| 5.6 | Ensemble Test Parameter Pulls | 93 |
| 5.7 | Best Fit Parameter Distributions for True NO | 94 |
| 5.8 | Best Fit Parameter Distributions for True IO | 94 |
| 5.9 | Parameter Correlations | 95 |
| 6.1 | NMO Analysis Procedure for MC Simulation | 98 |
| 6.2 | P-Value Calculation Example | 99 |
| 6.3 | 9.28-Year DeepCore NMO Median Sensitivity Projection | 104 |
| 6.4 | Three-Flavor Oscillation Probability | 105 |
| 6.5 | Opposite Ordering Fit Oscillation Probability Choices | 106 |
| 6.6 | Mass-Ordering-Octant Degeneracy Effect on the NMO Sensitivity | 106 |

| | | |
|-----|--|-----|
| 6.7 | Expected Pseudotrial $\Delta LL_{H_{IO-NO}}$ Distributions | 108 |
| 6.8 | Sensitivity Dependence on the δ_{CP} Parameter | 109 |
| 6.9 | DeepCore NMO Sensitivity Comparison to the 3-Year Analysis | 109 |
| 7.1 | Best Fit Pulls on the Real Data | 112 |
| 7.2 | Best Fit 2D Bin-wise Pulls | 113 |
| 7.3 | Best Fit 1D Bin-wise Pulls | 113 |
| 7.4 | Goodness of Fit Test on the Real Data | 115 |
| 7.5 | Post Fit Data-MC Agreement | 116 |
| 7.6 | Data-MC Distribution Around the Zenith Outlier Bin | 117 |
| 8.1 | NMO Unblinding Procedure | 119 |
| 8.2 | NMO Analysis Results | 122 |
| 8.3 | NMO Results LLH Scan in $\sin^2(\theta_{23})$ | 123 |
| 8.4 | Hypothetical Observed Value at the Median of the NO Best Fit | 125 |
| A.1 | Unsimulated Events Expected from Lowering the Energy | 130 |
| A.2 | Relative Percentage Difference for Bodek-Yang variables | 131 |

List of Tables

| | | |
|-----|--|-----|
| 1.1 | Neutrino Oscillation Parameters Global Fit | 23 |
| 3.1 | Final Level Cuts | 56 |
| 4.1 | 9.28-Year NMO Analysis Expected Event Rate | 63 |
| 4.2 | Convolutd LLH Metric Check | 75 |
| 4.3 | NMO Analysis Parameters | 86 |
| 6.1 | Conversion of CL to Significance | 100 |
| 7.1 | Blind Fit Procedure | 111 |
| 7.2 | Best Fit Distance to the Nearest Boundary | 112 |
| 8.1 | NO and IO Parameter Value Best Fits to the Real Data | 124 |
| 8.2 | Comparison of the 3-Year and 9.28-Year Results | 125 |

Acknowledgements

God's way is unerring; the LORD's promise is tried and true; he is a shield for all who trust in him. Truly, who is God except the LORD? Who but our God is the rock? This God who girded me with might, kept my way unerring. Who made my feet swift as a deer's, set me safe on the heights. Who trained my hands for war, my arms to bend even a bow of bronze. You have given me your protecting shield, and your help has made me great.

— SONG OF THANKSGIVING [2 SAM. 22:31-36]

What a journey it has been! From the day that I stepped foot in my first high school physics class, I knew that this is what I wanted to do. I wanted to get a PhD in physics. And just like that, this became one of my lifelong dreams ... *contra viento y marea*. Thanks to this dream, I have had the opportunity to travel to so many places and to meet so many incredible people along the way. From my time at Williams, to my time at Kansas State and Chicago. And then came Madison. Thank you thank you to everyone who helped me achieve this dream.

My biggest thank you is raised to God and Mother Mary. Without my faith, without this rock, I would not be here today.

Thank you to my incredible parents. Mom and dad, you have given me strength in moments where I could not find any myself. You have listened to me, consoled me, fought alongside of me, and cheered me. You are my biggest treasure. I truly could not have been

given a more loving, caring, and compassionate mom and dad. It is the greatest honor to be your daughter.

Thank you abuela Nena. You left me for heaven just a few months ago and took a piece of me with you. Thank you for being both my grandmother and my great friend. Thank you for your infinite love, encouragement, and wisdom. Thank you for all the laughs and for your great desire to live life to the fullest. You wanted so badly to see me graduate. I hope you have a big party in heaven for me the day of my graduation. I will love you forever.

Thank you my sweet Harper. From the moment you were born into this world, you have brought me so much joy and love. Your beautiful presence alone provided me an escape whenever this PhD became difficult. I feel so blessed to be your auntie and godmother.

Thank you Lisa. My great mentor and friend. Thank you for being a role model to me. Thank you for caring so much about me. You have guided me through every step of this PhD and cheered me on from the sidelines. I am so grateful to have met someone as amazing as you at UW.

Thank you Mr. Rose, thank you Larry, and thank you Charlie. You were my best physics professors in high school and college. You believed in me from the very beginning and always encouraged me to keep going. You gave me confidence and made me love physics even more. I cannot thank you enough for everything you did for me.

Thank you Jamie for connecting with me through APS and becoming one of my greatest mentors. I am so thankful for all of your encouragement and support throughout these years. Thank you for always believing in me.

Thank you Ava, Marina, and Joanna. My dearest friends. You have been through this journey with me from the very beginning, each from thousands of miles away. And yet, despite the physical distance, you have each been among my greatest supporters. Thank you for all of your love.

Thank you Nora and Jeff. Thank you for being a part of my journey in IceCube. Thank you for your invaluable friendship and support. Thank you for always making me laugh and for standing by me through difficult times.

And last but not least, thank you Francis. Thank you for meeting with me that first day at the Discovery Building and hearing my pitch as to why I wanted to join IceCube. You were so gracious with me from the very beginning and supported me every step of the way, even during uncertain times when I found myself without an advisor. Thank you for giving me the opportunity to live out my dreams.

*Mi Nenita, mi segunda mamá.
Siempre serás la luz que ilumine mi camino.
Esta tesis te la dedico a ti.*

Chapter 1

Introduction

1.1 Discovery of the Neutrino

An exciting new theory took the world by storm in 1930— one that proposed the existence of a brand new particle in the universe. This particle would, later on, become known as the *neutrino*, or "little neutral one". During this time, Austrian physicist, Wolfgang Pauli, was trying to explain what seemed to be a violation of conservation of energy and momentum in beta decay [4]. Beta decay was thought of, at the time, as a process where a neutron at rest decays into a proton and ejects an electron. The electron, then, is expected to have one well-defined energy value. However, this is not what was measured [5; 49]. Instead, a continuous spectrum of electron energies were found, leading to the question: "Could it be that energy and momentum are not conserved?" As a result, Pauli proposed a theory where a third, extremely light, and electrically neutral particle carried the missing energy, which would explain why this particle had not been detected. The existence of the neutrino was experimentally confirmed in 1956 by Clyde Cowan and Frederick Reines [64].

1.2 Neutrinos in the Standard Model

Neutrinos are elementary particles found in the Standard Model of Particle Physics. The Standard Model describes to extreme precision the behavior and properties of elementary particles in our universe. The word *elementary* here means that these particles cannot be subdivided further into other particles.

Particles in the Standard Model are classified into two categories: Fermions and Bosons. Elementary fermions are the foundation of matter that is observable and consist of spin $1/2$. Elementary bosons, on the other hand, act as force carriers, mediating the forces that act on fermions, and have integer spin.

The Standard Model is made up of five force carriers that give rise to the electromagnetic, weak, and strong forces of nature. Fermions are subdivided into quarks and leptons according to their interactions with force carriers. Quarks interact with all forces, while leptons do not interact with the strong force. Neutrinos are leptons that do not interact with the electromagnetic force as they have neutral charge. The Higgs particle gives rise to the mass acquired by the W and Z bosons and well as the charged fermions. Both the gluon and the photon do not interact with the Higgs, and as a result, are massless.

Figure 1.1 shows the particles that make up the Standard Model as well as their respective anti-particles. An anti-particle has the same mass and spin as its corresponding particle, but it has opposite charge and, for leptons, opposite lepton number. These are produced in different processes of nature such as beta decay and cosmic ray interactions.

1.2.1 Questions Still Unanswered by the Standard Model

Although the Standard Model is our current best theory for describing the building blocks of the universe, there are still several important questions that it does not answer. Some of these include: How does gravity, dark matter, and dark energy fit into the Standard Model? Why is the universe made up of more matter than anti-matter?

Standard Model of Elementary Particles

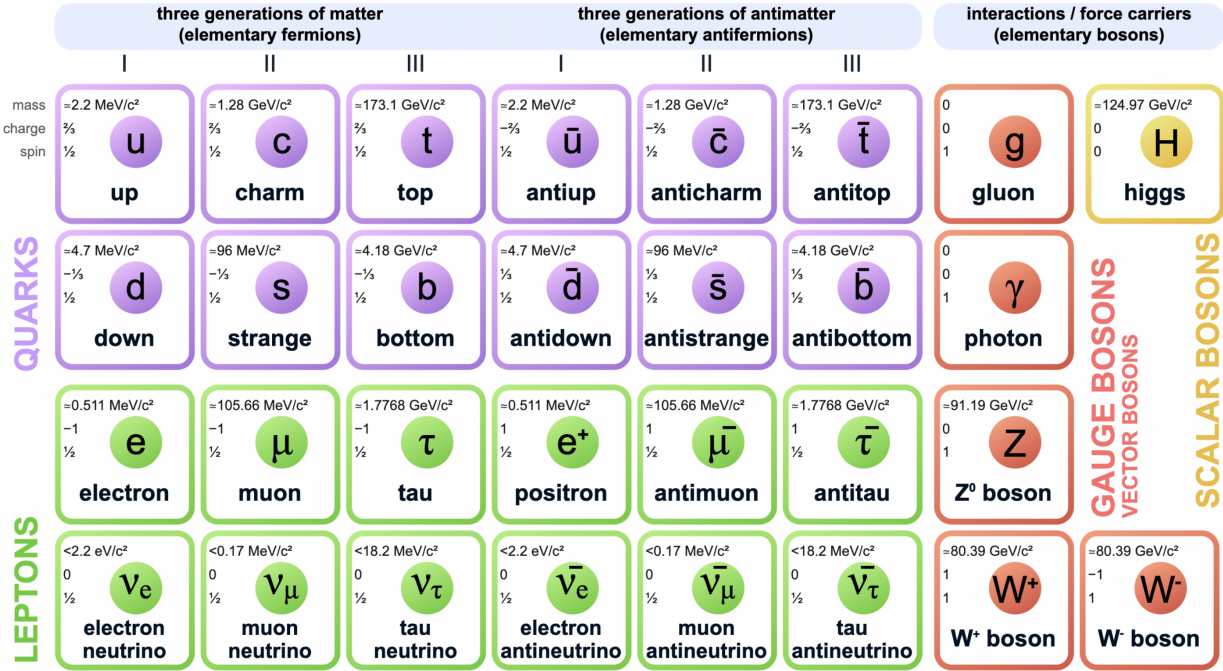


Figure 1.1: Standard Model of Particle Physics showing all experimentally confirmed elementary particles as well as their anti-particles (Public Domain). The mass, charge, and spin are also shown.

More importantly for this work, the Standard Model predicts that neutrinos should be massless particles. This arises from a particle's *chirality*. Chirality is an intrinsic quantum property that describes the handedness of a particle. While quarks and charged leptons can be found as both chiral right-handed and left-handed in the Standard Model, neutrinos can only be found as left-handed and anti-neutrinos as right-handed. This happens as a result of neutrinos only interacting with the weak force, which by nature, does not interact with right-handed particles or left-handed anti-particles.

For a particle in the Standard Model to acquire mass, it must interact with the Higgs field. This occurs by means of an interaction between the chiral right-handed particle, its left-handed component, and the Higgs. From this, it follows that, for a left-handed neutrino to acquire mass, a right-handed neutrino needs to exist. However, this is not what the Standard Model shows, and as a result, neutrinos were predicted to be massless.

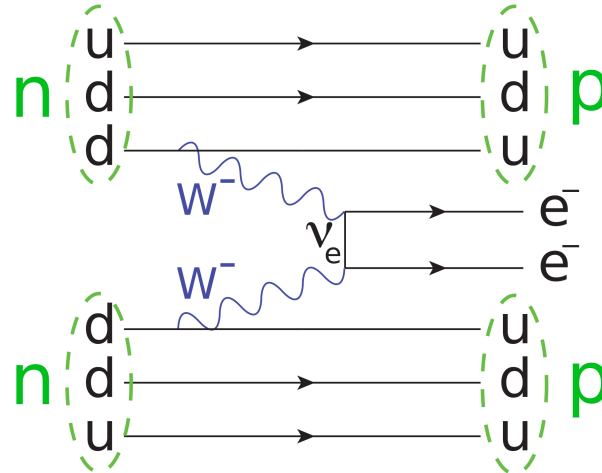


Figure 1.2: Diagram of the hypothesized neutrinoless double beta decay process, where the neutrino is its own anti-particle, and as such, gets absorbed [62].

Nevertheless, in 1998 and separately in 2001, it was confirmed by the Super-Kamiokande experiment [38] and by the Sudbury Neutrino Observatory (SNO) [33], respectively, that at least two out of the three neutrinos have non-zero mass. This occurs due to a phenomenon called neutrino oscillations, and will be further discussed in Section 1.3.

There are several theories that describe how it is possible that neutrinos can have non-zero mass. One of these theories proposes that the anti-neutrino is actually the chiral right-handed version of the neutrino, and therefore, the neutrino is its own anti-particle. Particles that are its own anti-particle are called *Majorana* particles. There are several experiments currently looking for this through a process called neutrinoless double beta decay [47]. Double beta decay is the process of a nucleus decaying through a double neutron decay into two protons along with a double emission of electrons and anti-neutrinos. If the neutrino is Majorana and exists as both right and left-handed, there would be a detection channel where no neutrinos are emitted as shown in Figure 1.2.

1.3 Neutrino Oscillations

Neutrinos exist in two bases—the flavor basis and the mass basis. Flavor and mass states are related through the Pontecorvo–Maki–Nakagawa–Sakata (PMNS) unitary mixing matrix as shown in Equation 1.1, and hence, the properties of mass and flavor are not independent. There are three flavors of neutrinos in the Standard Model, ν_e, ν_μ , and ν_τ . Likewise, there are three mass states, ν_1, ν_2 , and ν_3 .

$$\begin{pmatrix} \nu_e \\ \nu_\mu \\ \nu_\tau \end{pmatrix} = \begin{pmatrix} U_{e1} & U_{e2} & U_{e3} \\ U_{\mu1} & U_{\mu2} & U_{\mu3} \\ U_{\tau1} & U_{\tau2} & U_{\tau3} \end{pmatrix} \begin{pmatrix} \nu_1 \\ \nu_2 \\ \nu_3 \end{pmatrix} \quad (1.1)$$

Each flavor state is a unique mixture of the different mass states, and similarly, each mass state is a unique mixture of the different flavor states. Specifically, each is a linear superposition of the other as shown in Equation 1.2 where $\alpha \in \{e, \mu, \tau\}$ and $i \in \{1, 2, 3\}$.

$$\begin{aligned} |\nu_\alpha\rangle &= \sum_i U_{\alpha i} |\nu_i\rangle \\ |\nu_i\rangle &= \sum_\alpha U_{\alpha i}^* |\nu_\alpha\rangle \end{aligned} \quad (1.2)$$

The elements of the PMNS matrix are parametrized by three mixing angles, θ_{12}, θ_{13} , and θ_{23} , as well as one complex phase, δ_{CP} , in the following way

$$U_{PMNS} = \begin{pmatrix} 1 & 0 & 0 \\ 0 & c_{23} & s_{23} \\ 0 & -s_{23} & c_{23} \end{pmatrix} \times \begin{pmatrix} c_{13} & 0 & s_{13}e^{-i\delta_{\text{CP}}} \\ 0 & 1 & 0 \\ -s_{13}e^{i\delta_{\text{CP}}} & 0 & c_{13} \end{pmatrix} \times \begin{pmatrix} c_{12} & s_{12} & 0 \\ -s_{12} & c_{12} & 0 \\ 0 & 0 & 1 \end{pmatrix} \quad (1.3)$$

where $c_{ij} = \cos(\theta_{ij})$ and $s_{ij} = \sin(\theta_{ij})$.

Neutrinos propagate through space and time in the mass basis but interact with matter in the flavor basis. As such, neutrinos with different mass will propagate at different

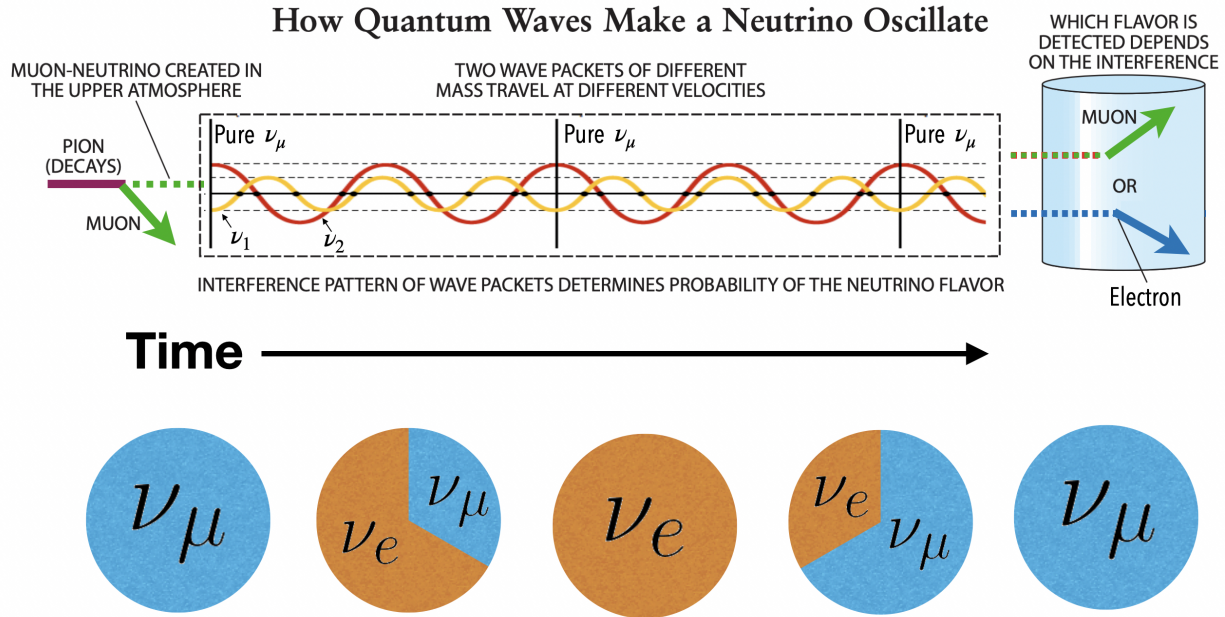


Figure 1.3: Diagram showing the concept of neutrino oscillations for the simplified case of two neutrino flavors (diagram modified from [51]). The pie charts on the bottom of the diagram show a depiction of changing probabilities when detecting one neutrino flavor or another as a function of time.

velocities, and as a result, their wavepackets can interfere with one another. This interference between the mass states leads to changes in the mixture of the flavor states. In other words, the probability of detecting one flavor of neutrino or another changes periodically as a function of time. This phenomenon is called *neutrino oscillations*. Figure 1.3 shows a diagram depicting this phenomenon for two neutrinos for simplicity.

1.3.1 Neutrino Oscillation Probability

Mass states are described by plane wave solutions such that

$$|v_j\rangle = e^{-i(E_j t - \vec{p}_j \cdot \vec{x})} |v_j\rangle_{t=0} \quad (1.4)$$

where $|v_j\rangle$ is the time-dependent mass state. E_j , p_j , and x are the energy, momentum, and position of the mass state, respectively, and t is the time elapsed since the mass state was first produced.

From Equation 1.2, it follows that

$$|v_\alpha\rangle = \sum_j U_{\alpha j} e^{-i(E_j t - \vec{p}_j \cdot \vec{x})} |v_j\rangle_{t=0}. \quad (1.5)$$

Since neutrinos are ultrarelativistic and near-massless, we can approximate $p \gg m$ and $p \simeq E$. This yields

$$E_j = \sqrt{p_j^2 + m_j^2} \approx E + \frac{m_j^2}{2E} \quad (1.6)$$

where m_j is the mass of the given mass state and E is the energy of the neutrino at the point of interaction. Dropping the phase factors which have no effect on the observables,

$$|v_\alpha\rangle = \sum_j U_{\alpha j} e^{-i\left(\frac{m_j^2 t}{2E}\right)} |v_j\rangle_{t=0}. \quad (1.7)$$

The probability that a neutrino with flavor α oscillates to flavor β after time t is

$$\begin{aligned} P_{\nu_\alpha \rightarrow \nu_\beta} &= |\langle v_\beta(t) | v_\alpha(0) \rangle|^2 \\ &= \left| \left(\sum_j U_{\beta j}^* e^{i\left(\frac{m_j^2 t}{2E}\right)} \langle v_j(0) | \right) \left(\sum_i U_{\alpha i} |v_i(0)\rangle \right) \right|^2 \\ &= \left| \sum_j U_{\beta j}^* U_{\alpha j} e^{i\left(\frac{m_j^2 L}{2E}\right)} \right|^2 \\ &= \sum_{i,j} U_{\alpha i}^* U_{\beta i} U_{\alpha j} U_{\beta j} e^{-i\left(\frac{(m_i^2 - m_j^2)L}{2E}\right)} \\ &= \sum_{i,j} U_{\alpha i}^* U_{\beta i} U_{\alpha j} U_{\beta j} e^{-i\left(\frac{\Delta m_{ij}^2 L}{2E}\right)} \end{aligned} \quad (1.8)$$

where we approximate $t \approx L$, the neutrino flight length, using natural units ($\hbar = c = 1$). After applying Euler's formula, we arrive at the standard equation for neutrino oscillation probability

$$\begin{aligned}
P_{\alpha \rightarrow \beta} = & \delta_{\alpha\beta} - 4 \sum_{i>j} \text{Re}[U_{\alpha i}^* U_{\beta i} U_{\alpha j} U_{\beta j}^*] \sin^2 \left(\frac{\Delta m_{ij}^2 L}{4E_\nu} \right) \\
& + 2 \sum_{i>j} \text{Im}[U_{\alpha i}^* U_{\beta i} U_{\alpha j} U_{\beta j}^*] \sin \left(\frac{\Delta m_{ij}^2 L}{2E_\nu} \right)
\end{aligned} \tag{1.9}$$

where L is the neutrino flight length, E_ν is the neutrino energy, and $\Delta m_{ij}^2 = m_i^2 - m_j^2$ is the *mass splitting* for mass states i and j . To better understand the significance and role of the neutrino oscillation parameters, we can think about the two-neutrino case for simplicity. For two neutrinos, the PMNS matrix reduces to

$$\begin{pmatrix} \nu_\alpha \\ \nu_\beta \end{pmatrix} = \begin{pmatrix} \cos(\theta) & \sin(\theta) \\ -\sin(\theta) & \cos(\theta) \end{pmatrix} \begin{pmatrix} \nu_i \\ \nu_j \end{pmatrix} \tag{1.10}$$

yielding an oscillation probability of

$$P_{\nu_\alpha \rightarrow \nu_\beta} = \sin^2(2\theta) \sin^2 \left(\frac{\Delta m_{ij}^2 L}{4E_\nu} \right) \tag{1.11}$$

where $\sin^2(2\theta)$ is the amplitude of the oscillation, Δm_{ij}^2 is inversely proportional to the wavelength of the oscillation, and L/E_ν is the *baseline*. Generally, the baseline is the independent variable that is controlled by experiments probing the different mixing angles, mass splitting values, and the δ_{CP} phase. Adding back in the c and \hbar values to Equation 1.11, we obtain

$$\frac{\Delta(m_{ij}c^2)^2 L}{4\hbar c E_\nu} \approx 1.27 \times \frac{\Delta m_{ij}^2 [\text{eV}^2] L [\text{km}]}{E_\nu [\text{GeV}]} \tag{1.12}$$

$$P_{\nu_\alpha \rightarrow \nu_\beta} = \sin^2(2\theta) \sin^2 \left(1.27 \frac{\Delta m_{ij}^2 L}{E_\nu} \right) \tag{1.13}$$

with Δm_{ij}^2 , L , and E_ν having experimentally practical units of eV^2 , km , and GeV , respec-

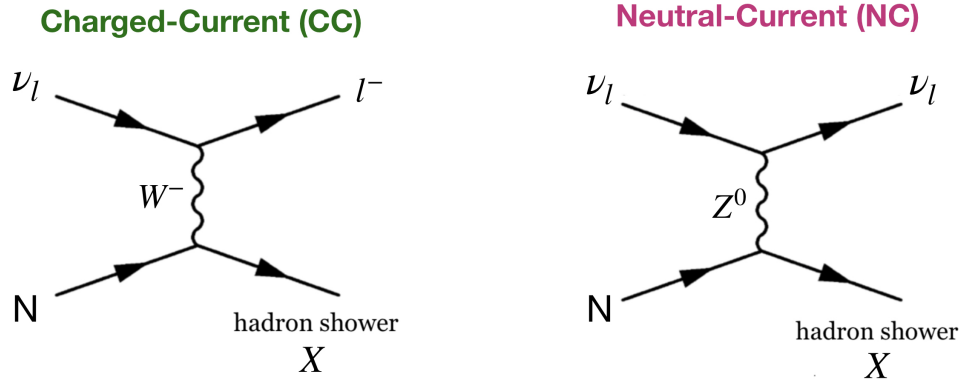


Figure 1.4: Example of possible Feynman diagrams of CC and NC interactions. CC interactions are mediated by a charged W^\pm boson while NC interactions are mediated by a neutral Z^0 boson.

tively.

Moreover, we can now take a step back and understand why observing the phenomenon of neutrino oscillations meant that neutrinos must have non-zero mass. From Equation 1.11, we can see that if neutrinos were massless, $\Delta m_{ij}^2 = 0$, and, hence, the oscillation probability would be zero. This means that neutrinos would never change flavors, but instead, remain as the flavor they were in at the time of their production.

1.4 Neutrino Interactions

There are two main channels for neutrinos to interact with matter. These are called charged-current (CC) and neutral-current (NC) interactions. CC interactions are mediated by a charged W^\pm boson and, as a result, produce a charged lepton of the corresponding neutrino flavor in the final state of the interaction. Meanwhile, NC interactions are mediated by a neutral Z^0 boson and, thus, produce a neutrino of the same initial flavor. Figure 1.4 shows possible Feynman diagrams depicting these two interactions.

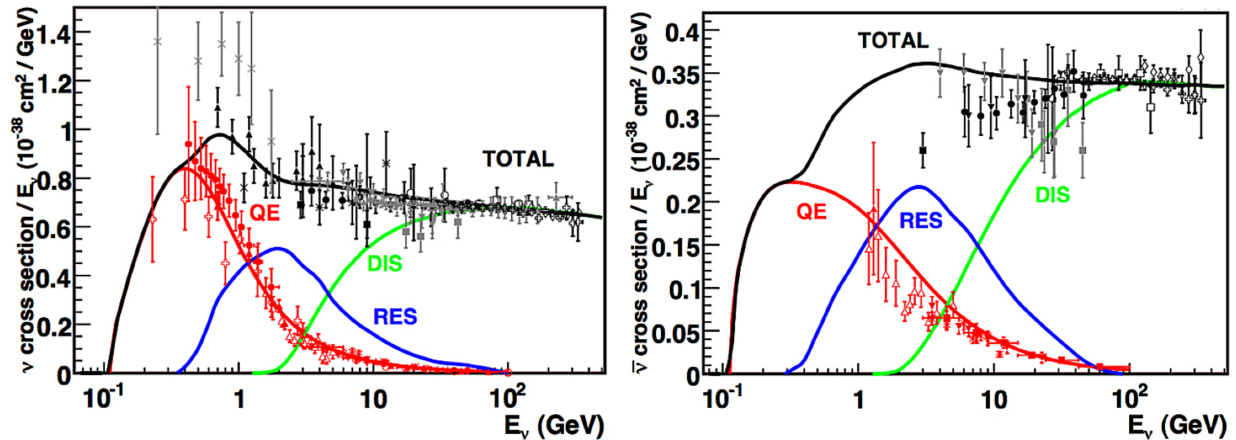


Figure 1.5: Neutrino interaction model cross-section as a function of neutrino energy for neutrinos (left) and anti-neutrinos (right) [24]. QE stands for Quasi-Elastic processes, RES for resonant processes, and DIS for deep-inelastic scattering processes.

1.4.1 Interaction Models

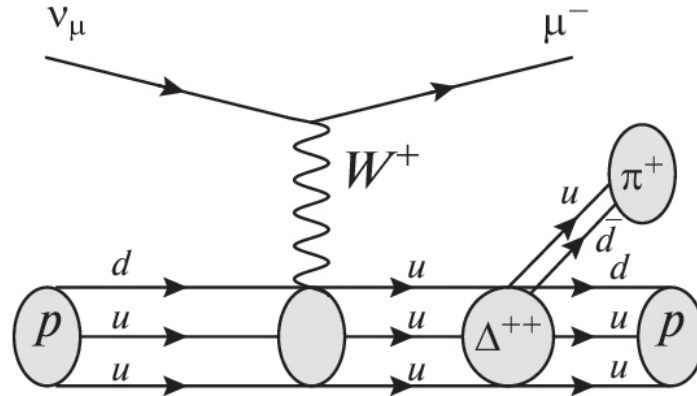
Depending on the strength of the interaction, CC and NC processes can be classified into a few different categories. The three most relevant of these for this work are Elastic/Quasi-Elastic (QE), Resonant (RES), and Deep-Inelastic Scattering (DIS). Figure 1.5 shows the cross-section as a function of neutrino energy for each of these interaction models for neutrinos and anti-neutrinos. As can be seen in the plots, neutrino cross-sections are roughly two times larger than anti-neutrino cross-sections. This feature plays an important role for this work and will be further discussed in Chapter 4.

1.4.1.1 Elastic and Quasi-Elastic

Elastic and quasi-elastic interactions dominate at neutrino energies of about 100 MeV to 1 GeV where a neutrino scatters off of either a nucleus or an electron. In the former, one or more nucleons get freed as a result of the scattering.

Quasi-elastic scattering occurs for CC processes that involve a neutrino interacting with a *nucleus*. Elastic scattering occurs for all NC processes (*nuclei and electron scattering*) as well as CC processes that involve an *electron* neutrino scattering off of an electron. Neutrino-electron scattering is also referred to as *coherent forward scattering*, and, specifically, CC

Figure 1.6: Feynman diagram of one type of resonant neutrino scattering [22]. In this example, a muon neutrino interacts with a proton through a W^+ exchange to produce a delta resonance and muon. The delta resonance then decays to a proton and a pion.



electron scattering gives rise to matter effects in the neutrino oscillation probabilities. This will be further discussed in Section 1.5.

1.4.1.2 Resonant

Resonant interactions dominate for neutrino energies of about 1 GeV to 10 GeV. In resonant scattering, a neutrino excites a nucleus to produce a delta resonance which then decays into a nucleon and a pion. A charged lepton or neutrino is also produced in the final state of the interaction. As such, these processes can occur in both CC or NC channels. Figure 1.6 shows one possible Feynman diagram for resonant scattering.

1.4.1.3 Deep-Inelastic Scattering

Deep-inelastic scattering dominates at neutrino energies above 10 GeV. These processes are energetic enough for the neutrino to penetrate all the way to the quark-level of the nucleus. In this case, a hadronic shower is produced in the final state of the interaction along with a charged lepton or a neutrino. Hadronic showers are composed of particles that are made up of quarks such as protons, neutrons, pions, and kaons. Similarly to resonant interactions, deep-inelastic scattering can occur in both CC and NC channels.

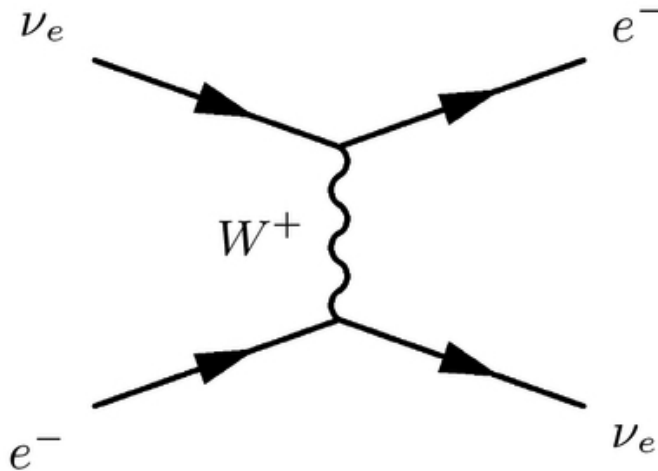


Figure 1.7: Feynman diagram for CC coherent forward scattering [46]. This type of scattering only occurs for electron neutrinos and, as such, breaks the flavor symmetry in the neutrino Hamiltonian.

1.5 Matter Effects

As was briefly mentioned in Section 1.4, neutrinos can undergo coherent forward scattering with electrons in matter. Although electron scattering can occur in both CC and NC processes, only neutrinos with an electron flavor can interact through CC as shown in the Feynman diagram in Figure 1.7. As such, this potential is enhanced for electron-flavored neutrinos only, creating an asymmetry in the Hamiltonian that makes mass states more "electron neutrino". The Hamiltonian is then modified such that

$$H_{matter} = H_{vacuum} + U_{PMNS}^\dagger \begin{pmatrix} V_e & 0 & 0 \\ 0 & 0 & 0 \\ 0 & 0 & 0 \end{pmatrix} U_{PMNS} \quad (1.14)$$

where H_{matter} and H_{vacuum} are in the mass basis, V_e is the electron neutrino potential contribution from CC coherent forward scattering in the flavor basis, and U_{PMNS} is the PMNS rotation matrix that converts the flavor basis to the mass basis. V_e is

$$V_e(\vec{x}) = \pm\sqrt{2}G_f N_e(\vec{x}) \quad (1.15)$$

where G_f is the Fermi Constant and $N_e(\vec{x})$ is the electron density as a function of the neutrino position. V_e is positive for neutrinos and negative for anti-neutrinos.

To understand the effects of this process on neutrino oscillation probabilities, we can look at the two-flavor case for simplicity. For two flavors, Equation 1.14 reduces to

$$H_{matter} = \frac{1}{2E} \begin{pmatrix} m_1^2 & 0 \\ 0 & m_2^2 \end{pmatrix} + \begin{pmatrix} \cos(\theta) & -\sin(\theta) \\ \sin(\theta) & \cos(\theta) \end{pmatrix} \begin{pmatrix} V_e & 0 \\ 0 & 0 \end{pmatrix} \begin{pmatrix} \cos(\theta) & \sin(\theta) \\ -\sin(\theta) & \cos(\theta) \end{pmatrix} \quad (1.16)$$

$$= \begin{pmatrix} \frac{m_1^2}{2E} + V_e \cos^2(\theta) & V_e \sin(\theta) \cos(\theta) \\ V_e \sin(\theta) \cos(\theta) & \frac{m_2^2}{2E} + V_e \sin^2(\theta) \end{pmatrix} \quad (1.17)$$

where H is now non-diagonal. This indicates that the mass states of H_{matter} are not the usual neutrino mass states but rather *effective* mass states. Effective mass states lead to an effective PMNS matrix, and hence, effective mixing angles and mass splittings. The process of matter enhancing the neutrino oscillation parameters as a result of coherent forward scattering is called the Mikheyev–Smirnov–Wolfenstein (MSW) effect, or "matter effects".

Consequently, Equation 1.11, then, becomes

$$P_{\nu_\alpha \rightarrow \nu_\beta}(t) = \sin^2(2\theta_{eff}) \sin^2\left(\frac{\Delta m_{eff}^2 L}{4E_\nu}\right) \quad (1.18)$$

where

$$\begin{aligned} \sin(2\theta_{eff}) &= \frac{\sin(2\theta)}{C} \\ \Delta m_{eff}^2 &= C\Delta m^2 \end{aligned} \quad (1.19)$$

with

$$C = \sqrt{(\cos(2\theta) - A)^2 + \sin^2(2\theta)} \quad (1.20)$$

and

$$A = \frac{2V_e E}{\Delta m^2} = \pm \frac{2\sqrt{2}G_f N_e E}{\Delta m^2}. \quad (1.21)$$

We can see from Equation 1.18 that matter effects are maximal when $\sin(2\theta_{eff}) = 1$. We can now solve for the neutrino energy in this case using Equation 1.19 where we obtain

$$E = \pm \frac{\Delta m^2}{2\sqrt{2}G_f N_e} \cos(2\theta). \quad (1.22)$$

As neutrino energy is only allowed to be a positive quantity, we see from Equation 1.22 that **matter effects are resonant only for neutrinos (+) when Δm^2 is positive and for anti-neutrinos (-) when Δm^2 is negative**. This concept becomes extremely important for this work and will be discussed further in Chapter 4.

1.6 Neutrino Oscillation Experiments

Throughout the years, experiments have been built to probe the different neutrino oscillation parameters. By adjusting the placement of their detector with respect to the energy of the incident neutrino, E_ν , experiments can control the oscillation baseline in Equation 1.9 to measure the PMNS mixing angles, mass splittings, and phase. Figure 1.8 shows different neutrino oscillation experiments as well as where these lie with respect to the oscillation baseline parameter space. The dashed and dotted-dashed diagonal lines show the baselines sensitive to measuring Δm_{21}^2 and Δm_{32}^2 , respectively.

Neutrino oscillation experiments are categorized according to the neutrino-production process that they use since this determines the energy of the incident neutrino flux. The four kinds of neutrino oscillation experiments are *solar*, *reactor*, *accelerator*, and *atmospheric*.

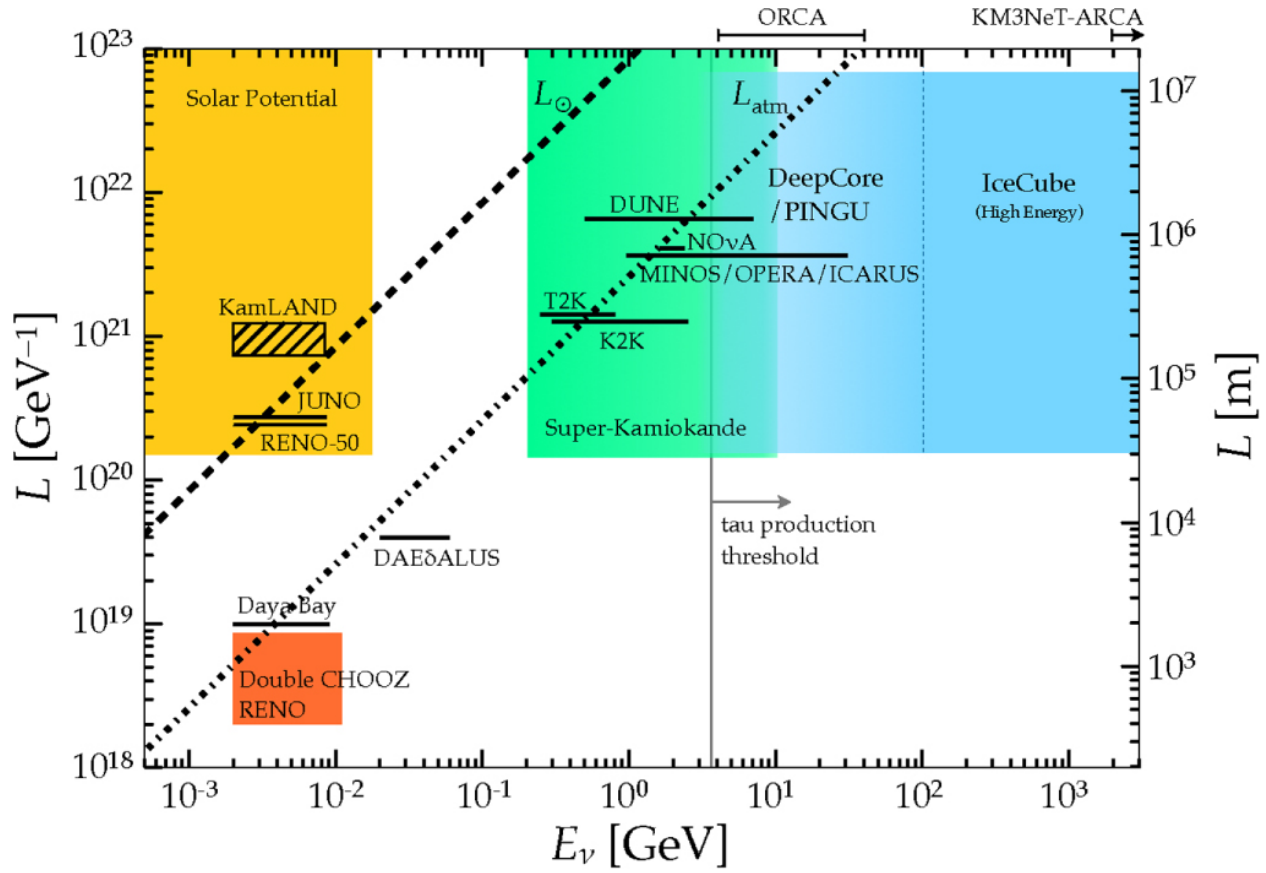


Figure 1.8: Neutrino oscillation experiments with respect to the oscillation baseline parameter space [29]. The dashed and dotted-dashed diagonal lines show the baselines sensitive to measuring Δm_{21}^2 and Δm_{32}^2 , respectively.

Equation 1.23 shows the types of experiments that can probe each different PMNS mixing angle as well as the phase.

$$U_{PMNS} = \begin{matrix} \text{atmospheric and} \\ \text{accelerators} \end{matrix} \begin{matrix} \text{reactor and accelerators} \\ \text{solar and reactors} \end{matrix} \quad (1.23)$$

$$U_{PMNS} = \begin{pmatrix} 1 & 0 & 0 \\ 0 & c_{23} & s_{23} \\ 0 & -s_{23} & c_{23} \end{pmatrix} \times \begin{pmatrix} c_{13} & 0 & s_{13}e^{-i\delta_{CP}} \\ 0 & 1 & 0 \\ -s_{13}e^{i\delta_{CP}} & 0 & c_{13} \end{pmatrix} \times \begin{pmatrix} c_{12} & s_{12} & 0 \\ -s_{12} & c_{12} & 0 \\ 0 & 0 & 1 \end{pmatrix}$$

Solar neutrino experiments rely on a naturally-sourced electron neutrino production from fusion and decay processes inside the Sun. On the contrary, reactor and accelerator

neutrino experiments produce their own artificial neutrino flux. For nuclear reactors, beta decay from fission creates an electron anti-neutrino flux while, for accelerator experiments, protons are smashed onto a fixed target where they produce showers of hadrons that decay to mostly muon neutrinos and anti-neutrinos. Atmospheric neutrino experiments rely on a naturally-sourced neutrino flux coming from cosmic rays in the Earth's atmosphere. This type of neutrino production is the most important for this work and will be discussed in further detail in what follows.

1.6.1 Atmospheric Neutrinos

Primary cosmic rays—highly energetic protons and nuclei from outside of the Solar System—collide with the Earth's atmosphere. This interaction produces showers of hadrons that include pions and kaons. The pions and kaons then decay to an array of muons and electrons as well as muon-flavored and electron-flavored neutrinos and anti-neutrinos as shown in Figure 1.9. In this sketch, a cosmic ray proton collision with the Earth's atmosphere produces a shower of charged and neutral pions as well as a neutron particle. The dominant source of atmospheric neutrino production is from charged pions which decay in the following way

$$\pi^+ \rightarrow \mu^+ + \nu_\mu \quad (1.24)$$

$$\mu^+ \rightarrow e^+ + \nu_e + \bar{\nu}_\mu \quad (1.25)$$

$$\pi^- \rightarrow \mu^- + \bar{\nu}_\mu \quad (1.26)$$

$$\mu^- \rightarrow e^- + \bar{\nu}_e + \nu_\mu \quad (1.27)$$

yielding two muon-flavored neutrinos and one electron-flavored neutrino. Figure 1.10 shows the atmospheric neutrino flux as a function of both neutrino energy and $\cos(\theta_{zenith})$ as it is expected at the South Pole Lab (SPL)—the relevant neutrino detector for this

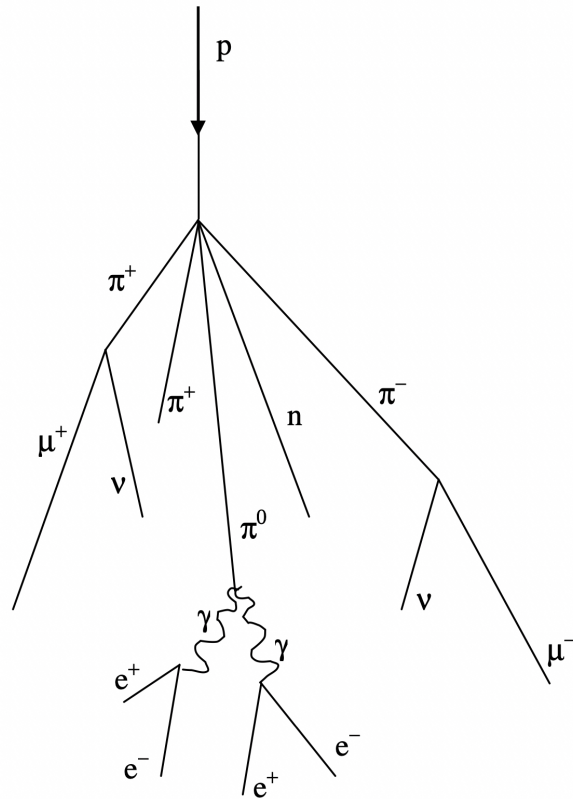


Figure 1.9: Primary cosmic ray hadronic shower produced from interactions with the Earth's atmosphere [7].

work. Note that there is a greater presence of neutrinos than anti-neutrinos in the flux. Moreover, neutrino oscillation effects are not accounted for in these figures, so in reality, a few tau-neutrinos do also get observed. Both of these concepts will be further discussed in Chapter 4.

The $\cos(\theta_{zenith})$ quantity observed in Figure 1.10 is typically used by atmospheric neutrino experiments to describe the directional dependence of neutrinos and is directly proportional to the propagation length of the neutrino such that

$$L \approx -D_{Earth} \cos(\theta_{zenith}) \quad (1.28)$$

for $\cos(\theta_{zenith}) < 0$. Figure 1.11 shows a visual representation of this quantity with respect to the SPL and how it changes depending on where the neutrino is produced.

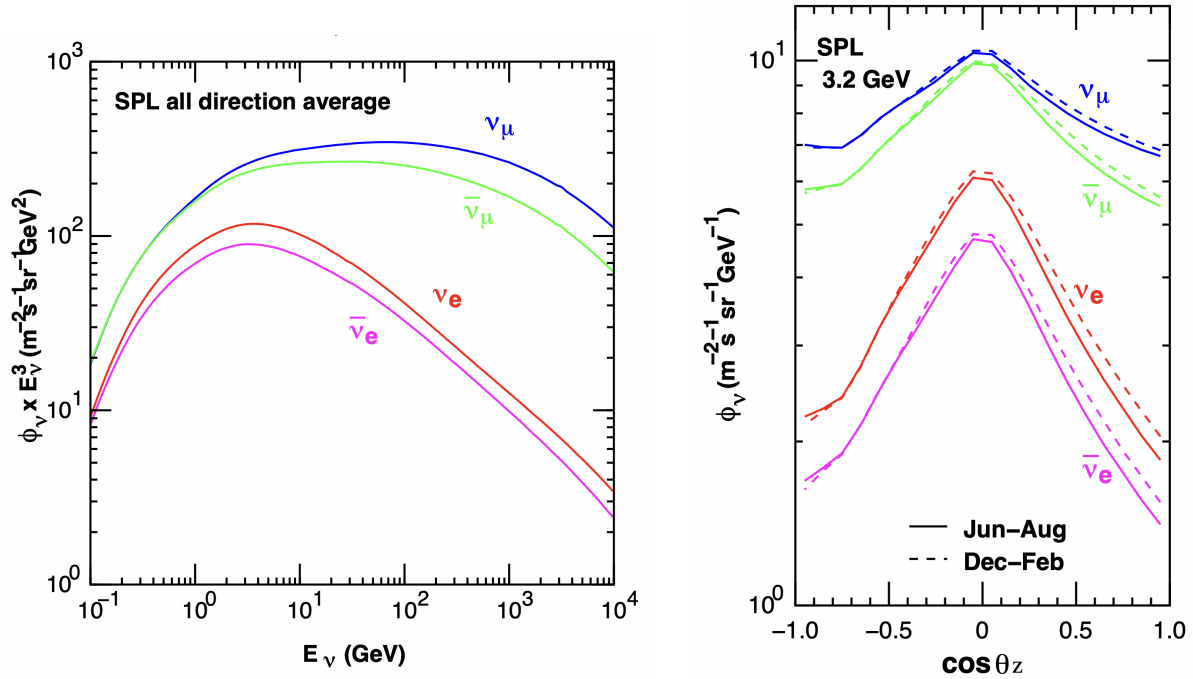


Figure 1.10: Atmospheric neutrino flux expected at the South Pole Lab (SPL) for neutrinos and anti-neutrinos [31]. Note that tau-flavored neutrinos are not shown since these are not produced as part of secondary cosmic ray decays. However, a few tau-flavored neutrinos are generated as a result of neutrino oscillations.

As can be seen in Figure 1.10, the atmospheric neutrino flux has a dependence on both energy and $\cos(\theta_{zenith})$. Although the spectra of both primary and secondary cosmic rays are the main contributing factors of this, other effects such as the density and temperature of the atmosphere as well as the Earth's magnetic field are also important. The Earth's magnetic field diverts primary cosmic rays in a preferential direction before they reach the atmosphere. This is due to the positive charge of the primaries.

Figure 1.12 shows the seasonal variation of the flux as compared to the one-year average as a function of neutrino energy for an all-direction average. This seasonal variation occurs mainly from changes in the density and the temperature of the atmosphere. As a result of using multiple years of data for this work, the effects of seasonal variation get averaged out and are, therefore, negligible.

It is important to mention that "down-going" muons (as defined in Figure 1.11) produced from primary and secondary cosmic rays tend to constitute as background for

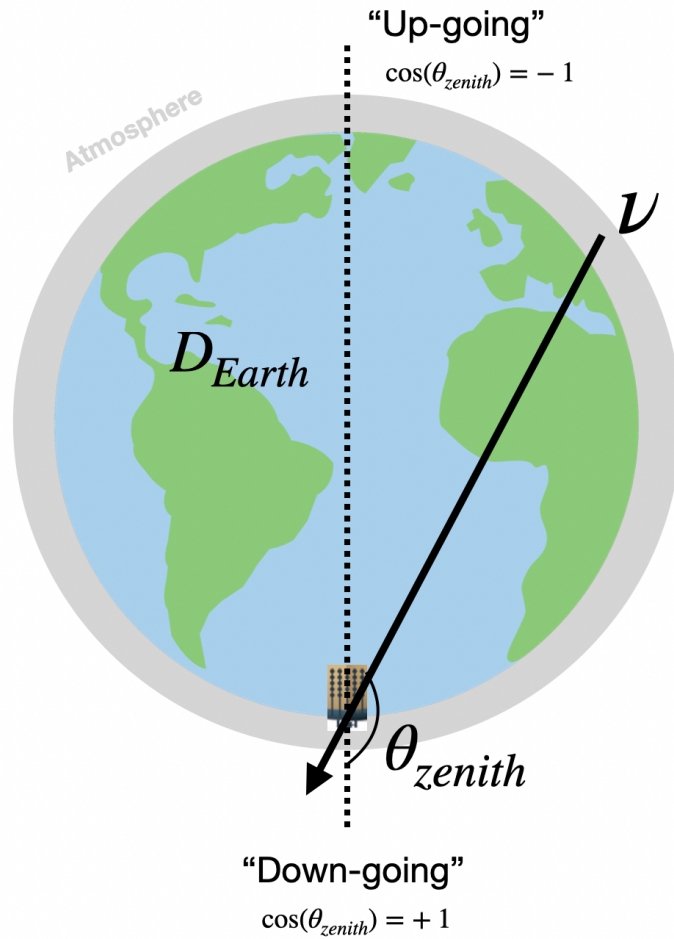


Figure 1.11: Angular dependence of neutrinos according to where these were initially produced. The $\cos(\theta_{zenith})$ quantity is directly proportional to the propagation length of the neutrino, L .

atmospheric neutrino experiments as these can be confused with the outgoing muons from CC interactions of muon-flavored neutrinos. Filtering methods are then used to reduce this background significantly. More details about this filtering process are given in Chapter 3.

1.7 Neutrino Mass Ordering

As a result of neutrino oscillations, at least two of the three neutrino mass states must have non-zero mass. Since neutrinos are so light and only interact through the weak interaction, it has become very difficult for experiments throughout the years to measure their masses.

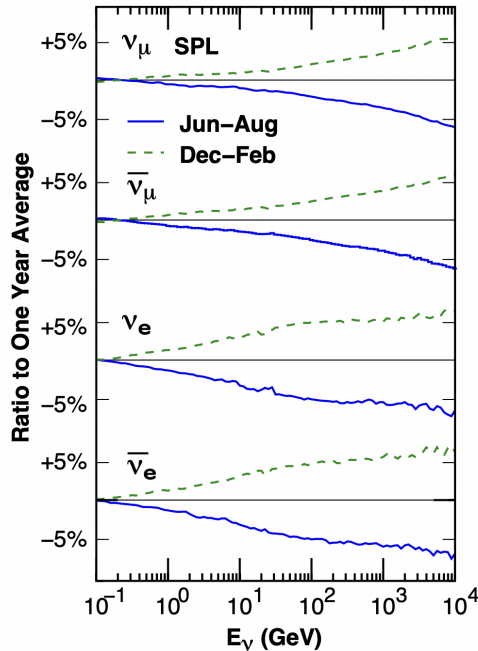


Figure 1.12: Seasonal variation of the flux as compared to the one-year average as a function of neutrino energy for an all-direction average [31].

One way to achieve this is by indirectly measuring the neutrino mass through beta decay.

As mentioned in Section 1.1, beta decay occurs when a neutron transforms into a proton and emits an electron and an electron anti-neutrino. There is an energy spectrum observed for the emitted electron due to the anti-neutrino carrying the rest of the energy difference. Thus, the higher the mass of the anti-neutrino, the lower the maximum possible electron energy. In this way, the mass of the neutrino can be measured by looking at the energy difference between the expected spectrum maximum if the neutrino were to have zero mass and the observed spectrum maximum. Figure 1.13 shows this concept for the KATRIN experiment [13], which uses Tritium beta decays. The latest results from KATRIN set an upper boundary of the electron anti-neutrino mass at 0.8 eV with a confidence level of 90% [10].

Another way to measure the neutrino masses is by measuring the mass splittings in the neutrino oscillation probability. The mass splittings, however, represent differences of mass squared and are, therefore, not able to make a statement on the absolute neutrino

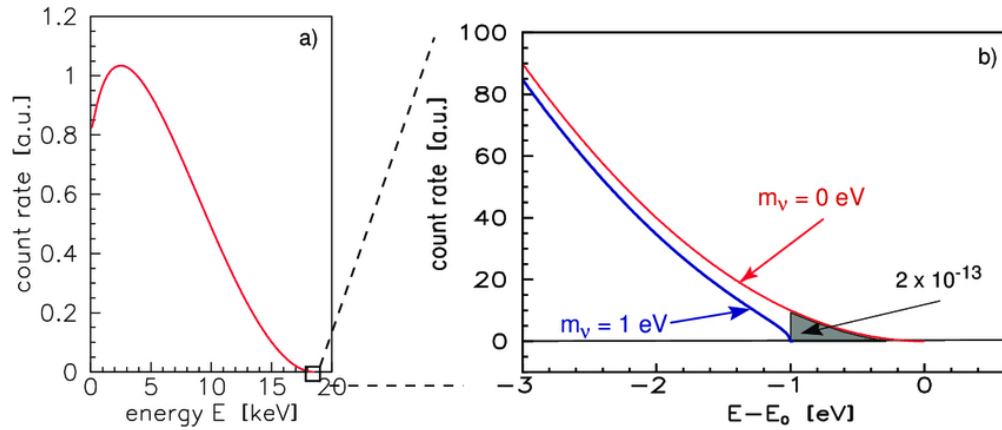


Figure 1.13: Concept of the KATRIN experiment for indirectly measuring the mass of the electron anti-neutrino through the beta decay of Tritium atoms [13]. The mass can be measured by looking at the energy difference between the expected spectrum maximum if the neutrino were to have zero mass and the observed spectrum maximum.

masses. Nevertheless, the ordering of these plays a crucial role in determining the answer to many of the open questions discussed in Subsection 1.2.1 such as neutrinoless double beta decay as well as why the universe is made up of more matter than anti-matter (a question tied to the value of the δ_{CP} phase). These questions rely greatly on the *neutrino mass ordering*, and as such, experiment sensitivities do so as well.

The neutrino mass ordering (NMO) organizes the mass states by the square of their masses. Figure 1.14 shows the only two possibilities still allowed of the mass ordering for the three-neutrino paradigm where the normal ordering (NO) places the ν_3 mass state as the heaviest mass state while the inverted ordering (IO) places this one as the lightest mass state. Moreover, this is also expressed by the sign of the Δm_{31}^2 mass splitting as this is positive for NO and negative for IO as seen in the figure. The sign of Δm_{21}^2 , however, was confirmed to be positive through measurements of matter-enhanced neutrino oscillations in the Sun [56].

The main source of neutrino production in the Sun is the proton-proton fusion chain, or pp-chain [9], which produces electron neutrinos. Through Equation 1.22, we can see that matter effects in the Sun would only be resonant for electron neutrinos if Δm_{21}^2 is positive. As such, by measuring matter-enhanced neutrino oscillations from solar neutrinos, the

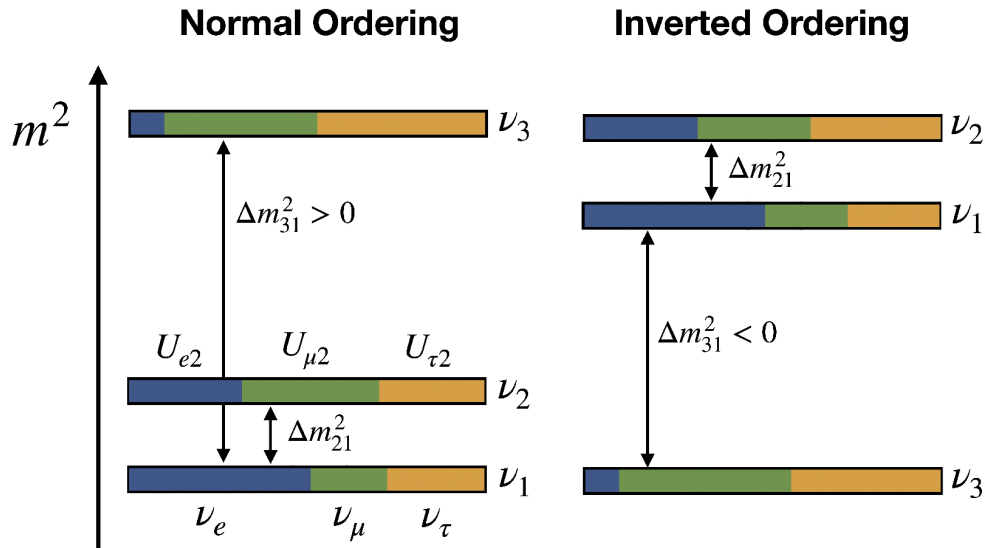


Figure 1.14: Diagram showing the normal ordering (NO), where ν_3 is the heaviest mass state and Δm_{31}^2 is positive, and the inverted ordering (IO), where ν_3 is the lightest mass state and Δm_{31}^2 is negative [59]. Flavor mixing ratios are also shown for all three mass states computed using the corresponding PMNS matrix elements.

sign of Δm_{21}^2 must be positive [56].

1.8 Status of Neutrino Oscillation Measurements

Global fits of the oscillation parameters consist in combining all of the measurements made by the various neutrino oscillation experiments (shown in Figure 1.8). The latest global fits are shown in Table 1.1 where it can be seen that $|\Delta m_{21}^2|$ is approximately two orders of magnitude smaller than $|\Delta m_{3\ell}^2|$, and $|\Delta m_{31}^2| \approx |\Delta m_{32}^2|$.

Measurements of the NMO have also been conducted by several experiments—mainly the NuMI Off-axis ν_e Appearance (NOvA) experiment, the Tokai to Kamioka (T2K) experiment, and the Super-Kamiokande experiment [25]. Individually, each of these observe a mild preference for NO over IO. The latest results by Super-Kamiokande show a disfavoring of the IO hypothesis at a 92.3% confidence level (CL) [44]. At the same time, while NOvA and T2K do also observe a preference for NO, there is an ongoing tension with respect to the δ_{CP} phase [43] as can be seen in Figure 1.15. The preference for NO can be

| Osc. Parameter | Best Fit Point $\pm 1\sigma$ | |
|--|---------------------------------|---------------------------------|
| | NO | IO |
| $\sin^2(\theta_{12})$ | $0.303^{+0.012}_{-0.012}$ | $0.303^{+0.012}_{-0.011}$ |
| $\sin^2(\theta_{23})$ | $0.451^{+0.019}_{-0.016}$ | $0.569^{+0.016}_{-0.021}$ |
| $\sin^2(\theta_{13})$ | $0.02225^{+0.00056}_{-0.00059}$ | $0.02223^{+0.00058}_{-0.00058}$ |
| $\delta_{\text{CP}} (\text{°})$ | 232^{+36}_{-26} | 276^{+22}_{-29} |
| $\Delta m_{21}^2 (\times 10^{-5} \text{ eV}^2)$ | $7.41^{+0.21}_{-0.20}$ | $7.41^{+0.21}_{-0.20}$ |
| $\Delta m_{3\ell}^2 (\times 10^{-3} \text{ eV}^2)$ | $+2.507^{+0.026}_{-0.027}$ | $-2.486^{+0.025}_{-0.028}$ |

Table 1.1: Global fits of the oscillation parameters including atmospheric data from the Super-Kamiokande experiment (NuFIT 5.2 (2022) [15]) where the mass splitting, $\Delta m_{3\ell}^2$, is given for Δm_{31}^2 for NO and Δm_{32}^2 for IO.

understood by looking at the best fit points of both experiments as well as by the larger CL contours as compared to those observed for IO (smaller contours show that more of the parameter space is ruled out). The tension in δ_{CP} shows up in the almost non-overlapping NO CL contours while, for IO, these are in agreement.

As a result of this tension, any measurement of the NMO that can be performed *without* a dependence on the δ_{CP} phase becomes increasingly important. One such experiment that has the ability to do this is the IceCube Neutrino Observatory. Further discussed in Chapter 2, IceCube uses one cubic kilometer of ice at the geographical South Pole to detect neutrinos. Due to its positioning, IceCube can record atmospheric neutrino events with energies greater than 3 GeV, opening a new window in the low-energy regime. Thus, with a δ_{CP} -independent baseline and its ability to see higher-energy neutrino events compared to those recorded by the above-mentioned experiments, IceCube can now shed light on the mystery of the neutrino mass ordering from a unique perspective. The work described in this dissertation focuses specifically on the latest 9.28-year IceCube measurement of the NMO performed with atmospheric neutrino oscillations. The goal of this work is to deliver a more robust result of the mass ordering preference in comparison to the previous 3-year IceCube measurement [40] through an increase in the detector livetime by more

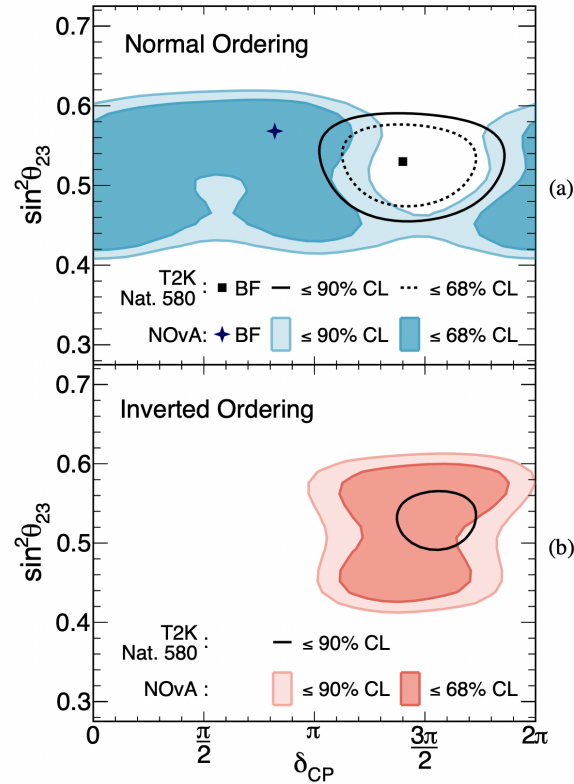


Figure 1.15: Latest results by the NOvA and T2K experiments on the NMO in the $(\sin^2(\theta_{23}), \delta_{CP})$ parameter space [43]. A preference for NO is observed by looking at the best fit points of both experiments as well as by the larger CL contours as compared to those observed for IO. A tension, however, shows up for δ_{CP} in the almost non-overlapping NO CL contours while, for IO, these are in agreement.

than 3 times, improved data analysis techniques, and improved filtering methods.

Chapter 2

The IceCube Neutrino Observatory

2.1 The IceCube Array

The IceCube experiment consists of 5160 optical sensors embedded into 1 cubic kilometer of Antarctic ice as shown in Figure 2.1. For the main IceCube array, the optical sensors, called digital optical modules (DOMs), are located 1450 m below the surface. There are 78 IceCube strings that each hold 60 DOMs with 17 m of vertical spacing between each DOM. Horizontally, the strings follow a hexagonal arrangement with 125 m spacing between them [28]. Cables attached to the strings provide a mechanism to read out the DOM signal, which reaches the surface and is processed in the IceCube Lab (ICL).

2.1.1 The DeepCore Subarray

The DeepCore subarray is comprised of 8 additional, more compact DeepCore strings as well as the 7 surrounding IceCube strings as shown in Figure 2.2. The DeepCore strings house a veto region and a main DeepCore region. The veto region is 100 m deep with 10 DOMs and is located at a depth of 1750 m. Moreover, the main DeepCore region contains 50 DOMs at a depth of 2100 m. DOMs in the main DeepCore region are placed 7 m apart vertically and 41 m to 105 m apart horizontally [28]. The purpose of the DeepCore subarray

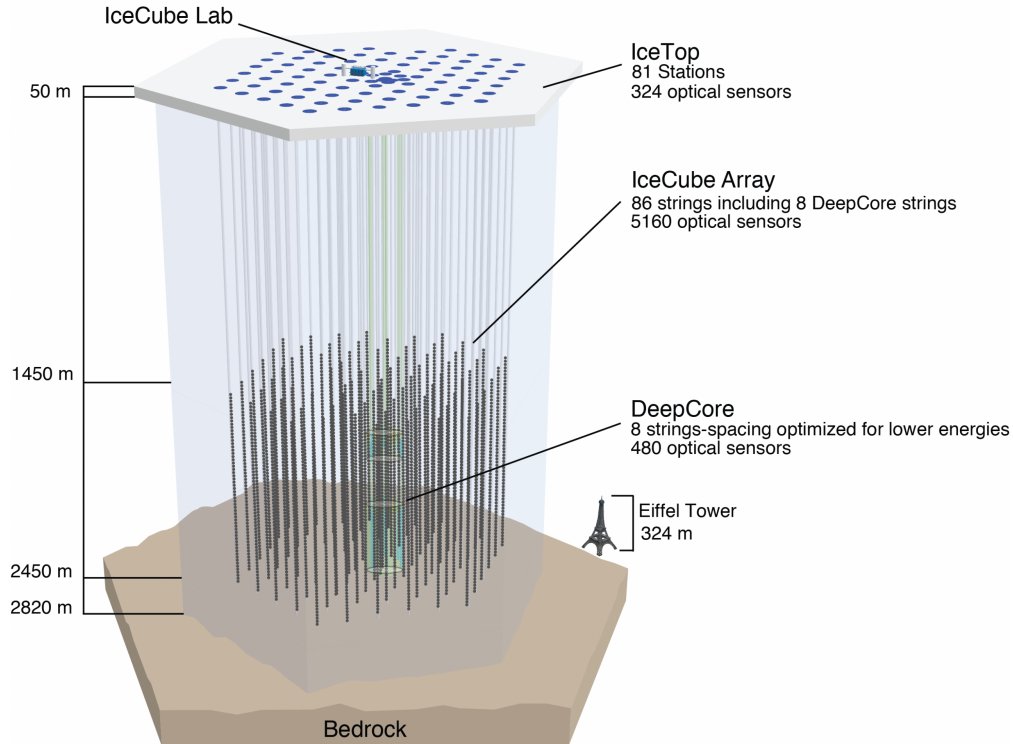


Figure 2.1: Diagram of the IceCube experiment located at the geographical South Pole 1450 m below the surface [1].

is to detect low-energy neutrino events, which output a signal of less intensity. *Low-energy* in this context denotes any event from incident neutrino energies ranging from 3 GeV to 100 GeV. These events are of particular interest for the work presented here as these fulfill the atmospheric baselines needed for neutrino oscillation measurements as shown in Figure 1.8.

2.1.2 Digital Optical Modules

Neutrino events in IceCube are detected using digital optical modules (DOMs). Each DOM is made up of one 10-inch photomultiplier tube (PMT) as well as various electronic boards that extract the signal up to the surface as shown in Figure 2.3. The entire structure is held inside of a 13-inch glass sphere strong enough to withstand the outer pressure when embedded in the ice.

PMTs detect light through the photoelectric effect by emitting a photoelectron (PE)

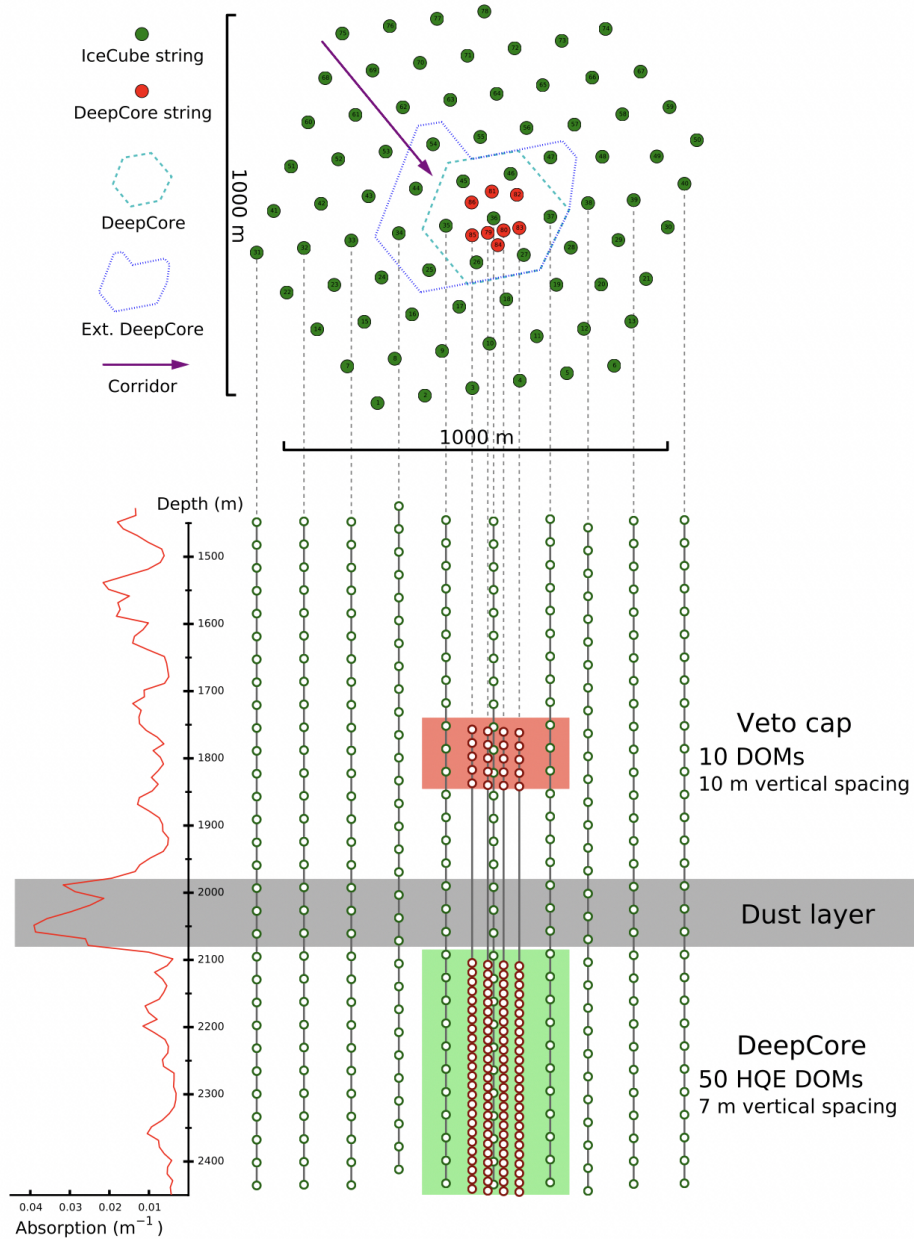


Figure 2.2: Diagram of the DeepCore subarray consisting of 8 additional, more compact DeepCore strings as well as the 7 surrounding IceCube strings [39]. The purpose of the DeepCore subarray is to detect low-energy neutrino events for atmospheric neutrino detection for oscillation measurements.

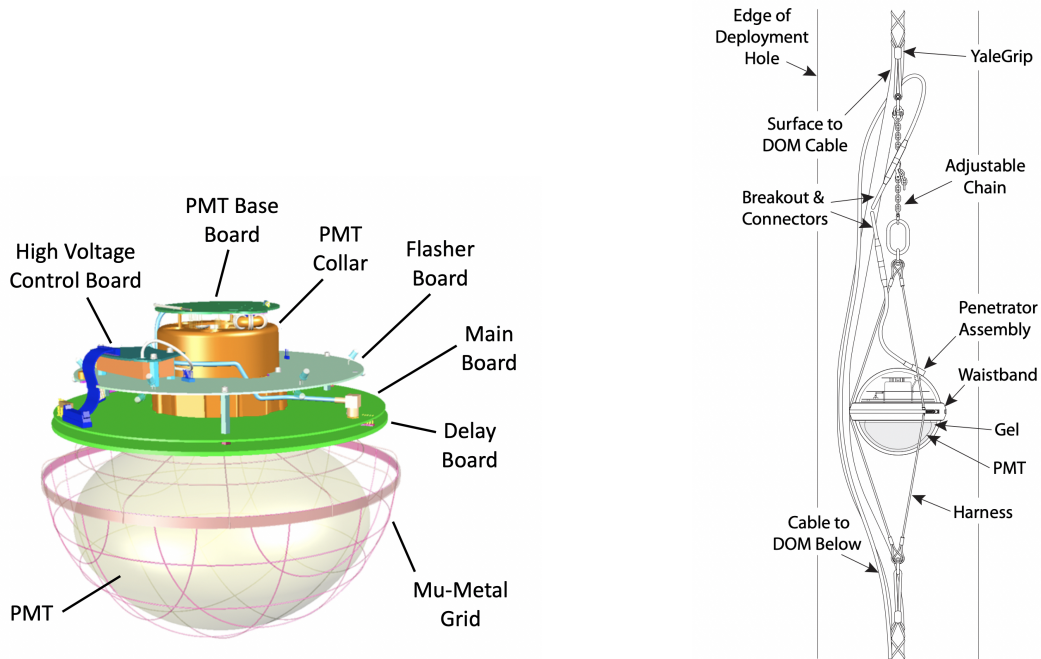


Figure 2.3: Diagram of a digital optical module (DOM) [28].

from the photocathode after a photon capture. The PE is then amplified to create a current that is read out. In IceCube, PMTs are placed facing downward toward the bedrock for the purpose of detecting more up-going neutrinos. The PMT is capable of detecting 300 nm to 600 nm photons and has a peak quantum efficiency of 25% for the IceCube DOMs. The DeepCore DOMs, however, were designed to have a higher efficiency at 33%, which helps to improve the detection of low-energy events. The readout of the electronics is then converted to digitized waveforms where approximately 0.8 mV corresponds to 1 PE. The threshold for reading and storing a waveform is 0.25 PE [28] [34].

2.2 Event Detection in the Ice

Neutrinos interact with the ice through the different interaction models and channels described in Section 1.4. When these interactions occur, charged secondary particles traveling at speeds close to the speed of light get produced leaving a trace of light that is then detectable by the DOMs. This mechanism of light emission is called the Cherenkov

effect.

2.2.1 Cherenkov Radiation

When a charged particle moves through a dielectric medium, the particle's electromagnetic field polarizes the atoms in its path, leading to photon emissions as the atoms return to their ground state. If the charged particle's speed is faster than the speed of light *in the medium*, the emitted photons will interfere constructively to form a cone of light called Cherenkov radiation [52]. Precisely, Cherenkov radiation occurs when the condition

$$v > c_n \quad (2.1)$$

is met where c_n is the speed of light in the medium, v is the velocity of the charged particle, and $c_n = \frac{c}{n}$ where c is the speed of light in vacuum and n is the index of refraction of the medium. This phenomenon can be observed in Figure 2.4 where the Cherenkov angle becomes

$$\cos(\theta_C) = \frac{c}{nv}. \quad (2.2)$$

Generally, Cherenkov radiation comes as either ultraviolet or visible light although the peak of the spectrum lies at wavelengths of about 420 nm [53], or purple and blue light.

In IceCube, the medium is the Antarctic ice with an index of refraction of $n = 1.31$ [63]. We can now calculate the energy threshold for a charged particle to emit Cherenkov radiation using the equation for relativistic total energy such that

$$E_{\text{threshold}} = mc^2\gamma = \frac{mc^2}{\sqrt{1 - (\frac{v}{c})^2}} = \frac{mc^2}{\sqrt{1 - (\frac{1}{n})^2}} = \frac{mc^2n}{\sqrt{n^2 - 1}}. \quad (2.3)$$

From Equation 2.3, we can see that an electron propagating through ice would need to have more than ~ 791 keV of energy to generate Cherenkov radiation. Due to its greater

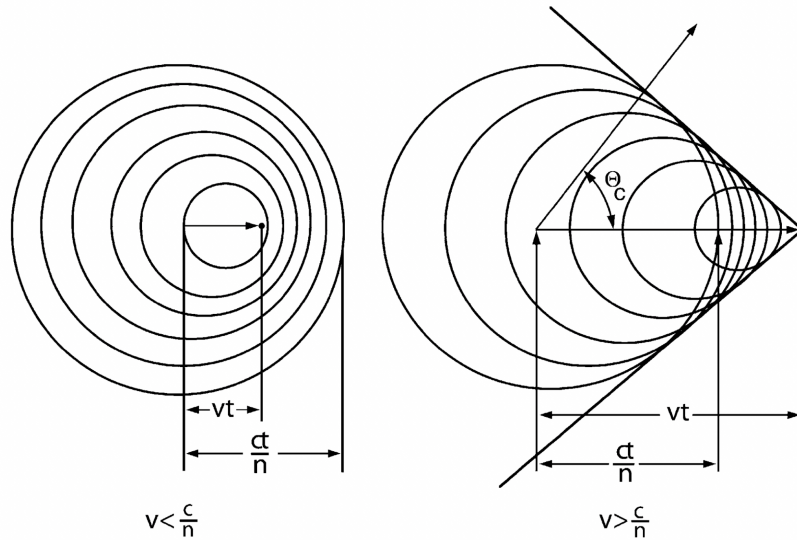


Figure 2.4: The Cherenkov effect is shown on the right-hand plot for a charged particle that moves at a speed greater than the speed of light in a dielectric medium. In this case, a cone of emitted light is formed at an angle θ_C [65]. The left-hand plot shows the case where the particle does not travel faster than the speed of light in the medium, and hence, no constructive cone is formed.

mass, a muon would need to have more than ~ 164 MeV of energy to produce the same effect.

2.2.2 Event Signatures

At DeepCore neutrino energies, there are two types of event signatures observed in the detector— *track-like* and *cascade-like* signatures. Figure 2.5 shows an example of each where a track-like event leaves a long trace of Cherenkov radiation while a cascade-like event shows a near-isotropic morphology.

2.2.2.1 Track-like Events

Track-like events arise from muon neutrino and anti-neutrino CC interactions with the ice. In these, a final state muon particle is produced which loses energy slowly as it moves across the detector creating a long "track" of Cherenkov radiation. This occurs because the muon is a *minimum ionizing particle* (MIP) at DeepCore energies, meaning that it loses most

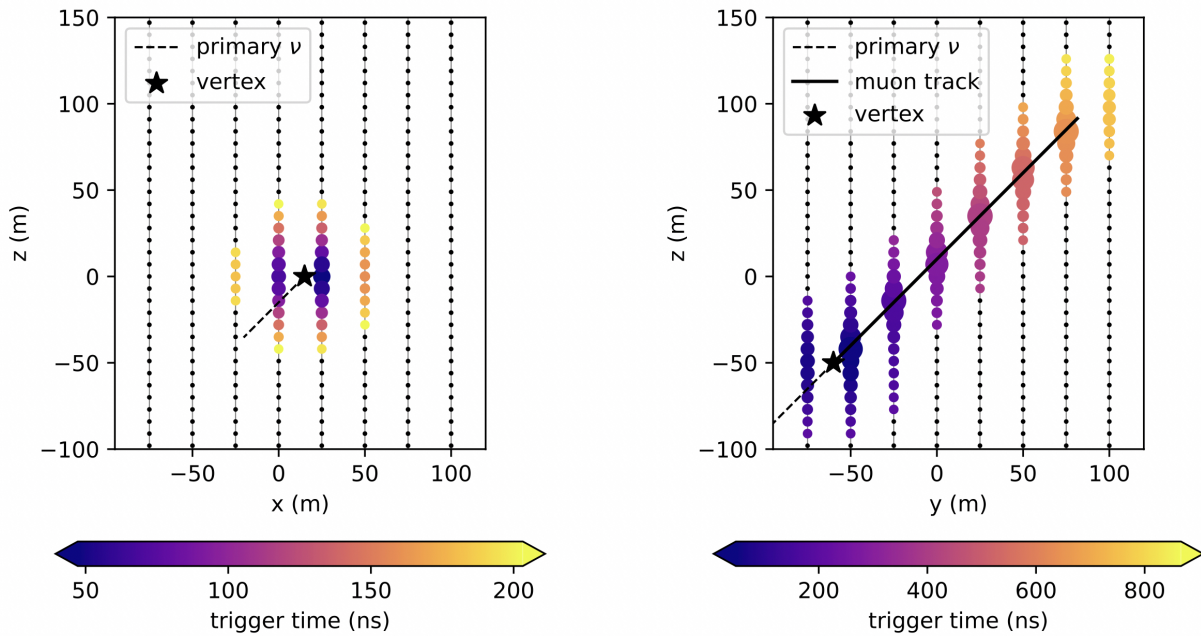


Figure 2.5: Illustration of DeepCore event topologies consisting of cascade-like (left) and track-like (right) event signatures. The diagrams show a cross-sectional view of the detector's z and x (or y) axes as well as the evolution of the events as a function of the trigger time [66].

of its energy through minimum ionization with the atoms in its path. Figure 2.6 shows the muon energy loss in ice as a function of the muon energy where it is seen that, at energies less than 100 GeV, the muon loss is almost constant and dominated by ionization. The muon energy is of the same order of magnitude as the incident neutrino energy; as a result, this process occurs for incident muon neutrinos with energies between 3 and 100 GeV (DeepCore energies).

Along with the final state muon, muon neutrino and anti-neutrino CC interactions also produce charged and neutral hadrons. For neutrino energies from 1 to 10 GeV, a proton and a pion will be produced from resonant scattering (Subsection 1.4.1.2). Otherwise, at neutrino energies above 10 GeV, a full hadronic shower, or cascade, of charged and neutral particles such as protons, neutrons, pions, and kaons will be produced from deep-inelastic scattering (Subsection 1.4.1.3). In both cases, the charged hadrons do not travel far distances like the muon, and thus, together form a near-spherical cluster of Cherenkov

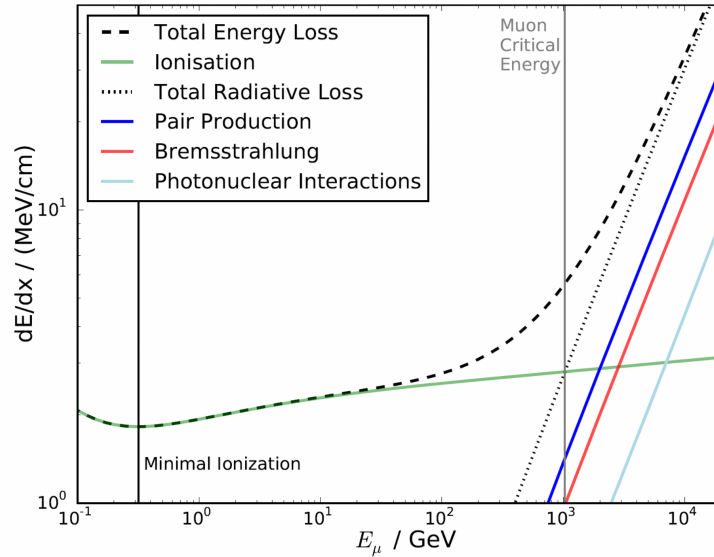


Figure 2.6: Muon energy loss in ice as a function of the muon energy [55]. At energies less than 100 GeV, the muon loss is almost constant and dominated by ionization. This leads to a slow loss of energy in ice and long Cherenkov tracks.

light.

Track-like signatures can also be produced by atmospheric muon background from above the horizon that reaches the detector. A veto region is assigned as a way to filter out some of this background. Figure 2.7 shows how the veto region is used for this purpose. Down-going atmospheric muons will enter the detector and leave a trace of Cherenkov light in the veto region before they reach DeepCore. In the case of a muon neutrino, the CC interaction will originate inside DeepCore.

2.2.2.2 Cascade-like Events

Cascade-like events arise from electron and tau neutrino and anti-neutrino CC interactions as well as all neutrino and anti-neutrino NC interactions (e, μ, τ). For each of these interactions, a hadronic cascade is produced as part of the final state. These hadrons together appear as a near-spherical cluster of Cherenkov light. For NC interactions, this is the only part of the cascade signature since the only other outgoing particle is a neutrino, which does not produce any Cherenkov light.

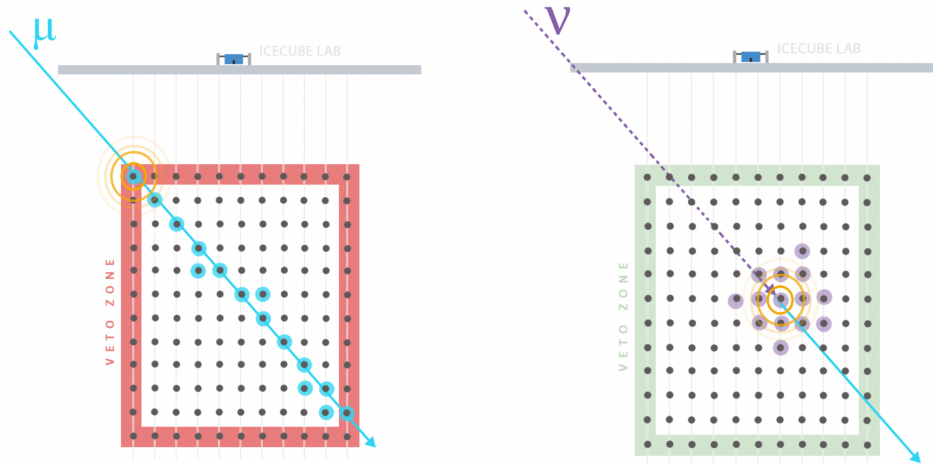


Figure 2.7: Illustration of the concept of the veto region, which helps to filter out the atmospheric muon background entering the detector [1]. Atmospheric muons from above the horizon will enter the detector and leave a trace of Cherenkov light in the veto region. For DeepCore, the veto region consists of the IceCube strings surrounding the DeepCore fiducial volume.

In the case of electron neutrino CC interactions, an electron is produced in the final state which generates an electromagnetic cascade in the detector. This occurs due to the process of *bremsstrahlung* where electrons decelerate rapidly from collisions with nuclei in the ice [65]. This deceleration causes the electrons to emit radiation so high in energy that the photons pair-produce into an electron and a positron and the cycle begins again. This process ends when the electrons and positrons reach a critical energy and start to ionize, losing the remaining energy.

For tau neutrino CC interactions, a tau particle is produced in the final state which decays quickly due to its heavy mass. This tau decay can occur in one of three ways [32]:

- $\tau \rightarrow \nu_\tau + X$ (occurs about 65% of the time)
- $\tau \rightarrow \nu_\tau + \nu_e + e$ (occurs about 18% of the time)
- $\tau \rightarrow \nu_\tau + \nu_\mu + \mu$ (occurs about 17% of the time)

where X is a hadronic cascade. The first type of tau decay listed will produce a hadronic cascade while the second will produce an electromagnetic cascade from the outgoing electron. For DeepCore energies, these will occur very rapidly after the original hadronic cascade is produced, and as a result, only one cascade-like signature will be observed. For the third type of tau decay, an outgoing muon will produce a track-like signature.

2.3 Optical Ice Properties

Using Antarctic glacial ice as a medium for detecting neutrino interactions brings about additional challenges related to accurately modeling the detailed structure of the ice. Due to this detailed structure, photons can get scattered or absorbed, leading to uncertainties in the number of photons that get detected by the DOMs if not properly modeled. This, in turn, greatly affects the reconstruction of events in IceCube.

2.3.1 Bulk Ice Properties

The *bulk ice* is considered to be Antarctic ice that has piled up throughout the years. As a result of this pile-up, the structure consists of compressed layers of ice with embedded impurities, called *dust*, coming from atmospheric conditions at the time of the layer formation. Figure 2.8 shows the ice model used for this work where the various ice layers can be observed through the fluctuating photon absorption and scattering coefficients. The absorption and scattering coefficients are scaling factors that increase or decrease each quantity. An increase or decrease in scattering and/or absorption affects the number of photons detected by the DOMs.

As can be seen in Figure 2.8, scattering and absorption are higher for the region of ice located above IceCube. This occurs due to air bubbles having formed in the ice. At lower depths, however, air bubbles have been compressed due to the pressure exerted from the structure above; thus, the absorption and scattering in this region is purely due to

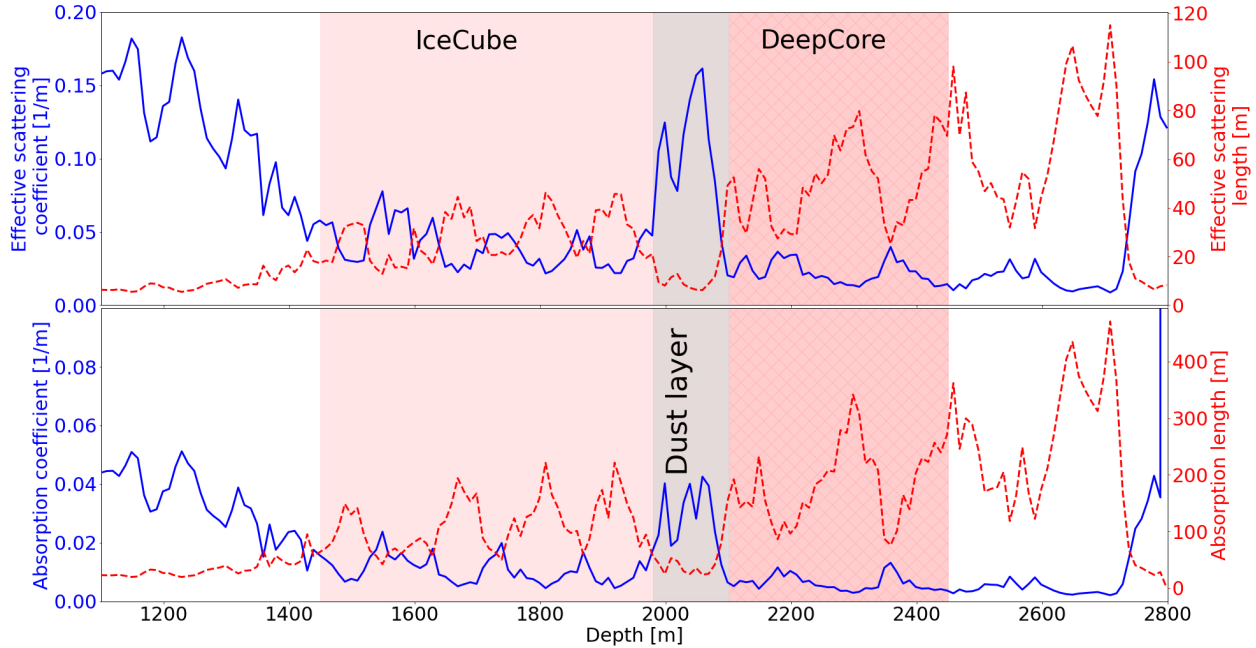


Figure 2.8: The birefringence ice model [35]. Various ice layers can be observed through the fluctuating photon absorption and scattering coefficients. The DeepCore subarray sits at a depth of extremely high ice purity found below the Dust Layer.

impurities found in the ice. Specifically, the DeepCore subarray sits at a depth of extremely high ice purity found below the *Dust Layer*, a region of increased scattering and absorption. The ice model is also affected by the structure of the bedrock below the ice as well as by glacial drifts.

Furthermore, an optical property called *birefringence* is also accounted for in Figure 2.8. Birefringence occurs when an incident photon refracts in two different directions due to the various polarizations of the material.

2.3.2 Hole Ice Properties

To insert the DOMs into the ice during the deployment period, cylindrical columns had to be drilled and melted. The refreezing process of the ice once the DOMs had been lowered caused a change in the optical structure—mainly, this *hole ice* now had a bubble column in the middle. Within the bubble column, the scattering length is smaller, reducing the probability that a photon will hit a DOM as compared to the case of no bubble column.

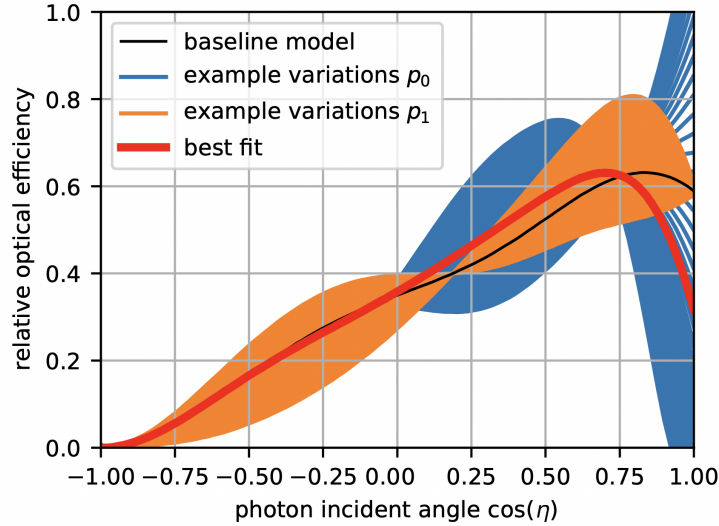


Figure 2.9: The optical efficiency of the DOM as a function of the photon incident angle, $\cos(\eta)$ [41]. Towards $\cos(\eta) = 1$, the optical efficiency decreases due to the presence of the bubble column whereas, for no bubble column, the curve would continue to increase.

This is accounted for in the ice simulation by adjusting the optical efficiency of the DOM as a function of the photon incident angle, $\cos(\eta)$, as shown in Figure 2.9. The *DOM efficiency* is the probability of detection of an incoming photon by the PMT in the DOM. Moreover, $\cos(\eta) = 1$ for a photon hitting the PMT head-on directly from below while $\cos(\eta) = -1$ for a photon coming directly from above the PMT. The figure shows variations in two parameters, p_0 and p_1 , which together account for variations in all of the different hole ice models that have been produced through either calibration measurements, oscillation measurements, or water tank measurements [45]. As can be observed, towards $\cos(\eta) = 1$, the optical efficiency decreases due to the presence of the bubble column whereas, for no bubble column, the curve would continue to increase.

Chapter 3

The Data Sample

3.1 Monte Carlo (MC) Simulation

In order to perform any atmospheric neutrino oscillation analysis with DeepCore, a Monte Carlo (MC) simulation of the expected data is generated for the purpose of measuring a particular effect in the observed data. Both the MC simulation and the observed data undergo eight processing levels as a way to decrease the atmospheric muon and noise background from the sample while maintaining as much of the neutrino signal as possible. A neural network is trained using a separate MC sample generated solely for the purpose of event reconstruction and classification training. The optimized network model is then applied to the cleaned MC and data samples to reconstruct the energy and zenith angle of the events as well as classify the different event signatures in the sample. Figure 3.1 shows a diagram depicting this procedure.

There are two main types of events that are simulated in the MC— neutrino and atmospheric muon events. These events are modeled using the nominal expectation for different systematic uncertainties. Separate MC sets, ones for which off-nominal detector uncertainties are used, are also generated. The purpose for these extra MC sets will be further discussed in Section 4.3.

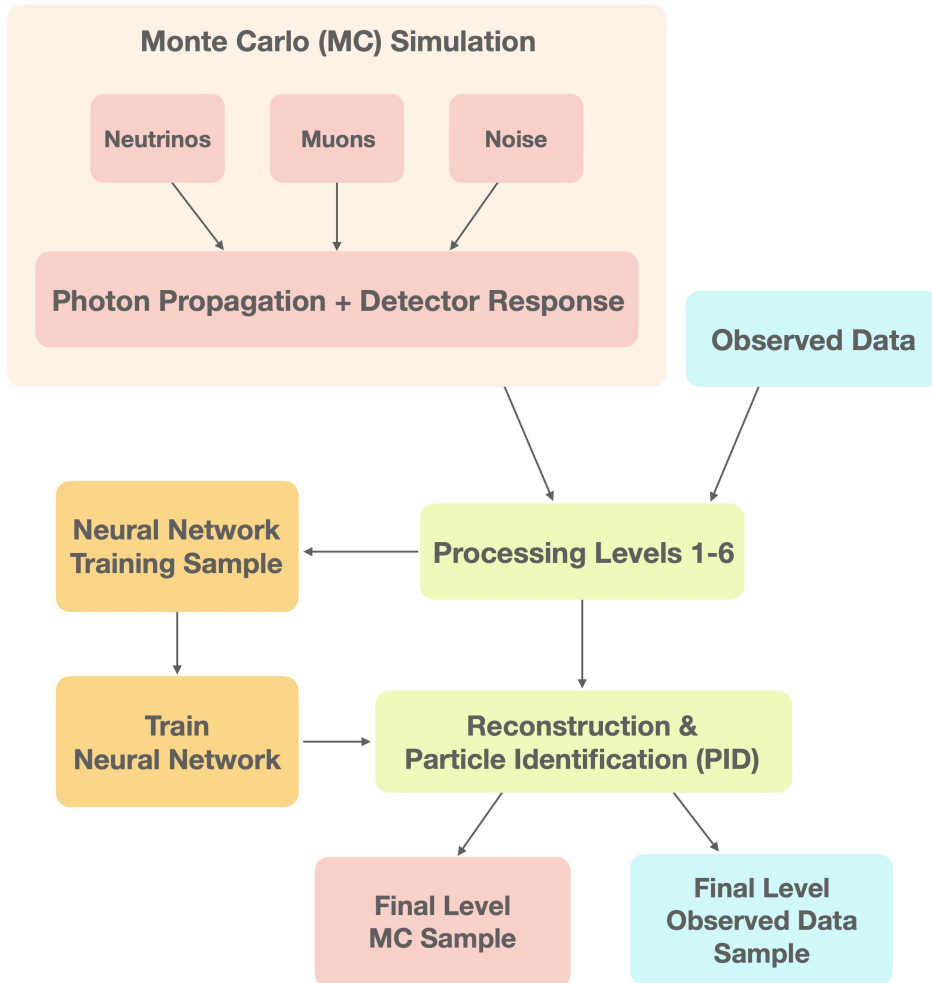


Figure 3.1: The FLERCNN Sample Processing Chain. A Monte Carlo (MC) simulation as well as the observed data are both processed by 6 different filtering levels followed by reconstruction of the event energy and zenith angle and particle identification (PID) of event signatures.

3.1.1 Neutrino Events

Since neutrinos rarely interact with the ice due to their extremely light mass, it becomes too inefficient and computationally expensive to simulate the total number of neutrinos expected to traverse DeepCore for a given livetime. Instead, all of the neutrino events modeled are required to interact inside the DeepCore cylinder volume. In turn, this produces a larger number of raw events compared to what is otherwise expected from atmospheric neutrino flux predictions. To account for this, a weight is calculated for each

event. Multiplying the weight of an event by the flux and the total livetime yields the fraction of events *expected* from the contribution of this one particular event.

Neutrino interactions in the ice are simulated with the GENIE framework [18]. For each event, GENIE computes the cross-section of the neutrino-nucleon interaction and simulates the propagation of the final state particles. More than 70 years of combined event livetime are simulated for neutrino energies from 1 GeV to 10 TeV for each neutrino flavor. Of the GENIE events, 70% are neutrino events and 30% are anti-neutrino events.

3.1.2 Atmospheric Muon Background

For the atmospheric muons, a slightly different approach is taken. Due to the large number of atmospheric muons that deliberately get discarded as the sample undergoes the filtering levels, two separate simulations are generated for the purpose of fine-tuning the filters. In the first simulation, muons are allowed to interact anywhere within the entire IceCube array in an effort to fine-tune up to Level 4 of the processing chain. In the second simulation, muons are restricted to interact in the DeepCore subarray only. This allows more muons to survive up to higher filtering levels, and as a result, Levels 5 and above are able to be tuned.

Similarly to the neutrino event simulation, muons are assigned a weight that is multiplied by the atmospheric muon flux and the total livetime to obtain the number of expected muon events. Muons are propagated using the MuonGun internal software [67]. More than 6 years of combined event livetime are simulated for muon energies from 150 GeV to 5 TeV.

3.1.3 Photon Propagation and Detector Response

Neutrino interaction primaries and secondaries both produce Cherenkov photons in the ice. To accurately simulate the trajectory of these photons, a few different simulation frameworks are used. For photons originating from muon propagation, the PROPOSAL

software [26] is used. Furthermore, for photons produced from all other kinds of charged particle propagation, the GEANT4 software [37] is used. To simulate the absorption and scattering effects in the ice discussed in Section 2.3, the CLSIM package [19] is used.

For photons that hit a DOM, the detector response is simulated. The efficiency and angular acceptance of the DOM are used to determine the probability that the photon will produce a PE. The amount of current generated by the PMT as a result of the PE is also simulated. Finally, the signal is converted into digitized waveforms and passed through the processing filters in the same manner as for the real data.

3.1.3.1 Noise Hits

PEs from radioactive decays in the DOM and PMT glass as well as thermally-induced PMT dark noise produce noise hits in the detector, where dark noise is defined as randomly emitted PEs from the photocathode in the PMT. Noise hits can occur at any given moment, and, therefore, need to be accounted for in the neutrino and muon simulations to further improve the accuracy of an event. Moreover, pure noise events can also occur, faking a signal in the detector. These are simulated using the Vuvuzela software [54] for 2 months of combined event livetime.

3.2 Data Processing

To reduce the atmospheric muon and noise background and retain as much of the neutrino signal as possible, both the MC simulation and the observed data are processed through various filtering levels. The different techniques applied at each level depend on the complexity of the remaining background events in the sample as, the higher the level, the more difficult it is to tell apart signal from background. Figure 3.2 shows the event rates from Level 2 to the final level cuts.

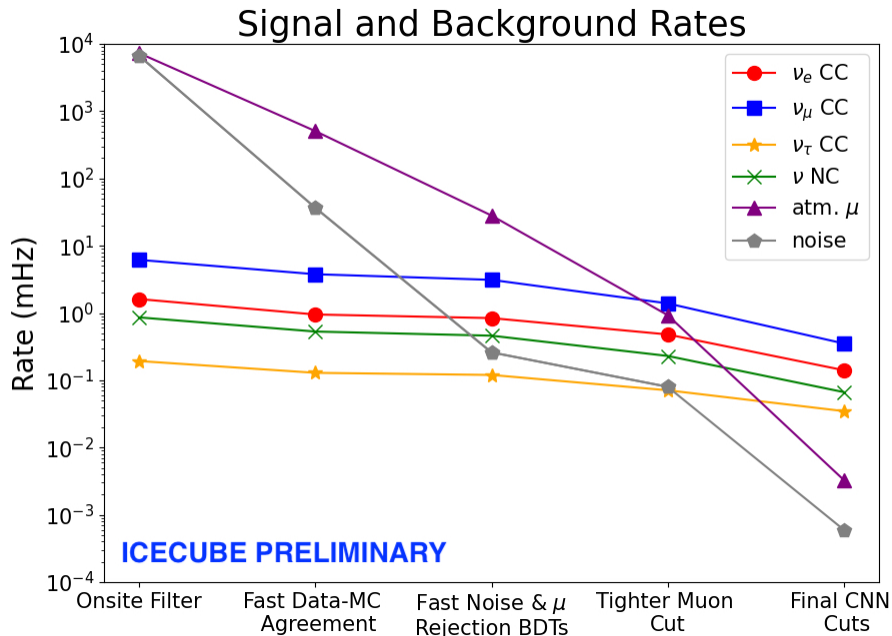


Figure 3.2: Event rates for the FLERCNN sample from Level 2 to the final level cuts.

3.2.1 Event Trigger (Level 1)

It was briefly discussed in Subsection 2.1.2 that the readout threshold for a given DOM hit was 0.25 PE. More precisely for DeepCore, an event is recorded when at least three nearby DOMs each detect a waveform greater than or equal to 0.25 PE within a time-window of 1 μ s, also known as a Hard Local Coincidence (HLC). The three DOM hits must occur in a 2.5 μ s time-window, a condition enforced by the SMT3 trigger. Single hits are recorded as Soft Local Coincidences (SLC) since many of these qualify as random noise.

3.2.2 Onsite Filter (Level 2)

After an event is recorded, an initial filter is applied onsite at the South Pole, where the type of filter varies depending on the physics being studied. For DeepCore studies, the filter used, referred to as the *DeepCore Filter*, is designed for rejecting atmospheric muons that hit the veto region described in Subsection 2.2.2. The filter works by calculating the center of gravity (COG) for the hits located inside the DeepCore fiducial volume. Based

on the reconstructed velocity that it would take for the hits in the veto region to reach the COG, the filter determines whether this velocity matches that which is expected of atmospheric muons, and if so, rejects the event.

3.2.3 Data-MC Agreement Cuts (Level 3)

At Level 3, several fast algorithms are applied to the sample, aimed at reducing atmospheric muon and noise background through data-MC agreement cuts for different event variables. The goal at this stage is to place a cut at the point of disagreement between the data and MC to remove any unsimulated background events that reach the detector. These include coincident events involving both a neutrino and a muon as well as muon bundles.

Coincidences occur when a neutrino interaction in DeepCore is directly followed by an atmospheric muon event. These are able to pass both the trigger level and DeepCore filter; however, hits for these types of events are generated for a longer period of time than would otherwise be expected from one single event. Therefore, a cut is placed on the total time length as shown in Figure 3.3, where the cut is located at $5\mu\text{s}$ and any events with a greater time length are discarded.

Cuts targeting the removal of atmospheric muons and muon bundles focus mainly on keeping those events that are contained within the DeepCore fiducial volume. The cuts include removing events with 10 or more hits in the veto region as well as those whose first HLC trigger lies above a depth of 2068 m below the surface.

Noise events, although simulated, are greatly reduced through data-MC cuts by 99%. First, a cleaning approach is performed to get rid of any obvious noise hits in a given event. If the *cleaned* event contains fewer than 6 hits, it is discarded. Other cuts assessing the direction that the event traveled as well as the time difference between hits also contribute to decreasing the noise background. After Level 3, the neutrino to noise to muon ratio of the sample is 1:7:100, respectively [41].

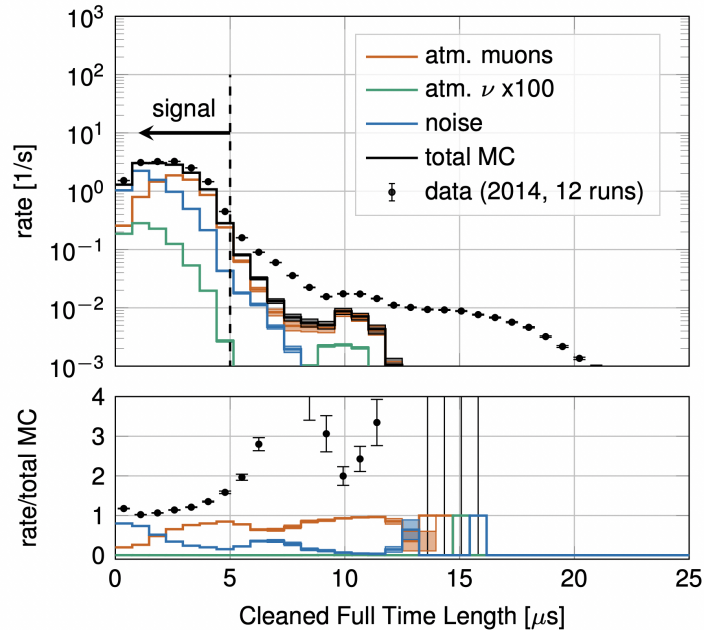


Figure 3.3: Data - MC full time length cut at Level 3 [41]. The cut is placed at $5\mu\text{s}$ and any event with a greater time length is discarded.

3.2.4 Background Rejection BDTs (Level 4)

At Level 4, machine learning algorithms are used to further identify background events. The sample is fed to two separate Boosted Decision Trees (BDTs)— one for rejecting atmospheric muons and one for rejecting noise —which help to spot the most difficult background events. The package used for these is the LightGBM package [21].

For noise rejection, the BDT is trained on MC noise and neutrino events using Level 3 and 4 noise-related variables. Some of these include the number of cleaned DOM hits as well as the amount of spread of the hits about the first HLC trigger. For atmospheric muon rejection, the BDT is trained on real data muon events and MC neutrino events. Real data is used at this stage due to its high content of atmospheric muon events comprising 99% of the sample. Using real muon events increases the robustness of the training sample. Level 3 and 4 muon-related variables are then used to train the BDT.

The output for each event consists in a value between 0 and 1, where, the closer the value is to 0, the more an event is classified as background-like, while a value closer to

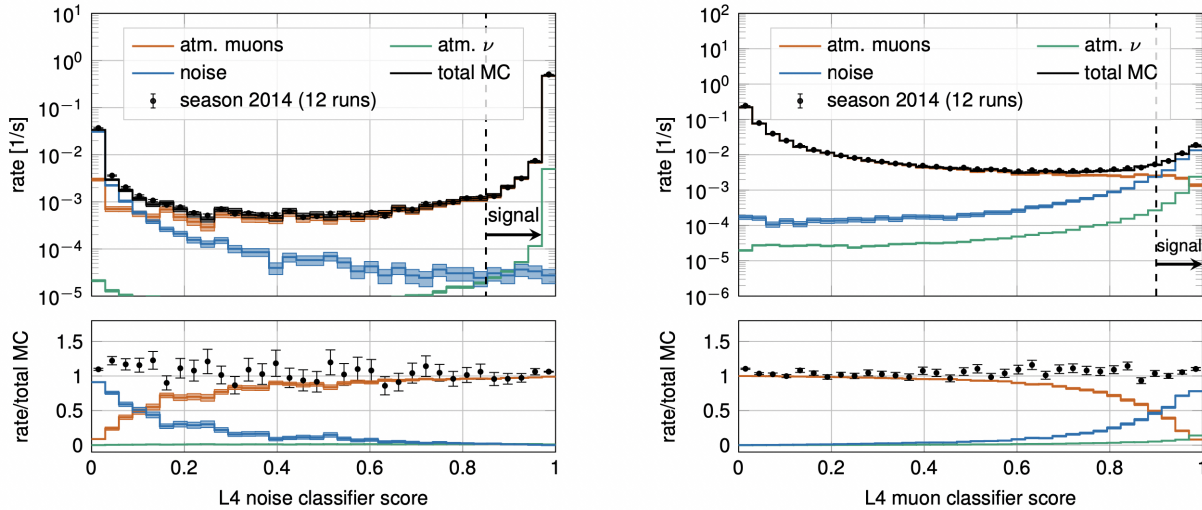


Figure 3.4: Level 4 background-signal BDT classification [41]. The left plot shows the event distribution as a function of the noise BDT score while the right plot shows the same events as a function of the atmospheric muon BDT score. The score ranges from 0 to 1, where a value closer to 0 is considered more background-like and closer to 1 is considered more signal-like.

1 corresponds to being more signal-like. Figure 3.4 shows the classification of events by both the noise and muon BDTs. A cut is placed at 0.85 for the noise classifier and at 0.9 for the muon classifier, keeping all events above this score. After Level 4 processing, there are very few noise events left in the sample; it is mostly comprised of a 2:1 ratio of muons to neutrinos, respectively [41].

3.2.5 Corridor and Containment Muon Cuts (Level 5)

At this stage of processing, most of the atmospheric muon events that are left in the sample are not as clearly defined as those that were previously cut. As such, two more cuts targeting these hard-to-find muons are applied— a *corridor* cut and a *containment* cut.

Corridors are regions of low instrumentation within the main IceCube array due to the hexagonal arrangement of the DOMs. These create diagonal paths where atmospheric muons can travel through avoiding detection until they reach DeepCore. The corridor cut identifies any hits located near these corridors and checks for extra hits nearby. If more

than two DOMs are hit, the event is rejected.

Containment cuts reject any event whose interaction vertex does not lie within the DeepCore fiducial volume. As a result, radial and vertical containment cuts are applied to the vertex of the event. The vertex is approximated using the string with the greatest charge output, the location of the first HLC hit, and Level 3 vertex information.

3.2.6 Pre-Reconstruction Checks (Level 6)

At Level 6, several fast algorithms are run on the sample to determine which variables are of most importance for post-reconstruction cuts performed for the improvement of the data-MC agreement. Other variables determined at this stage include those that further improve corridor and containment event rejection. The specific cuts will be discussed in more detail in Section 3.4.

3.3 Reconstruction

After processing the event sample through Level 6 for the purpose of reducing the atmospheric muon and noise background rates, a rigorous reconstruction method is applied. *Reconstruction* refers to utilizing all of the final state information of an event to predict the incident neutrino properties. Since neutrino oscillation analyses are performed by measuring the oscillation pattern as a function of the baseline, as discussed in Section 1.6, the two most important quantities to reconstruct are the incident neutrino energy and zenith angle. To achieve this, a deep-learning based reconstruction involving convolutional neural networks (CNNs) is used. The same approach is taken for reconstructing another useful quantity— the neutrino interaction vertex— with the goal of further improving the DeepCore fiducial volume containment cut. Furthermore, two classifier networks are run in an effort to categorize each event according to their Cherenkov light signature in the detector (discussed in Subsection 2.2.2) as well as to identify any remaining atmospheric

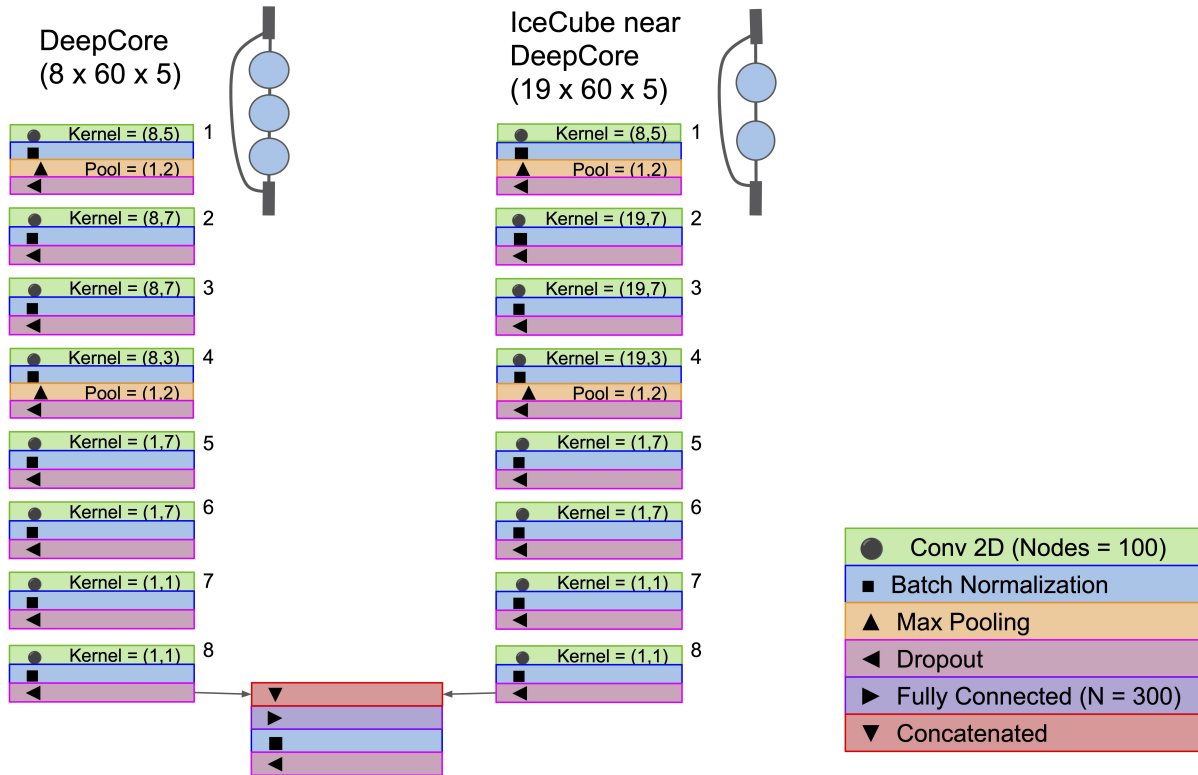


Figure 3.5: Architecture of the FLERCNN model mainly consisting of a series of 2-dimensional CNNs, batch normalization layers, max-pooling layers, and dropout layers.

muon background events. The higher the accuracy of the reconstruction and classification, the higher the visibility of the oscillation pattern.

3.3.1 Fast Low-Energy Reconstruction using CNNs (FLERCNN)

The Fast Low-Energy Reconstruction using Convolutional Neural Networks (FLERCNN) is comprised of two separate networks that are concatenated at the very end of the model. One network is optimized for the less densely-instrumented IceCube strings while the other is optimized for the more densely-instrumented DeepCore strings. Each network contains eight 2-dimensional CNNs along with a series of helper layers that assist in preventing overtraining, providing model stability, and improving image pattern recognition. The FLERCNN architecture can be seen in Figure 3.5.

3.3.1.1 Convolutional Neural Networks (CNNs)

A CNN is a type of neural network that utilizes a *kernel filter* to accentuate a specific pattern within an image. Much like its name, a CNN *convolves* the kernel function with the corresponding image pixels in order to intensify, suppress, or preserve the pixel value depending on the pattern that it wants to highlight. In general, kernels can be used to blur, sharpen, darken, or brighten an image, for example. The job of CNNs is to optimize the kernel function weights to improve the performance of the model.

The performance is calculated using a *loss function*, which is chosen such that a penalty is added whenever the network performs poorly. The lower the value of the loss function, the better the performance of the network. A loss is calculated separately for each event in the sample and averaged for all events. This way, there is one loss value that quantifies the overall performance of the network for a given choice of weights. The network, then, *backpropagates*, using an optimizer algorithm, to adjust the model weights and recalculate the loss function with the goal of minimizing the loss. Every time that the network backpropagates is called an *epoch*.

An *activation function* is typically used after a CNN layer to scale the output of the CNN into a more useful range. For example, the Rectified Linear Unit (ReLU) activation function is commonly used as it deactivates any input value lower than zero allowing for deeper network training. The last layer of the network also includes an activation function with the purpose of scaling the final output accordingly. For example, for the classification networks in FLERCNN, the Sigmoid function is used as these are binary classifications and this function restricts the output to lie between 0 and 1.

To prevent overtraining the network, two approaches are followed— dropout layers and a validation sample. A dropout layer "drops", or deactivates, a random portion of the weights and/or inputs to reduce the number of free parameters for a given epoch that the network has to optimize. This action stops any possible co-dependence between the layers that could lead to overtraining. For example, layers might attempt to correct the

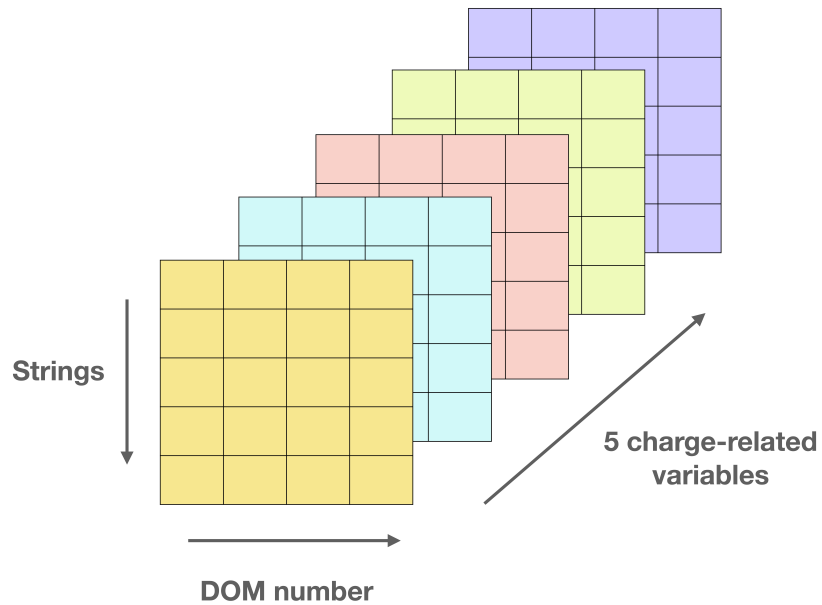


Figure 3.6: The FLERCNN inputs are 3-dimensional images of each sample event consisting in a string dimension, a DOM number dimension, and a charge-related variable dimension.

flaws from previous layers, in turn, forming a model that cannot be generalized. For each epoch, the load dropped is varied, so that, in the end, the network is still able to converge on optimal values for all weights and/or inputs.

A validation sample is used to assess the loss of the model after each epoch without bias. The training should be stopped at the point before the validation loss becomes greater than the training loss, as a higher validation loss indicates that the model is not generalizing well.

3.3.1.2 FLERCNN Training

To train the FLERCNN model, extra MC samples with uniform energy and zenith distributions were generated and processed through Level 6. A fraction of each MC sample is then used for training purposes, while the rest is divided into validation and test. After the final model is chosen based on its performance on the test sample, the real data is fed to the network to prevent any form of bias.

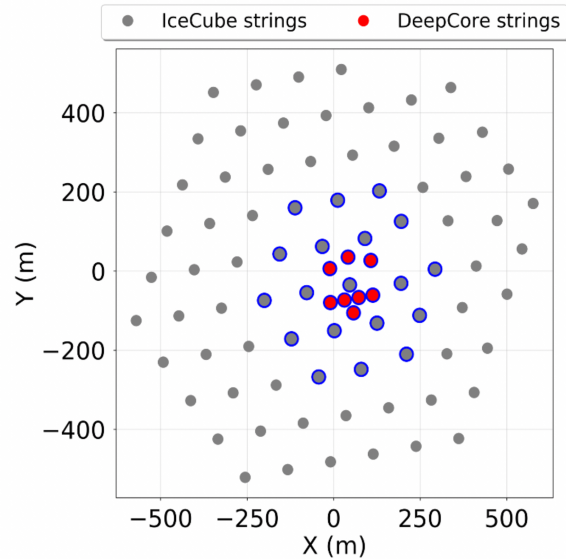


Figure 3.7: The DeepCore and surrounding IceCube strings used in the FLERCNN input images [57].

The input images consist of Level 6 cleaned events, each arranged into 3-dimensions as shown in Figure 3.6. Each image is comprised of a string dimension, a DOM number dimension, and a charge-related variable dimension. The DeepCore and surrounding IceCube strings used for each image can be seen in Figure 3.7.

The 5 charge-related variables include the total charge of the event, the time of the first hit, the time of the last hit, the mean charge of the hits, and the charge standard deviation of the hits. This particular dimension is perceived as a *channels* dimension by the CNN in a similar way to how a conventional image with three color channels (RGB) would be perceived. The CNN optimizes the kernel weights for each different channel and yields one combined output. An example of this is found in Figure 3.8. As a result, the CNN is able to handle separate channel features simultaneously and even search for cross-channel patterns.

The loss function used in FLERCNN varies depending on the purpose of the network. For example, the energy neural network uses the mean absolute percentage error loss defined as

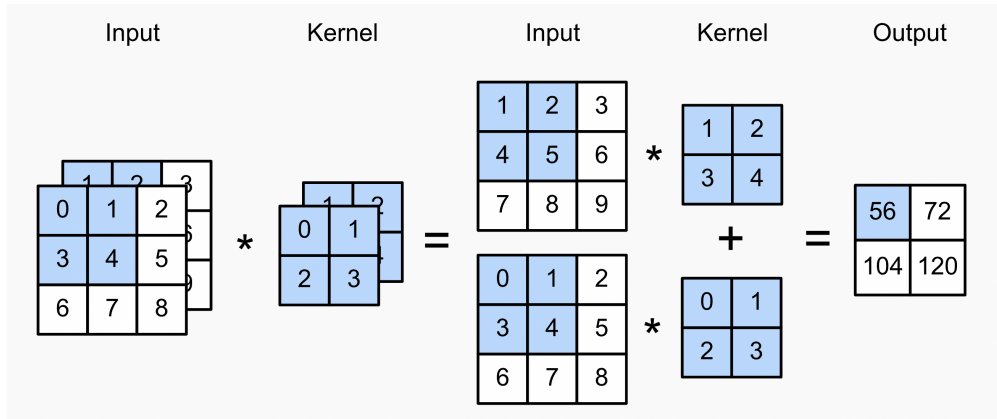


Figure 3.8: An example of how a CNN treats convolutions of separate channel inputs [17].

$$\text{Loss} = \frac{100\%}{n} \sum_{i=1}^n \left| \frac{t_i - r_i}{t_i} \right| \quad (3.1)$$

while the interaction vertex and zenith networks use the mean squared error loss,

$$\text{Loss} = \frac{1}{n} \sum_{i=1}^n (t_i - r_i)^2, \quad (3.2)$$

where n is the number of events, t_i is the true value, and r_i is the predicted value. This choice allows the energy network to equally prioritize reconstructing both high-energy and low-energy events in the sample, as opposed to prioritizing the high-energy events only. The mean absolute percentage error accounts for the *relative* difference between the true and predicted values, yielding a larger, more accurate loss at lower energies when $t_i - r_i$ is equal. The network, then, works to decrease this loss as part of the backpropagation process. Furthermore, the classification networks use the binary cross-entropy loss function, commonly used for binary classification problems as it monotonically decreases the loss as the predicted value moves closer to the 0 or 1 truth input. Figure 3.9 shows the training and validation losses for the energy and zenith CNNs as a function of the epoch number. As can be seen in the figure, the *learning rate*, or the step size of the backpropagation, decreases as the loss decreases. This was specifically chosen to fine-tune the location of the global minimum.

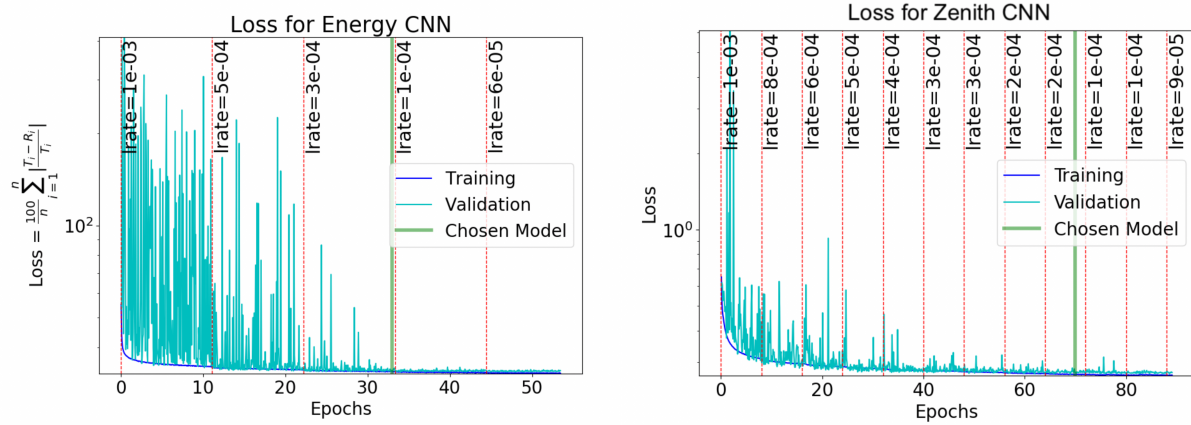


Figure 3.9: Training and validation loss for the energy network (left) and the zenith network (right) as well as the chosen model [57]. The learning rate decreases as the loss decreases in order to fine-tune the location of the global minimum.

3.3.2 FLERCNN Performance

3.3.2.1 Energy and Zenith Reconstruction

Figure 3.10 shows the FLERCNN performance for the neutrino energy and zenith as a function of the true neutrino energy. The zenith is plotted as a difference in the reconstructed and true $\cos(\theta_{zenith})$ to match Equation 1.28. Moreover, neutrino energy is plotted as the fractional energy difference between the reconstructed and true values. From the figure, it can be observed that, for both the energy and zenith, the reconstruction performance deteriorates at the lowest energies. This occurs because low-energy events produce a short-ranged Cherenkov photon signature in the detector. The large DOM spacing relative to the short range of these low-energy events causes very little signal to be detected, which in turn, leads to difficulties reconstructing these low-resolution events.

3.3.2.2 Particle Identification (PID)

Particle identification (PID) is defined as the classification of each event in the sample into one of the various signatures observed in the detector. For DeepCore, the two possible signatures include tracks and cascades as discussed in Subsection 2.2.2. Figure 3.11 shows

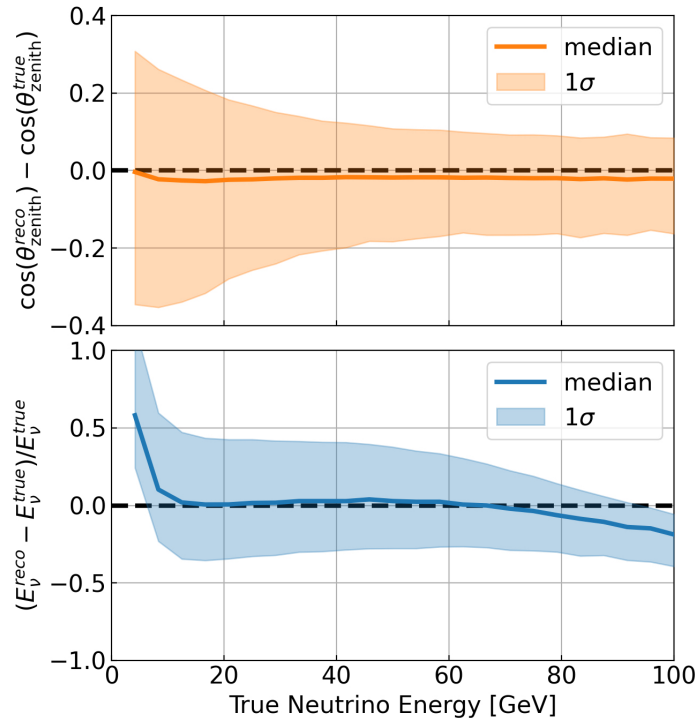


Figure 3.10: The FLERCNN reconstruction performance on the neutrino energy (bottom) and zenith angle (top) as a function the true neutrino energy [57]. The performance deteriorates at low energies due to the poor resolution of the corresponding events.

the FLERCNN classification performance on the PID, where an output score closer to 1 refers to an event being classified as more track-like while a score closer to 0 denotes more cascade-like. A peak is seen in the figure at a score of 1 for true tracks as is desirable; however, no peak is seen at a score of 0 for true cascades. This feature is understood by thinking about the geometry of track and cascade signatures. A cascade looks the same as a track with track length equal to zero. Therefore, the classifier has trouble recognizing between a pure cascade event and a very short track event. This leads to greater uncertainty whenever the network classifies an event as more cascade-like.

3.3.2.3 Vertex Reconstruction and Muon Classification

The neutrino interaction vertex is reconstructed as two separate variables— the z position of the vertex and the radial position with respect to the center-most string in IceCube.

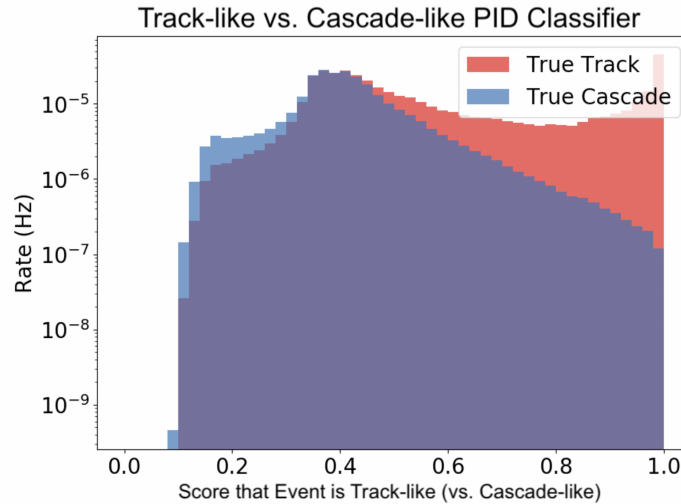


Figure 3.11: The performance of the FLERCNN PID classifier shows some discrimination power between tracks and cascades when the event is a clearly defined track [57].

Figure 3.12a shows a confusion matrix of the FLERCNN performance when placing a cut at a radius of 200 m from the center-most IceCube string. The matrix shows the percentage of events that were correctly reconstructed inside and outside of the cut in comparison to the percentage that were incorrectly reconstructed. This specific cut of the radius at 200 m will be further discussed in Section 3.4.

The atmospheric muon background classification performance can be seen in Figure 3.12b, where an output score closer to 1 indicates that an event is classified as more neutrino-like while a score closer to 0 denotes more muon-like. Due to the degree of flatness of the muon distribution seen in the plot, the FLERCNN muon classifier output is fed to a BDT as part of the final level cuts.

3.4 Final Level Cuts

A series of cuts are made at post-reconstruction level with the goal of discarding events that are most difficult to reconstruct as well as further improving background rejection. A default cut is also performed on the reconstructed neutrino energy and zenith ranges.

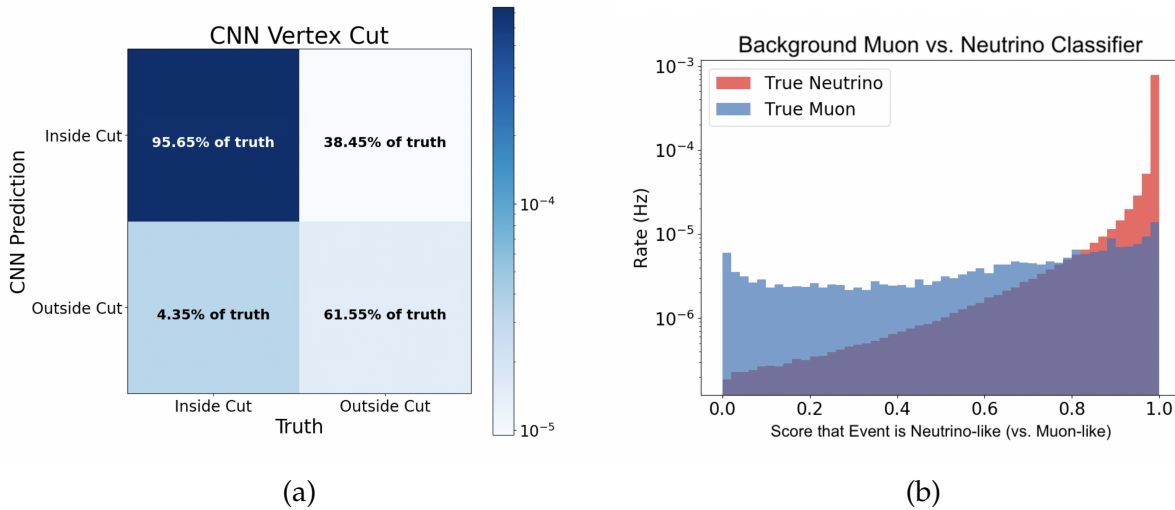


Figure 3.12: The FLERCNN performance on (a) the reconstruction of the radial component of the interaction vertex for a cut at $r = 200$ m, and (b) signal/background classification between neutrinos and atmospheric muons [57].

However, this cut is adjusted in Chapter 4 to better suit the neutrino mass ordering analysis.

3.4.1 Low Resolution and Background Rejection Cuts

Events with extremely low charge are the most difficult to reconstruct due to the large amount of undetected Cherenkov light as discussed in Subsection 3.3.2. To help mediate this, a cut is placed on the minimum number of DOM hits required for an event to be accepted. A cut is also placed on the reconstructed interaction vertex for the same purpose as well as for improved background rejection, assessing that the vertex is located inside the DeepCore fiducial volume. This cut is broken down into two quantities, a cut on the vertex z position as well as a cut on the radial position with respect to the center-most IceCube string. First alluded to in Subsection 3.3.2, a radial cut at 200 m is applied.

Additional efforts for background rejection include tighter veto cuts, a muon BDT, and a cut on the number of *direct hits*. These are mostly quantified using data-MC agreement. The veto cuts remove any events with hits in the top 15 IceCube DOM layers as well as events with 8 or more hits in the outer-most IceCube strings.

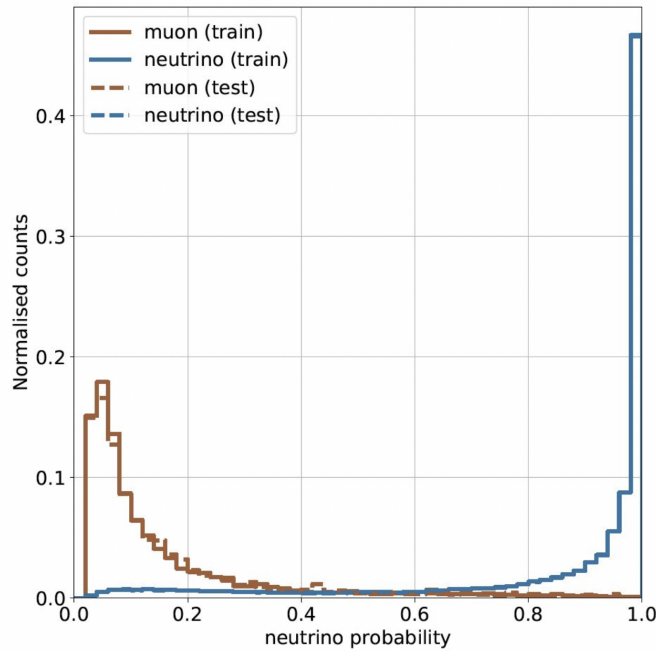


Figure 3.13: Performance of the post-reconstruction muon BDT at the final level of processing [57]. Clear discrimination power between neutrinos and atmospheric muons can be seen.

The muon BDT takes in the FLERCNN muon classification score from Subsection 3.3.2 as well as other inputs such as the FLERCNN reconstructed vertex and the Level 4 muon classifier score with the goal of separating muons from neutrinos. The BDT performance can be seen in Figure 3.13, where clear signal/background discrimination is observed.

To remove any remaining noise hits, a cut is made on the number of direct hits in an event requiring at least 3 hits. "Direct hits" originate from photons that did not scatter in the ice. This feature is calculated using the SANTA [41] framework by determining whether the detected photon properties match those of a Cherenkov cone. Table 3.1 shows the values chosen for each of the final level cuts described.

| Final Level Cuts | |
|--------------------|-------------------------|
| Type | Value |
| DOM hits | ≥ 7 |
| Reco radius | < 200 m |
| Reco z | -495 m $< z < -225$ m |
| Direct hits | > 2.5 |
| IceCube top 15 | < 0.5 |
| IceCube outer-most | < 7.5 |
| Muon BDT | ≥ 0.8 |

Table 3.1: All post-reconstruction cuts applied at the final level of processing with the goal of removing extremely low-resolution events as well as improving background rejection. The cut for the reconstructed vertex z position is shown with respect to the IceCube coordinate system, which places the origin at 1948.07 m below the surface.

3.4.2 Default Energy and Zenith Cuts

For completeness, a default cut is made on the reconstructed neutrino energy and zenith ranges preserving the essential signal region of oscillation-related analyses. Events range from energies of [5, 100] GeV and $\cos(\theta_{zenith})$ values of [-1, 0.3]. The cut on the zenith angle provides further atmospheric muon rejection and prevents *self-veto* effects. Self-veto effects arise when coincident muon and neutrino events originating from the same air shower get discarded during the processing of real data, while, during the MC processing, neutrinos from these type of events survive due to coincidences not being simulated.

These cuts are further evaluated in Chapter 4 and adjusted to better fit the signal region for the work presented in this dissertation— the neutrino mass ordering analysis.

Chapter 4

Analysis of the Neutrino Mass Ordering

4.1 Premise of the Analysis

As stated at the end of Section 1.5, matter effects resonate for *neutrinos* only if the normal ordering (NO) is true. Conversely, if the inverted ordering (IO) is true, matter effects resonate for *anti-neutrinos*. It follows, then, that, to measure the neutrino mass ordering (NMO), one would simply need to match the matter-enhanced oscillation pattern to its correct source. This is more easily seen in Figure 4.1, where the oscillation probability is plotted for muon neutrinos and anti-neutrinos as a function of the incident neutrino energy and $\cos(\theta_{zenith})$. For atmospheric neutrino/anti-neutrino events in DeepCore, matter effects take place at energies of about 2.5 GeV to 15 GeV. The magnitude of these effects is highly dependent on the oscillation parameter θ_{23} , and as a result, so is the analysis sensitivity. This concept will be further explored in Chapter 6.

From the figure, it can be inferred that a crucial part of the analysis consists in separating neutrino from anti-neutrino events. DeepCore, however, does not have this capability as both types of events create the same track and cascade Cherenkov signatures in the detector (described in Subsection 2.2.2). Thus, this analysis relies on the differences in the flux and cross-section of neutrinos and anti-neutrinos. Mainly, the flux and cross-

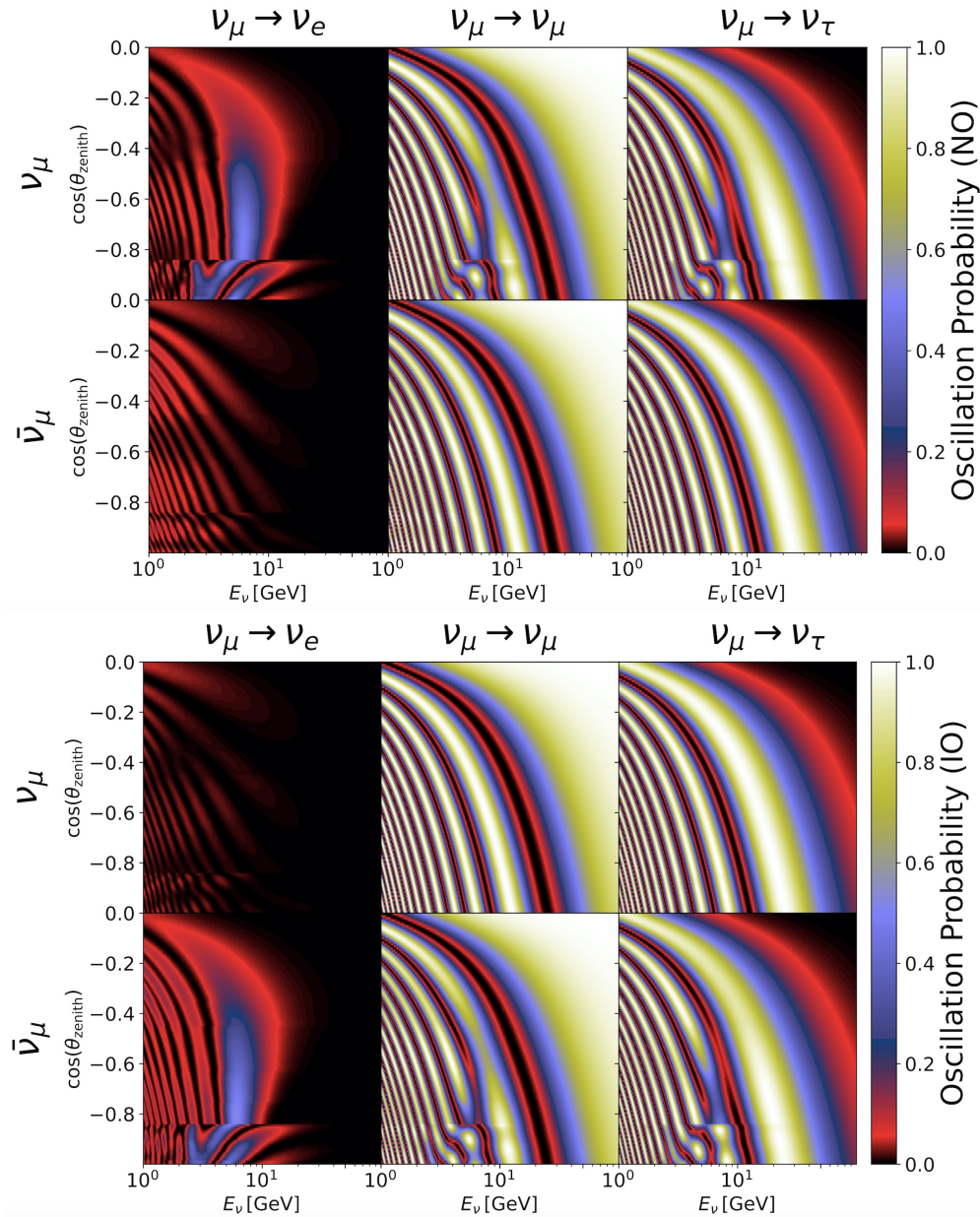


Figure 4.1: Matter-enhanced muon neutrino and anti-neutrino oscillation probabilities for true NO (top) and true IO (bottom) as functions of the incident neutrino energy and $\cos(\theta_{zenith})$ [59].

section are both higher for neutrinos in the region of interest as compared to anti-neutrinos (Figs. 1.5 and 1.10). The target signal, then, for the combined neutrino and anti-neutrino sample, although suppressed, survives as a difference in the magnitude of the matter effects, yielding stronger effects for true NO and weaker effects for true IO.

4.2 9.28-Year Analysis Sample

Event distributions are assembled as functions of the reconstructed E_ν , $\cos(\theta_{zenith})$, and PID for the MC simulation sample and the observed data sample described in Chapter 3. The MC distribution is then used to measure the oscillation features found in the observed data distribution through a fit of the oscillation and systematic parameters of the analysis. Before fitting the observed data, however, a *MC only* analysis is developed to check the validity of the various analysis choices as well as to quantify the projected significance of the mass ordering measurement. This approach is taken so as to prevent any injection of bias on the measured result from a *post-unblinding* change to the analysis. A fit to the observed data is performed starting from Chapter 7.

4.2.1 Binning

The binning used for the event distributions is specifically chosen so as to optimize the signal region of the analysis (described in Section 4.1). It consists of

- **Energy:** 20 \log_{10} -spaced bins between 3 and 100 GeV
- **Cos(θ_{zenith}):** 20 linearly-spaced bins between -1.0 and 0
- **PID:** 3 bins with edges at [0, 0.33, 0.39, 1.0]

This particular binning modifies the default energy and zenith cuts, mentioned in Subsection 3.4.2, by placing a slightly tighter cut on the $\cos(\theta_{zenith})$ and extending the energy range down to 3 GeV. The $\cos(\theta_{zenith})$ cut is made with the intention of further rejecting atmospheric muon events and events following from self-veto effects. Additionally, the lower energy limit is extended to conserve as much of the NMO signal region as possible while considering the reconstruction limitations imposed by FLERCNN.

The extraction of the signal is improved by using a logarithmic scale to make the bin width smaller at low energies. The bin content is also carefully assessed for the purpose

of maintaining a statistically stable analysis. Mainly, a minimum threshold of 5 expected events and 100 raw MC events per bin is imposed to avoid statistical fluctuations.

It is important to note that, although the bin width is subdivided further than the corresponding reconstruction resolution, the analysis remains stable due to the minimum threshold imposed in the number of events per bin. Fundamentally, the stability of the analysis is determined by its statistical stability. As such, the subdivision of bins should be halted when either any given bin shows signs of statistical instability due to a low number of bin counts or the sensitivity improvement plateaus due to reconstruction limitations. Nevertheless, in the latter case, bin subdivision is still possible, however, one is left with a much greater computational effort without gaining any benefit, so it is not recommended.

If statistical stability is obtained through a large sample size, as is the case for this analysis, and there is a sizeable improvement in the sensitivity, a finer binning is justified. Taking this into consideration, along with all of the previously mentioned binning choices optimized to target the NMO signal, the sensitivity is observed to increase by roughly 60% in comparison to the default case with 12 energy bins and $8 \cos(\theta_{zenith})$ bins.

The final piece of the binning scheme consists in selecting the PID decision boundaries, which are based on the FLERCNN PID performance discussed in Subsection 3.3.2. There are three PID bins—the cascade bin, the *mixed* bin, and the track bin. The mixed bin holds events with higher uncertainty in their PID score mostly due to their low-purity nature. The PID bins for this analysis are shown in Figure 4.2, where the cascade bin is represented by $P_{track} < 0.33$, the $0.33 < P_{track} < 0.39$ bin holds mixed events, and $0.39 < P_{track}$ denotes tracks. In general, decision boundaries adjust these bounds in order to maximize the discrimination power of the PID. For this analysis, although a conscious effort is made to optimize the discrimination power of the PID, another feature is regarded as more critical—fulfilling the minimum threshold imposed in the number of events per bin. This can be seen in Figure 4.2, where the plot on the right shows the total number of events in each PID bin to be similar instead of one bin holding a much greater number of events compared to

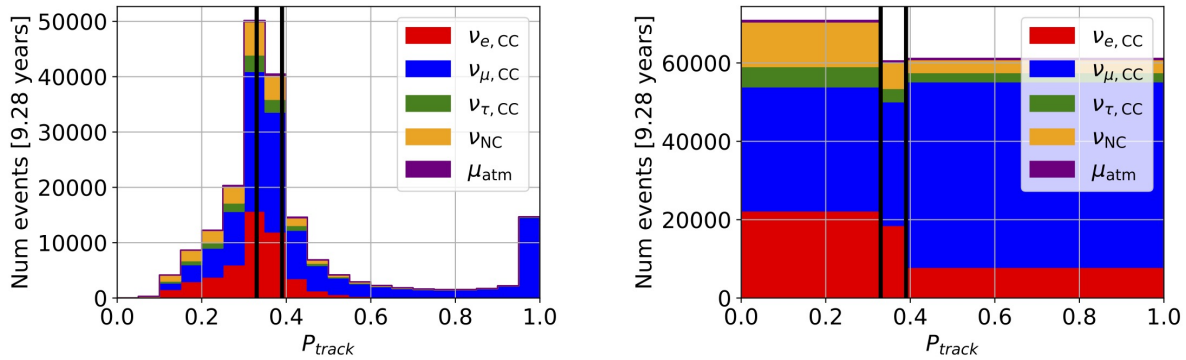


Figure 4.2: Particle identification (PID) distributions with 20 bins (left) and 3 bins (right) stacked by event type. Track-like events are denoted by scores closer to 1 while cascade-like events lie closer to 0. Decision boundaries are optimized for this analysis to improve track/cascade discrimination as well as to populate each PID bin as evenly as possible for statistical stability.

the other bins.

4.2.2 MC Simulation Templates

Figure 4.3 shows the event distribution templates for the case of true NO (top) and true IO (bottom) at the *nominal* MC expectation for 9.28 years of detector data with the chosen analysis binning. Conducting a fit of the oscillation and systematic parameters is expected to change the bin counts as a result of varying the parameter values.

Reconstruction effects on the analysis template can be seen in Figure 4.4, where the NO event distribution is plotted as a function of the *true* energy and $\cos(\theta_{zenith})$. By comparing the true and reconstructed templates, one can visualize the amount of dilution in the oscillation features that occurs as a result of reconstruction.

Additionally, Figure 4.4 validates the objective of the PID decision boundaries. Mainly, for both the track and cascade bins, a greater number of events are observed to lie at higher energies which is expected due to the higher resolution of these events that lead to better-defined PID scores. In contrast, for the mixed bin, the majority of events lie at low energies as a result of low purity and greater uncertainty in the PID scores.

Event counts as well as their corresponding rates are listed in Table 4.1 for the finalized

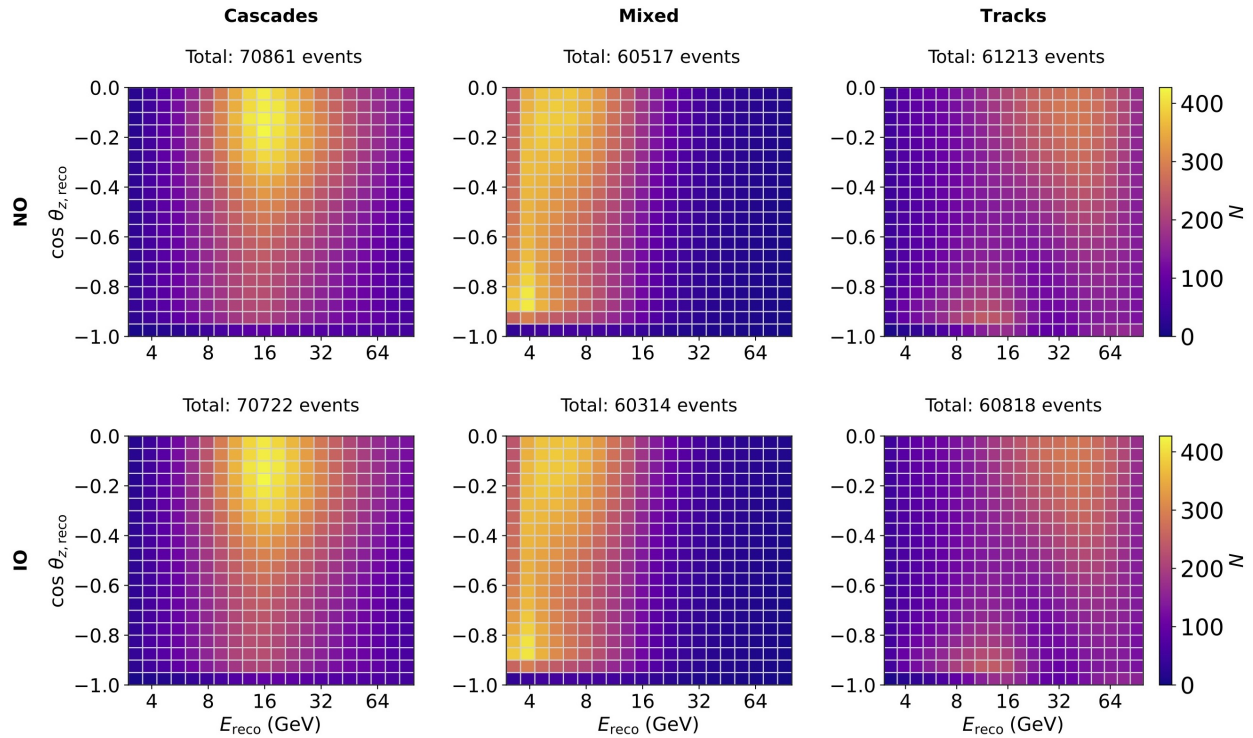


Figure 4.3: Analysis-level MC simulation templates assuming true NO (top) and true IO (bottom) using reconstructed quantities.

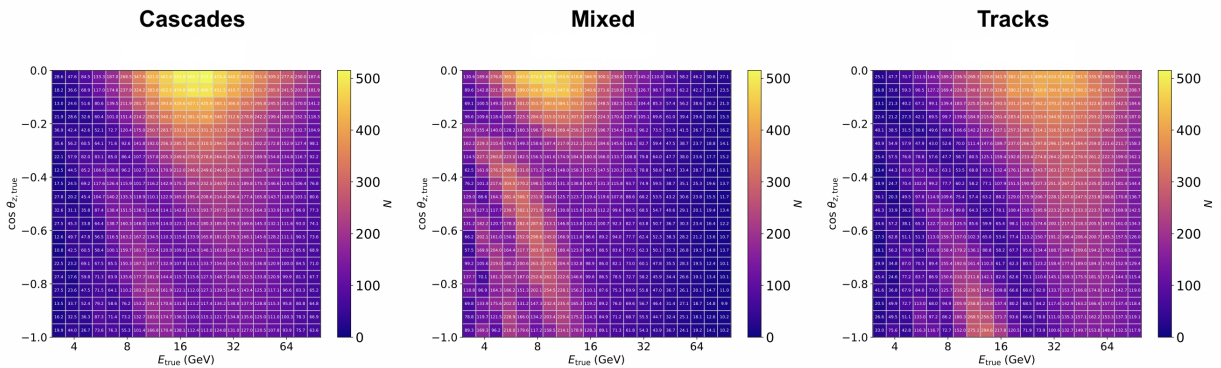


Figure 4.4: MC simulation template using true energy and $\cos(\theta_{zenith})$ values and assuming true NO. Oscillation fringes can be observed for all three PID signatures.

NMO analysis sample. It is important to note that noise events are negligible at the analysis level, and thus, are not included.

| Type | Counts [9.28 years] | Rate [μHz] | % of Sample |
|--|---------------------|-------------------------|-------------|
| All MC | 192,605 | 0.658 | - |
| $\nu_{\text{all}} + \bar{\nu}_{\text{all}}$ NC | 21,412 | 0.073 | 11.1 |
| $\nu_e + \bar{\nu}_e$ CC | 48,637 | 0.166 | 25.3 |
| $\nu_{\mu} + \bar{\nu}_{\mu}$ CC | 110,645 | 0.378 | 57.4 |
| $\nu_{\tau} + \bar{\nu}_{\tau}$ CC | 10,936 | 0.037 | 5.7 |
| muons | 973 | 0.003 | 0.5 |

*Values are for Normal Ordering

Table 4.1: Expected event rate for 9.28 years of detector livetime separated by event types. Each value is calculated using the nominal parameter values.

4.2.3 Muon Template Smoothing

As a result of the low number of atmospheric muon events in the analysis sample, the muon MC template is observed to have sharp features that are not suitable to represent the real data as seen in the left-hand plots of Figure 4.5. To mediate this issue, a kernel density estimator (KDE) is used to smear the template. The KDE implementation spans the entire $(E_{\nu}, \cos(\theta_{\text{zenith}}))$ parameter space beyond the analysis binning to improve the event accuracy at the edges of the smoothed template. The smoothed muon template, including KDE implementation, can be seen in the right-hand plots of Figure 4.5.

4.3 Uncertainties

Uncertainties for this analysis (with the exception of statistical uncertainties) can be broadly categorized into three classes— systematic uncertainties, oscillation uncertainties, and normalization uncertainties. As previously discussed, these are included in the analysis as free parameters with nominal expectation values and ranges based on external constraints. Varying any given parameter modifies the number of expected events by either weighing each individual event, each individual bin (in the case of detector systematics), or the entire template (for normalization). In total, 50 parameters are assessed. Section 4.6 delves into the details of this assessment and the studies performed to quantify the impact of each parameter on the analysis. As a result, parameters with a negligible impact are fixed.

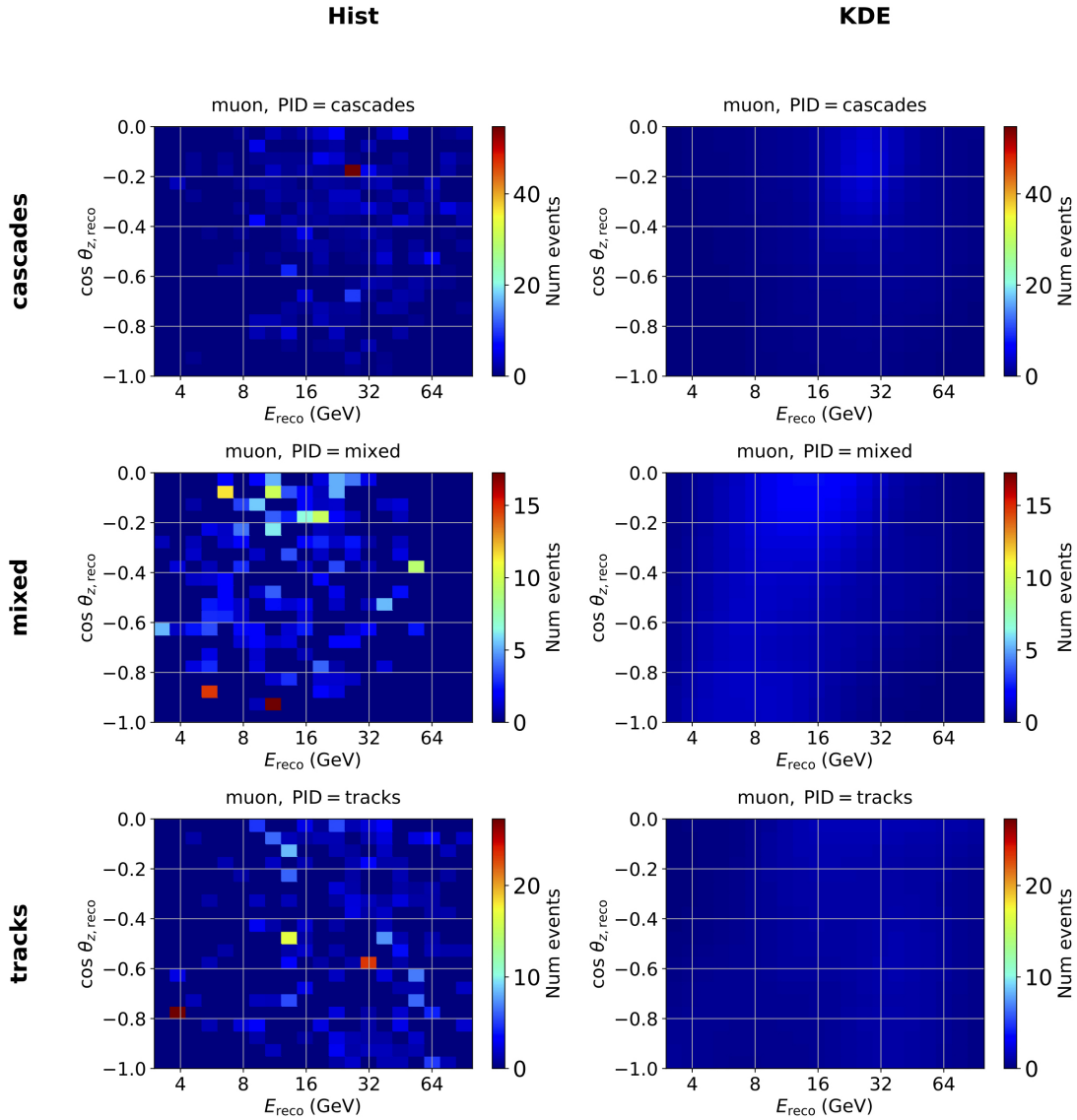


Figure 4.5: The MC atmospheric muon template with (right) and without (left) the implementation of a kernel density estimator (KDE). The KDE serves to smooth out the sharpness of the template, resulting from the low number of muon events in the analysis sample.

4.3.1 Systematic Uncertainties

Systematic uncertainties include uncertainties in the atmospheric flux, the incident neutrino cross-section, and detector properties (described in Section 2.3). These are accounted for using the following systematic parameters.

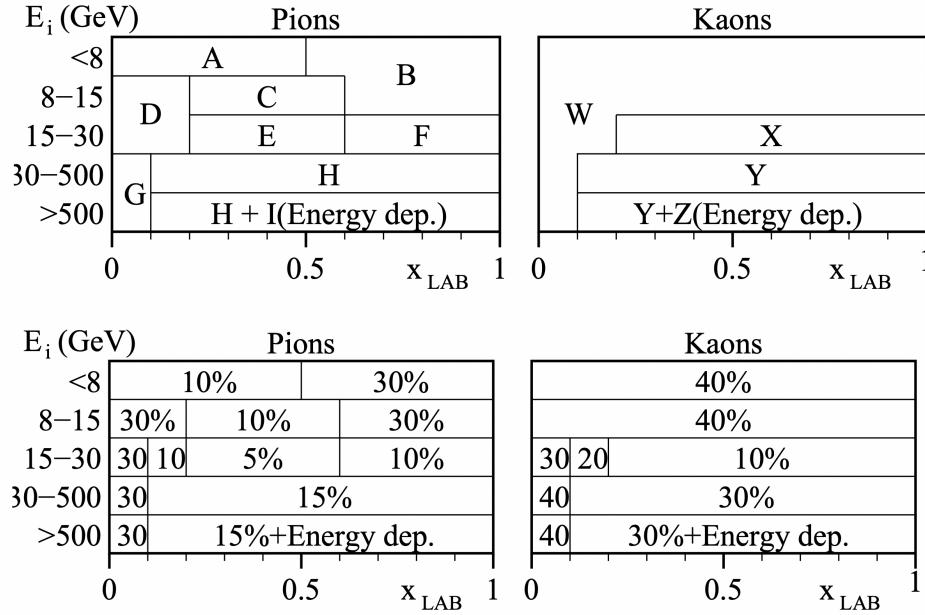


Figure 4.6: Pion and kaon production Barr blocks [20]. E_i denotes the energy of the primary cosmic ray and $x_{\text{LAB}} = E_s/E_i$, where E_s is the energy of the secondary hadron.

4.3.1.1 Atmospheric Neutrino Flux

The atmospheric flux is calculated using

$$\Phi(E) = \Phi_{\text{nominal}} \left(\frac{E}{E_{\text{pivot}}} \right)^{\Delta\gamma} + \sum_{i=1}^{N_{\text{Barr}}} B_i \cdot \frac{d\Phi_{\text{nominal}}}{dB_i} \quad (4.1)$$

where the first and second terms denote a dependency on the primary cosmic ray model [31] and the hadronic interaction model [20], respectively. The first term varies as a function of the atmospheric neutrino flux spectral index, $\Delta\gamma$, while the energy pivot, E_{pivot} , is set to a fixed value of 24.09 GeV [41]. The second term varies as a function of B_i , or the uncertainty of each *Barr block* found in Figure 4.6.

Barr blocks represent pion and kaon production uncertainties derived from existing experimental data for different portions of the $E_i(x_{\text{LAB}})$ phase space. Here, E_i denotes the energy of the primary cosmic ray and $x_{\text{LAB}} = E_s/E_i$, where E_s is the energy of the secondary hadron. Two energy dependent terms are included at $E_i > 500$ GeV to make up for the lack of data available from accelerator experiments. It is important to note that the

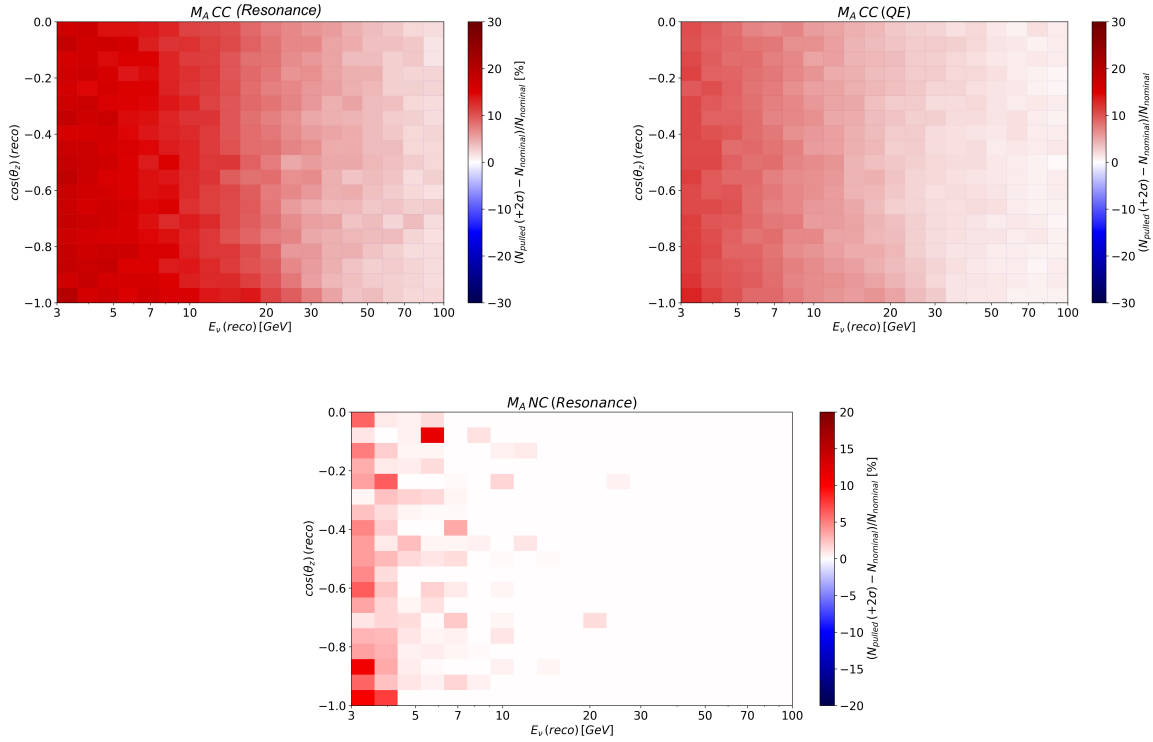


Figure 4.7: Event distributions for $M_{A,RES}$ (CC and NC) and $M_{A,QE}$ (CC) denoting the relative percentage difference in the number of expected events between the nominal and 2σ variation values of the parameter. Greater difference is seen towards lower energies as expected.

pion uncertainties listed in Figure 4.6 correspond to π^+ uncertainties only. To account for π^- uncertainties, the pion ratio, π^+ / π^- , is used as this is better constrained. The quantity $\frac{d\Phi_{nominal}}{dB_i}$ is calculated using the MCEq software [16].

4.3.1.2 Neutrino Cross-Section

Neutrino cross-section uncertainties mainly come from an uncertainty on the neutrino-nucleon interaction form factor, as this has not been well-constrained experimentally. The form factor is a function of the momentum transfer, Q , and depends on the value of the *axial mass*, M_A , so that

$$F(Q^2) \propto \left(1 - \frac{Q^2}{M_A^2}\right)^{-2}. \quad (4.2)$$

Essentially, the axial mass affects the magnitude of the total cross-section such that, as the axial mass increases/decreases, so does the total cross-section. Three axial mass parameters are considered in this analysis in order to account for uncertainties in quasi-elastic (QE) CC interactions as well as resonant (RES) CC and NC interactions.

To determine the variation in the number of expected events due to a change in the axial mass parameters, a cross-section weight is calculated using GENIE [18]. To lower the computational time, the weight is quantified for 5 representative values of the axial mass followed by an interpolation of these values. Figure 4.7 shows event distributions for $M_{A,RES}$ (CC and NC) and $M_{A,QE}$ (CC) denoting the relative percentage difference in the number of expected events between the nominal and 2σ variation values of the parameter. Greater differences are seen towards lower energies, and, in particular, the greatest difference is seen for $M_{A,RES}$ CC, as expected from the signal region of this analysis.

Additionally, a deep-inelastic scattering (DIS) parameter accounts for uncertainty stemming from a mismatch between the GENIE [18] and CSMS [12] cross-section values at energies above 100 GeV. As a result, this parameter interpolates between the two models to, then, extrapolate the cross-section at lower energies.

To account for different ν_τ cross-section models [11], a ν_τ cross-section scale parameter is implemented as a correction factor. Studies involving other cross-section parameters can be found in Appendix A. These are shown to be negligible for this analysis and are not further considered in this work.

4.3.1.3 Detector Properties

Detector uncertainties arise from uncertainties in the DOM calibration as well as in the optical ice properties as discussed in Section 2.3. These consist of the DOM efficiency, the bulk ice scattering of photons, the bulk ice absorption, and the hole ice p_0 and p_1 parameters. Each uncertainty is treated as a separate systematic parameter in the analysis.

Nuisance parameters for birefringence (BFR) and the muon light yield are also incorporated to account for uncertainties in the different models used. In the case of BFR, a parameter was introduced in the analysis to interpolate between the newly completed BFR ice model [35] and the previous baseline model, SPICE [27]. For the muon light yield parameter, inconsistencies were found post-simulation with the configuration of the PROPOSAL software [26] for muon propagation leading to a non-negligible overestimation of the muon light yield and imprecise muon propagation lengths at low energies. To reduce the computational effort that it would take to rerun the entire MC simulation, a parameter was introduced to interpolate between the muon light yield calculated using PROPOSAL and GEANT4 [37].

To calculate the variation in the number of expected events resulting from changing the detector parameters, a *hypersurface* method is applied as a result of an analytic function not being known. Hypersurfaces are N-dimensional bin-wise fits of the event counts derived from varying the detector parameters in discrete MC simulation sets. In total, there are 32 MC sets plus the nominal set, all of which get processed up to the analysis level. For each MC set, a *re-weight factor* is calculated as the ratio of the expected counts of that set and the nominal set. The re-weight factor, thus, represents a conversion factor between the expected counts of the two sets used to generate it. For each bin, there are 32 re-weight factors, which span an N-dimensional parameter space. Here, N denotes the number of detector parameters plus an offset parameter; hence, $N = 8$ for this analysis. A linear *hypersurface* fit is then conducted of the gradients of each parameter and the offset to obtain the expected variation in the bin counts for a range of detector values. Note that a linear fit is used as this showed comparable results to higher-polynomial fits but was most stable. Figure 4.8 shows an example of a one-dimensional hypersurface fit for the DOM efficiency parameter for a given bin.

Due to the bin-wise nature of the hypersurface method, the re-weight ratios calculated from expected bin counts are only exact at the nominal values of non-detector parameters.

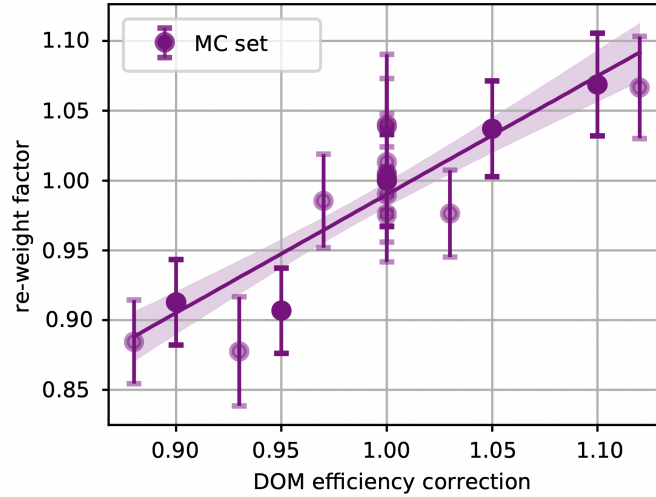


Figure 4.8: Example of a slice of the hypersurface for the DOM efficiency parameter. The re-weight factors are plotted for all MC simulation sets and fitted using a linear fit [41].

More precisely, a dependence exists on all of the analysis parameters as a result of the variation in expected bin counts due to a change in the parameter values. To account for this, hypersurfaces are generated for several representative values of each non-detector parameter that was found to have a non-negligible dependence. A piece-wise linear interpolation of the gradients and the offsets is then performed for each bin. The parameters found to have a non-negligible dependence consist of the oscillation parameters, θ_{23} and Δm_{31}^2 , as well as the neutrino flux spectral index, $\Delta\gamma_\nu$.

In general, hypersurfaces are fitted separately for three different categories of neutrino flavors:

- $(\nu_e + \bar{\nu}_e)$ CC and $(\nu_{\text{all}} + \bar{\nu}_{\text{all}})$ NC
- $(\nu_\mu + \bar{\nu}_\mu)$ CC
- $(\nu_\tau + \bar{\nu}_\tau)$ CC

This accounts for differences in detector effects that can occur depending on the type of event signature. The first two categories correspond to cascades and tracks, respectively. Although $(\nu_\tau + \bar{\nu}_\tau)$ CC interactions mostly yield cascade-like signatures, a track-like signa-

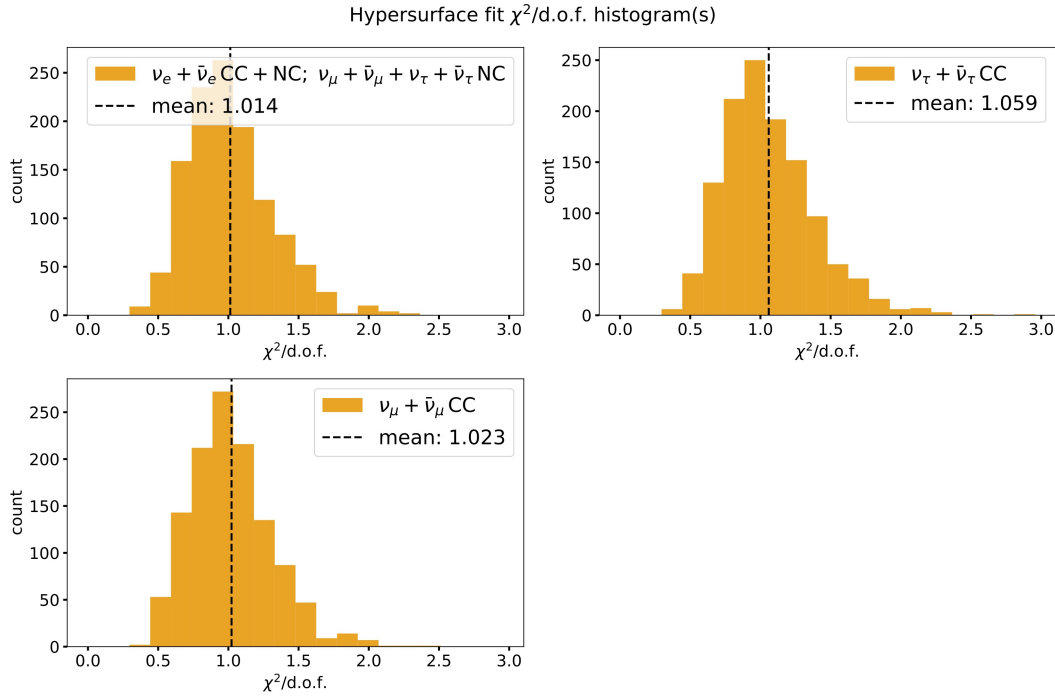


Figure 4.9: 1-dimensional distributions of the bin-wise reduced χ^2/DOF for each neutrino flavor signature. A mean value close to 1 is expected for each distribution to ensure the validity of the hypersurfaces.

ture is expected 17% of the time due to the branching ratio of the tau particle. As a result of this as well as the imposed tau production threshold, $(\nu_\tau + \bar{\nu}_\tau)$ CC hypersurfaces are fitted separately.

To gauge the statistical stability of the hypersurfaces, the bin fit reduced χ^2 is divided by the number of degrees of freedom (DOF), where $\text{DOF} = N_{\text{fitted points}} - N_{\text{params}}$. Here, $N_{\text{fitted points}}$ corresponds to the number of fitted re-weight factors and N_{params} is the number of free parameters.

Figure 4.9 shows the distributions of the bin-wise reduced χ^2/DOF for this analysis pertaining to each flavor signature. To ensure the validity of the fits, the mean value of each distribution is expected to be close to 1. This is observed to be true in the figure. Furthermore, the information in Figure 4.9 can be expanded into 3-dimensional distribu-

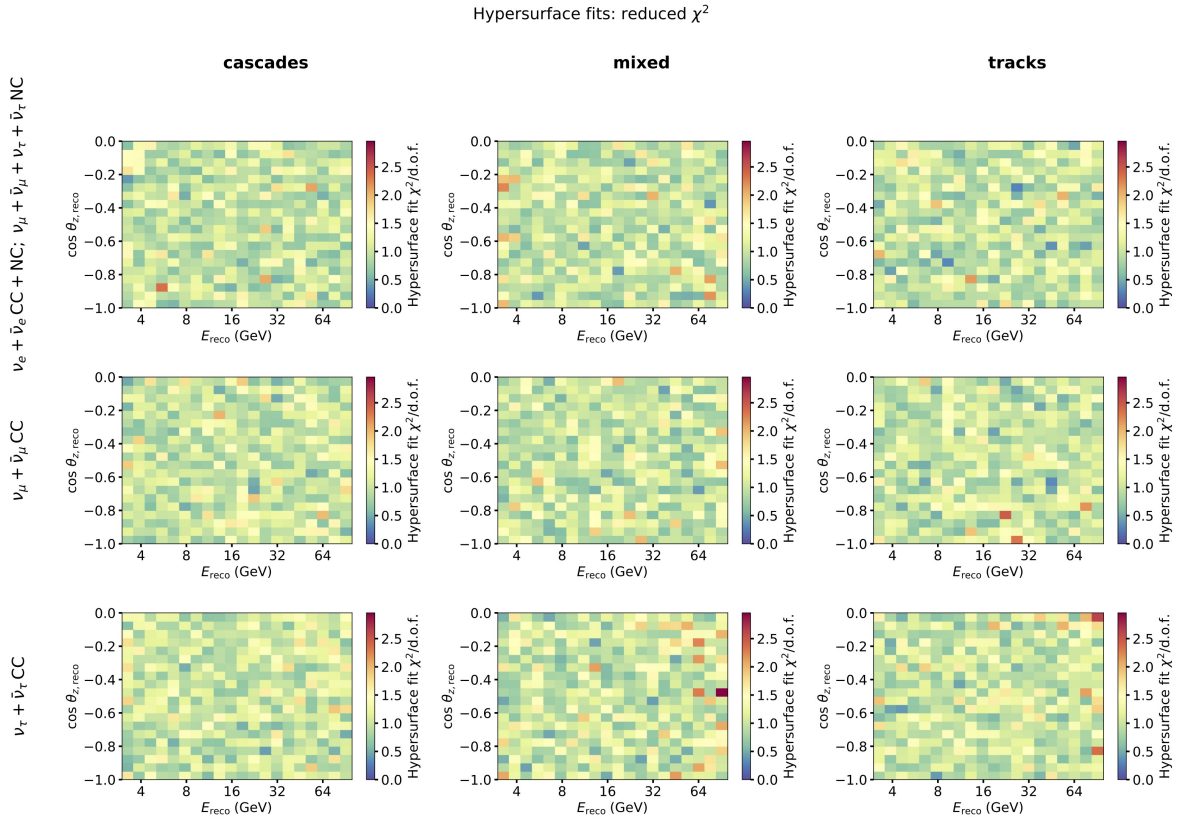


Figure 4.10: 3-dimensional hypersurface distributions of the reduced χ^2/DOF separated by neutrino flavor. No clustering effects are seen at the higher χ^2 values as well as no uncharacteristically high χ^2 value for any individual bin, showing hypersurface stability.

tions to assess the χ^2/DOF at each individual bin. This is shown in Figure 4.10, where no clustering effects are seen at the higher reduced χ^2 values.

4.3.2 Oscillation and Normalization Uncertainties

The oscillation parameters consist of the Earth model and corresponding density parameters, the detector depth, the atmospheric neutrino generation height, and the neutrino oscillation parameters discussed in Section 1.8. The Earth model used for this analysis is the 12-layer approximation of the preliminary reference Earth model (PREM) [14], which is parametrized by three density parameters denoting the inner Core, outer Core, and

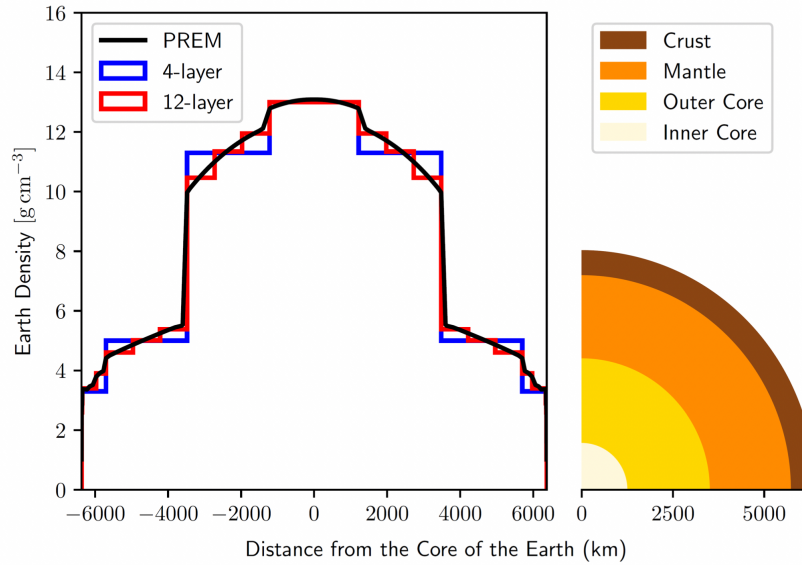


Figure 4.11: Earth density as a function of the distance from the Core of the Earth for PREM as well as the 12-layer and 4-layer approximations [40].

Mantle such that

- Y_e Inner Core parametrizes 1 layer
- Y_e Outer Core parametrizes 3 layers
- Y_e Mantle parametrizes 8 layers

Figure 4.11 shows the Earth density as a function of the distance from the Core of the Earth for PREM as well as the 12-layer and 4-layer approximations. The density of the Earth is a crucial component for matter effects (Section 1.5) to occur.

The Prob3++ software [36] is used to calculate the neutrino oscillation probability. In this calculation, the Earth densities as well as the detector depth and neutrino generation height are kept fixed. The corresponding oscillation probability is then applied as a weight to each event.

For normalization uncertainties, a neutrino normalization factor, N_ν , scales the MC template to account for a variation in total neutrino counts due to flux uncertainties as

well as the various cuts performed during processing, which can remove neutrinos from the sample.

4.3.3 Atmospheric Muon Uncertainties

As a result of atmospheric muon events comprising only 0.5% of the analysis sample (Table 4.1), systematic effects on these are found to be small. Thus, only an atmospheric muon flux spectral index parameter and an overall muon normalization scale factor are considered. These parameters effectively account for all muon systematic effects. Similarly, muon hypersurfaces are found to be negligible and, therefore, not used.

4.4 Test Statistic

A fit of the MC simulation template is assessed using a binned Poisson log-likelihood (LLH) metric such that

$$L = \prod_i^{N_{bins}} \frac{\lambda^{k_{data,i}} e^{-\lambda_i}}{k_{data,i}!} \quad (4.3)$$

$$LLH = \sum_i^{N_{bins}} \log \left(\frac{\lambda^{k_{data,i}} e^{-\lambda_i}}{k_{data,i}!} \right),$$

where λ_i and $k_{data,i}$ are the expected and observed event counts for a given bin i , respectively. A prior penalty based on external constraints is added to the LLH in the form

$$LLH_{prior} = \frac{1}{2} \sum_j^{N_{const}} \left(\frac{s - s_0}{\sigma_j} \right)^2, \quad (4.4)$$

where N_{const} is the number of parameters with external constraints, s and s_0 are the parameter template and nominal values, respectively, and σ_j is the uncertainty on the parameter represented by its 1σ prior. In essence, the prior serves to penalize the fit for

values that lie far from the nominal value.

The test statistic for this analysis is constructed, then, as a difference in the LLH such that

$$\Delta\text{LLH}_{\text{NO-IO}} = |\text{LLH}_{\text{NO}}| - |\text{LLH}_{\text{IO}}|, \quad (4.5)$$

where LLH_{NO} and LLH_{IO} denote the LLH value from a fit of the analysis parameters assuming a true NO and a true IO, respectively. An in-depth discussion of the treatment of the test statistic is provided in Section 6.1.

4.4.1 Treatment of limited MC Statistics

Statistical uncertainty exists in the number of expected events in a given bin due to the finite MC generation. This is normally accounted for in the metric of the analysis by including a value, σ , representing this uncertainty. Looking closely at the LLH definition from Equation 4.3, however, one can see that no σ value is included. Instead, to incorporate this uncertainty, a *convoluted LLH* metric can be computed. The convoluted LLH is defined as the log of the convolution of the Poisson likelihood, p , with a Gaussian distribution, n , centered at zero so that

$$\begin{aligned} \text{Convoluted LLH} &= \sum_i^{N_{\text{bins}}} \log((p * n)(k_{\text{data},i}, \lambda_i, \sigma_i)) \\ &= \sum_i^{N_{\text{bins}}} \log\left(\int p(k_{\text{data},i}, \lambda_i - x)n(x, \sigma_i)dx\right), \end{aligned} \quad (4.6)$$

where σ_i is the uncertainty on the expected number of events for a given bin. In essence, this metric weighs all values around the expected value according to how far away they are, where the farther the value is from the expected value, the smaller the weight.

After computing the optimized analysis fit using both the LLH and convoluted LLH, similar values are obtained, denoting a negligible MC generation statistical uncertainty.

| Metric | Value after Optimization |
|---------------|--------------------------|
| LLH | 0.343 |
| Convolved LLH | 0.339 |

Table 4.2: Optimized LLH and convoluted LLH values for a fit of the IO theory template assuming an NO "observed" data template. Similar values are observed for both, denoting a negligible impact of MC generation statistical uncertainty. The NO data template uses the nominal parameter values except for the θ_{23} parameter, which is set to the more representative value of 45° .

This can be seen in Table 4.2. Consequently, the LLH is adopted as the analysis metric as it yields the lower computational time.

4.5 Optimization

The analysis metric is optimized using MINUIT [48] with MIGRAD implementation. The optimization is carefully performed twice, once for each *octant* of the θ_{23} oscillation parameter, with the upper and lower octants corresponding to $\theta_{23} > 45^\circ$ and $\theta_{23} < 45^\circ$, respectively. This helps the optimizer better identify the true global optimum as the phase space is almost identical in both octants—a feature stemming from the octant degeneracy created by the $\sin^2(2\theta_{23})$ term in the oscillation probability. A meticulous look at the oscillation probability shows that, in the full three-flavor paradigm with matter effects, sub-leading terms break this degeneracy. However, as the difference is not significant, separate octant optimizations are necessary.

The performance of the optimizer is assessed through various checks on the analysis MC template. First, the same optimization is performed across the entire θ_{23} range with both the analysis optimizer as well as a more robust and computationally intensive optimizer using the controlled random search 2 (CRS2) algorithm [50] along with MINUIT [48]. The optimization was found to yield almost equal values.

Secondly, the optimized bin-wise metric is examined. Figures 4.12 and 4.13 show the

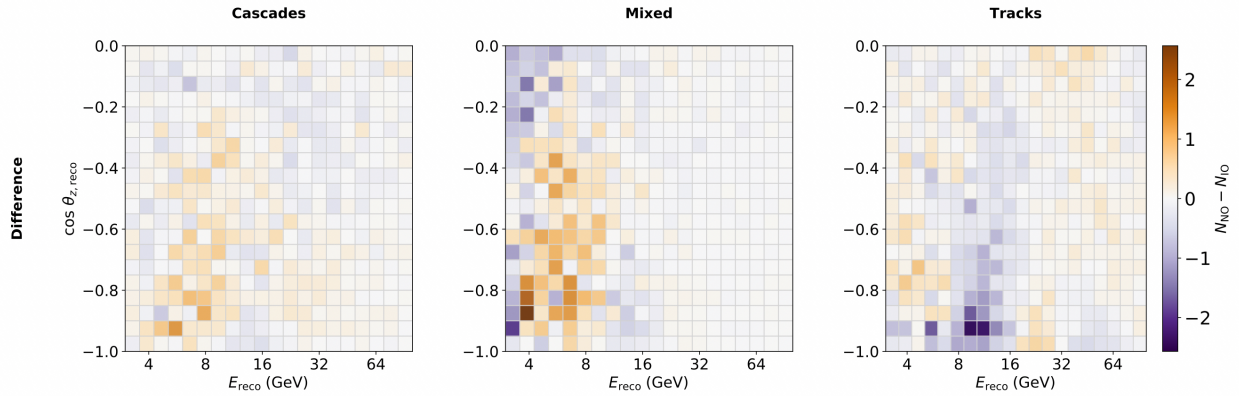


Figure 4.12: Expected event difference between the optimized IO theory template and the assumed NO "observed" data template.

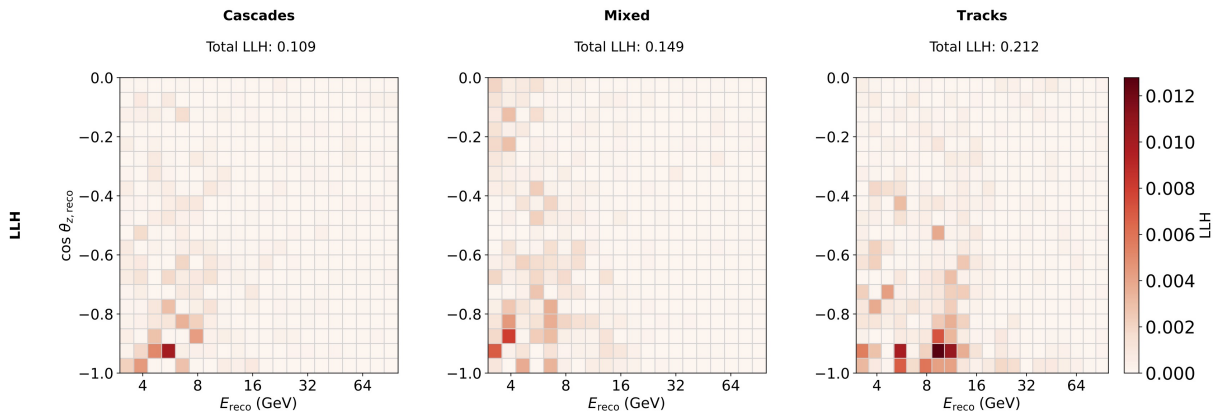


Figure 4.13: Optimized bin-wise LLH produced from a fit of the IO theory template assuming an NO "observed" data template. The NMO signal can be seen mainly at low energies for neutrinos traversing the Earth's core.

expected event difference and LLH values, respectively, obtained post-optimization for a fit of the IO theory template assuming an NO "observed" data template at the nominal expectation values and $\theta_{23} = 45^\circ$. In the figures, a larger difference and LLH denote a stronger NMO signal. As expected, it can be observed that the signal mainly comes from low-energy events traversing the core of the Earth. Further checks on the optimizer are discussed in Chapter 5 as part of the *pre-blind fits*.

4.6 Parameter Impact

To gauge the impact of the analysis parameters, two separate tests are performed—the Systematic Impact Test and the Barr Parameter Correlations Test. Based on the outcome of these tests, any parameter with low impact on the analysis is fixed in order to decrease the computational time of the fit. Due to the complexity and computational cost of calculating a rigorous NMO sensitivity (discussed in more detail in Chapter 6), the standard $\sqrt{\Delta\chi^2}$ (or $\sqrt{2|\Delta\text{LLH}|}$) Wilks' calculation [68] is used to estimate the analysis sensitivity mismodeling in both of these tests. This approach is found to yield similar values.

4.6.1 Systematic Impact Test

The Systematic Impact Test quantifies the mismodeling introduced in the analysis sensitivity due to fixing a given parameter at its nominal expectation value when the truth value is different. The larger the mismodeling produced, the greater the parameter impact on the analysis. The "truth" values assessed are the $\pm 1\sigma$ values away from nominal in the case of an existing Gaussian prior, or for parameters without a prior constraint, the halfway point between the nominal value and the upper or lower bound is evaluated. Figure 4.14 shows a diagram of the steps taken to quantify the mismodeling for the example case of the DOM efficiency parameter assuming true NO. The following procedure is performed:

1. Generate NO and IO theory templates with the test parameter fixed at its nominal expectation value.
2. Conduct a *reference fit* to the "observed" data template assumed at nominal.
3. Conduct a *test fit* to the "observed" data template with the test parameter pulled to $\pm 1\sigma$ of its value (otherwise at nominal).

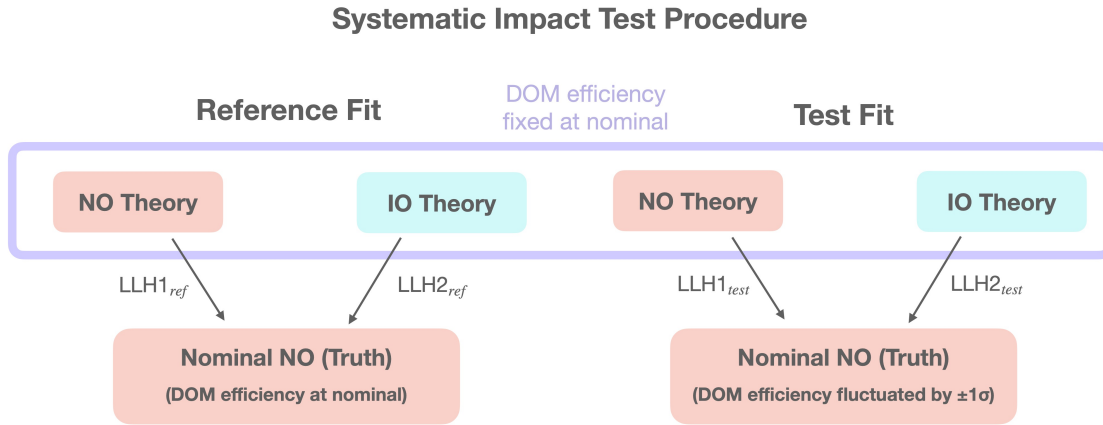


Figure 4.14: Diagram of the systematic impact test for the example case of the DOM efficiency parameter assuming true NO.

4. Calculate a *reference* and *test* sensitivity using

$$\eta_{\sigma} \approx \sqrt{2|\Delta\text{LLH}|} \quad (4.7)$$

5. Calculate the sensitivity mismodeling as

$$\text{Mismodeling} = \left| \eta_{\sigma_{ref}} - \eta_{\sigma_{test}} \right| \quad (4.8)$$

To gauge the stability of the reference fit, the reference sensitivity is plotted across all test parameters as shown in Figure 4.15 for true NO (top) and true IO (bottom). As can be seen, the reference sensitivity is mostly independent of the test parameter indicating that fixing any given parameter at its nominal truth value has a negligible effect. Thus, the Systematic Impact Test shows the *relative impact with respect to the test fit*.

Figures 4.16 and 4.17 show the results of this test for both true NO and true IO, respectively. Parameters either boxed or signaled are found to have a mismodeling greater than 0.1σ (red line) leading to a non-negligible impact on the analysis. Therefore, these parameters are kept free in the fit. One exception is the muon normalization parameter,

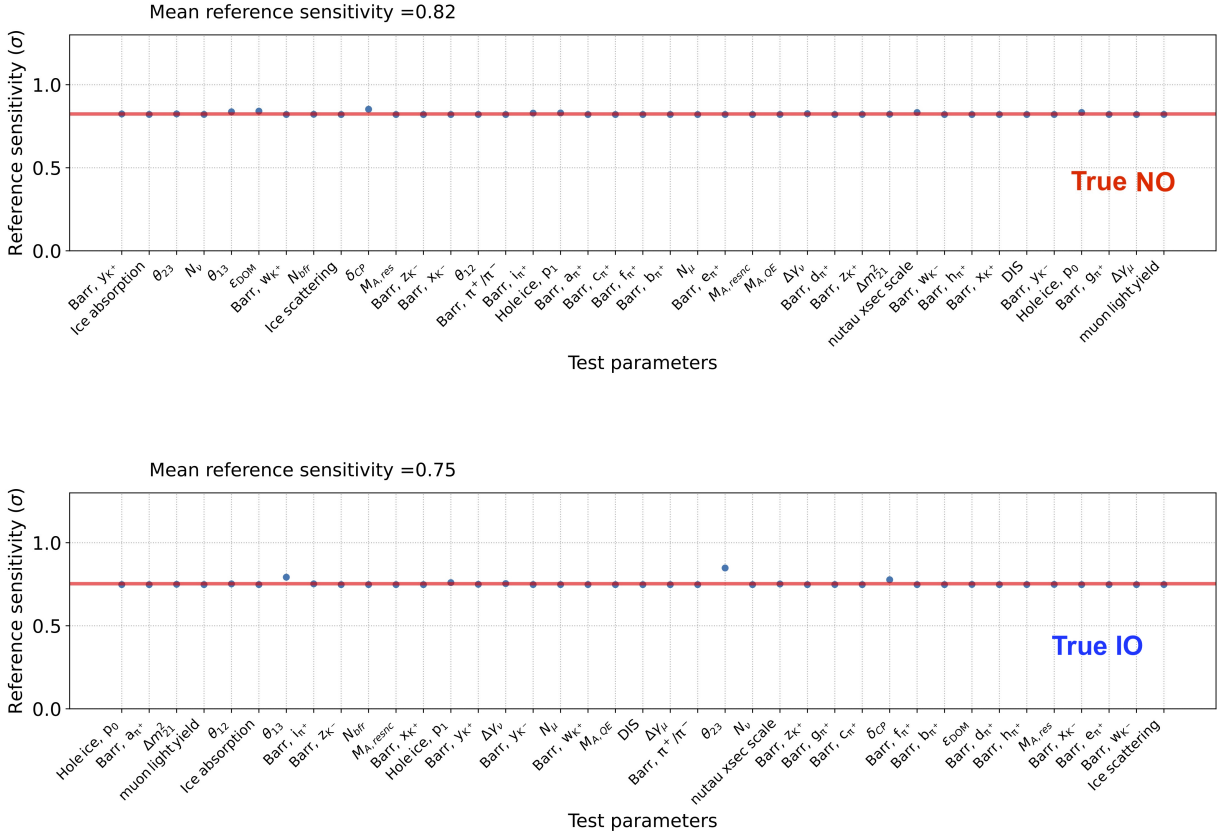


Figure 4.15: Reference sensitivity assuming true NO (top) and true IO (bottom) for all analysis parameters tested. The sensitivity is similar when fixing any given parameter at its nominal true value.

which is kept free regardless of having a lower mismodeling than the chosen threshold to improve the data-MC agreement. For the δ_{CP} , Muon Light Yield, and BFR parameters, it is not possible to test the negative pulls as the nominal value for these is located on the lower bound of the range. It is important to note that this test cannot be performed for the mass splitting parameter, Δm_{31}^2 , as fixing the value of this parameter introduces a spurious contribution to the fit. This occurs as a result of using the same fixed value of $|\Delta m_{31}^2|$ in both the NO and IO theory templates, leading to different values of $|\Delta m_{32}^2|$ in each. This artificially enhances the sensitivity.

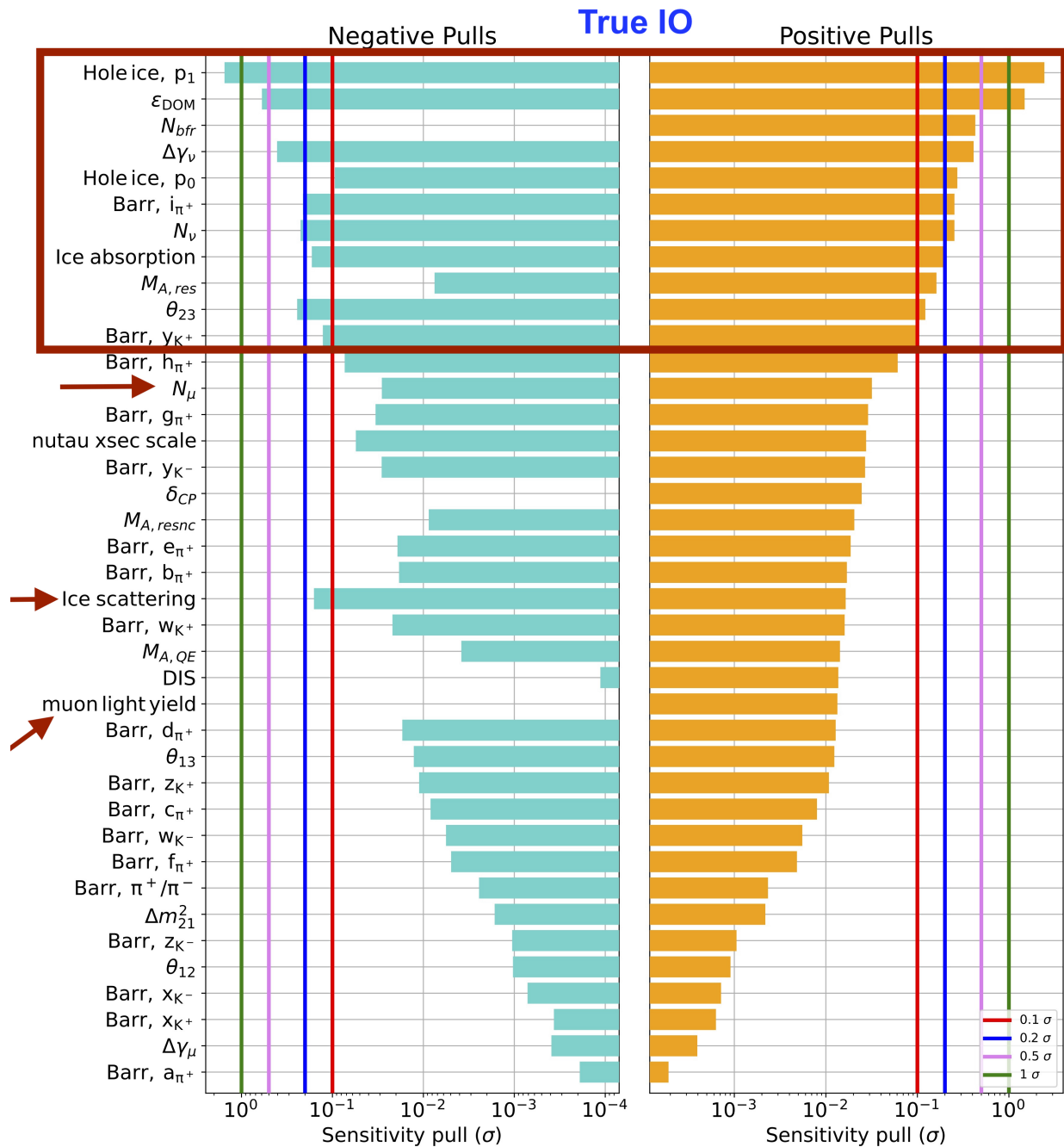


Figure 4.17: Systematic Impact Test results assuming true IO for $\pm 1\sigma$ pulls. Boxed or signaled parameters are kept free in the analysis except for the Barr parameters, which are further gauged using the Barr Parameter Correlations Test.

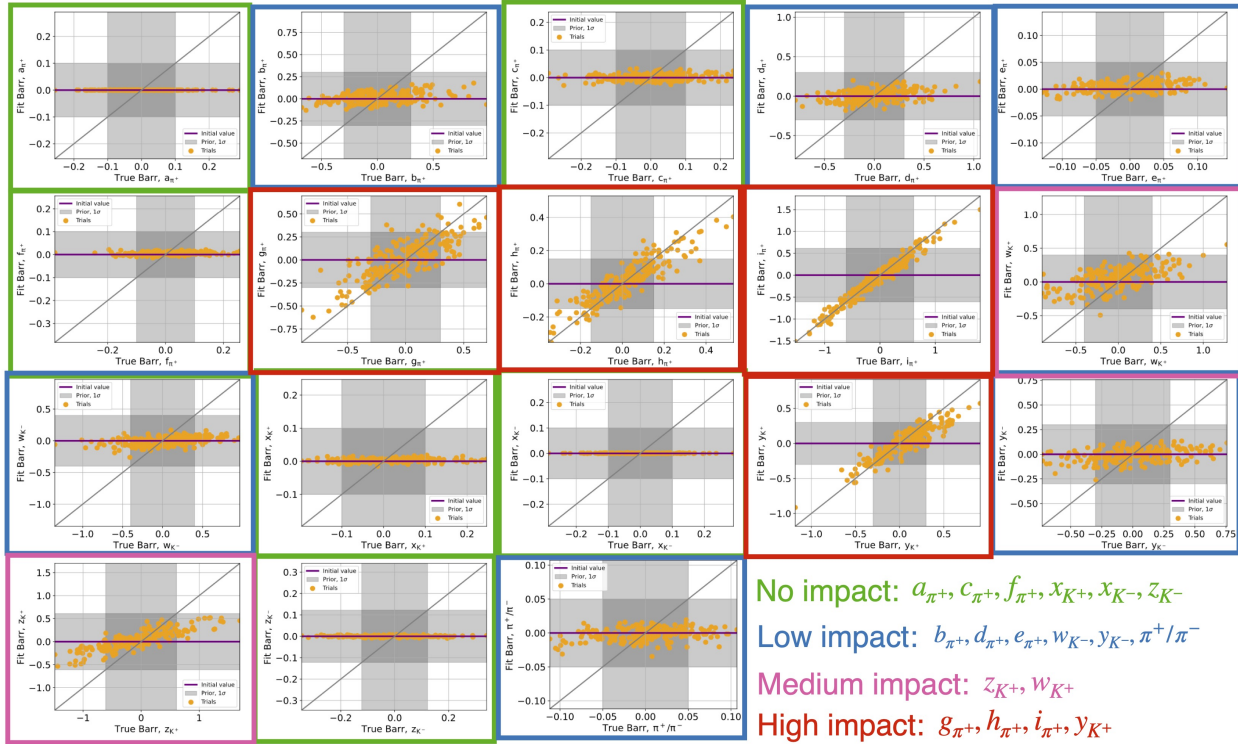


Figure 4.18: Barr Parameter Ensemble Test results for a fit of the IO theory assuming an NO "observed" data template for 200 trials. The test classifies each Barr parameter as having either no impact, low impact, medium impact, or high impact.

4.6.2 Barr Parameter Correlations Test

As correlation effects are more prominent between the various Barr parameters, a Barr Parameter Correlations Test is performed to further assess the impact of these on the analysis. This test is broken up into two parts— a *classification* of the relative impact of each Barr parameter and a *quantification* of this impact on the sensitivity mismodeling of the analysis.

The first part is achieved using the *Parameter Ensemble Test* for the Barr parameters only. Mainly, this test consists in simultaneously fluctuating all Barr parameter values in the "observed" data template and performing a fit. The fitted value of each Barr parameter is then plotted as a function of its fluctuated "true" value. This procedure is repeated for a total of 200 trials to gauge the overall behavior and impact of the given parameter. The results of the Barr Parameter Ensemble Test are shown in Figure 4.18 for a fit of the IO

theory template assuming an NO "observed" data template. All four fits pertaining to the NMO analysis (two for each mass ordering) are evaluated and are found to yield similar results.

Based on the trend observed in the Barr Parameter Ensemble Test, Barr parameters are classified into one of four impact categories— no impact, low impact, medium impact, or high impact. A parameter with no impact on the analysis follows a horizontal trend as this shows that the fitted value did not change from the starting value. Therefore, the fit did not need to compensate for having fluctuated the true value, and as a result, the true value of this parameter is not important for the fit. On the contrary, parameters with high impact on the analysis lie on the diagonal, showing that the true value of this parameter is important for the fit. Furthermore, parameters with medium impact follow a semi-raised trend, where the fitted values of the parameter are only slightly shifted towards the diagonal.

One feature worth noting consists in a *pull* exerted on the fitted value from the Gaussian prior as a result of fluctuating the true parameter value. Since the prior is centered around the nominal value, as the fit starts to drift towards the fluctuated true value, a tension is created by the prior, pulling the fit in the opposite direction. Hence, a high impact parameter is one who is able to completely overcome this pull.

The second part of the Barr Parameter Correlations Test consists in quantifying the analysis sensitivity mismodeling produced by fixing the various categories of parameter impact. Figure 4.19 shows a diagram of the steps performed to quantify this sensitivity mismodeling assuming true NO. The procedure is as follows:

1. Generate NO and IO theory templates with both the non-Barr parameters and the *test* Barr parameters fixed at their nominal expectation value. The Δm_{31}^2 oscillation parameter, however, is kept free due to the spurious contribution created when fixed (refer back to Section 4.6.1).
2. Conduct a *reference fit* to the "observed" data template assumed to be at nominal.

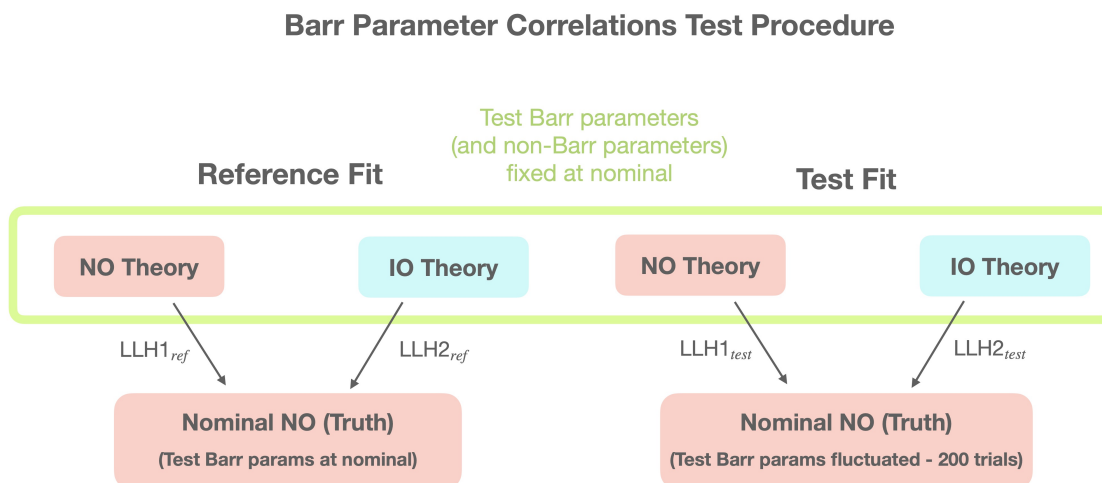


Figure 4.19: Diagram of the Barr Parameter Correlations Test assuming true NO.

3. Conduct a *test fit* to the "observed" data template with fluctuated test Barr parameter values.
4. Calculate *reference* and *test* sensitivities using Equation 4.7.
5. Calculate the sensitivity mismodeling using Equation 4.8.
6. Repeat the procedure for 200 trials.

Figure 4.20 shows the results of this test for the NMO analysis, where the cumulative distribution function (CDF) is plotted for the sensitivity mismodeling assuming an NO "observed" data template. The orange curve in the plot is the *baseline* when all Barr parameters are kept free. Baseline "mismodeling" occurs due to the prior pull being exerted on the test fit but not on the reference fit as this one is evaluated at the nominal true values. As a result, this test is evaluated as a *relative difference* between the baseline curve and a test curve.

Mismodeling test curves are plotted for different motivated choices of fixed Barr parameters in Figure 4.20. The mismodeling tolerance is set as a 5% change in the baseline

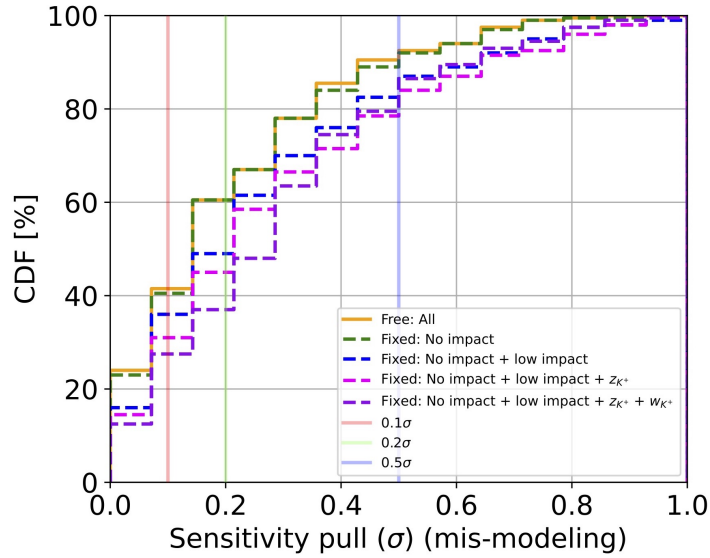


Figure 4.20: Sensitivity mismodeling accounting for correlations among the Barr parameters. The mismodeling is plotted for various categories of fixed Barr parameters assuming true NO. Based on 200 trials, the cumulative distribution function (CDF) shows the percentage of trials that generate the given mismodeling or lower.

mismodeling at the 0.1σ line. Any combination of Barr parameters with less relative mismodeling than the tolerance are considered to have a negligible impact on the analysis. Thus, parameters labeled as "no impact" or "low impact" are fixed. The same conclusion is found for an assumption of true IO.

Table 4.3 shows the list of parameters considered in this analysis along with their respective nominal values, priors, and bounds. Furthermore, the table also shows whether a parameter is fixed or freed in the fit. Parameters highlighted in yellow are kept free. Note that for all checks and studies described before Chapter 7, the bulk ice absorption and scattering parameters are assigned a Gaussian prior of $\sigma = \pm 0.05$ and $\sigma = \pm 0.1$, respectively. Due to an unresolved disagreement between bulk ice calibration data and simulation, a conservative uniform prior is adopted at the *blind-fit* stage and onwards. This modification is found to yield a negligible effect on the studies mentioned in this work.

Table 4.3: List of analysis parameters considered, along with priors and allowed bounds. Parameters highlighted in yellow are kept free. Note that for all checks and studies described before Chapter 7, the bulk ice absorption and scattering parameters are assigned a Gaussian prior of $\sigma = \pm 0.05$ and $\sigma = \pm 0.1$, respectively. Due to an unresolved disagreement between bulk ice calibration data and simulation, a conservative uniform prior is adopted at the *blind-fit* stage and onwards.

| Parameter | Nominal Value | Prior | Bounds | Fixed? |
|--------------------------------|---|-------------------------------|----------------------|-------------|
| Flux: | | | | |
| $\Delta\gamma_\nu$ | 0 | Gaussian, $\sigma = \pm 0.1$ | [-0.5, 0.5] | Free |
| Energy Pivot | 24.09 | - | - | Fixed |
| Barr π^+/π^- | 0 | - | - | Fixed |
| Barr a_ π^+ | 0 | - | - | Fixed |
| Barr b_ π^+ | 0 | - | - | Fixed |
| Barr c_ π^+ | 0 | - | - | Fixed |
| Barr d_ π^+ | 0 | - | - | Fixed |
| Barr e_ π^+ | 0 | - | - | Fixed |
| Barr f_ π^+ | 0 | - | - | Fixed |
| Barr g_ π^+ | 0 | Gaussian, $\sigma = \pm 0.3$ | [-1.5, 1.5] | Free |
| Barr h_ π^+ | 0 | Gaussian, $\sigma = \pm 0.15$ | [-0.75, 0.75] | Free |
| Barr i_ π^+ | 0 | Gaussian, $\sigma = \pm 0.61$ | [-3.05, 3.05] | Free |
| Barr w_ K^+ | 0 | Gaussian, $\sigma = \pm 0.4$ | [-2.0, 2.0] | Free |
| Barr x_ K^+ | 0 | - | - | Fixed |
| Barr y_ K^+ | 0 | Gaussian, $\sigma = \pm 0.3$ | [-1.5, 1.5] | Free |
| Barr z_ K^+ | 0 | Gaussian, $\sigma = \pm 0.61$ | [-3.05, 3.05] | Free |
| Barr w_ K^- | 0 | - | - | Fixed |
| Barr x_ K^- | 0 | - | - | Fixed |
| Barr y_ K^- | 0 | - | - | Fixed |
| Barr z_ K^- | 0 | - | - | Fixed |
| Neutrino Normalization: | | | | |
| N_ν | 1.0 | Uniform | [0.1, 2.0] | Free |
| Cross Section: | | | | |
| $M_{A,QE}, CC$ | 0 | - | - | Fixed |
| $M_{A,RES}, CC$ | 0 | Gaussian, $\sigma = \pm 1.0$ | [-2.0, 2.0] | Free |
| $M_{A,RES}, NC$ | 0 | - | - | Fixed |
| DIS | 0 | - | - | Fixed |
| ν_τ cross-section scale | 0 | - | - | Fixed |
| Detector: | | | | |
| DOM Efficiency | 1.0 | Gaussian, $\sigma = \pm 0.1$ | [0.8, 1.2] | Free |
| Hole Ice p_0 | 0.102 | Uniform | [-0.6, 0.5] | Free |
| Hole Ice p_1 | -0.0493 | Uniform | [-0.2, 0.2] | Free |
| Bulk Ice Absorption | 1.0 | Uniform | [0.9, 1.1] | Free |
| Bulk Ice Scattering | 1.05 | Uniform | [0.85, 1.25] | Free |
| Birefringence | 0 | Uniform | [0, 1.0] | Free |
| Muon Light Yield | 0 | Uniform | [0, 1.0] | Free |
| Oscillations: | | | | |
| Earth Model | PREM 12 layers | - | - | Fixed |
| Y_e Inner Core | 0.4656 | - | - | Fixed |
| Y_e Mantle | 0.4957 | - | - | Fixed |
| Y_e Outer Core | 0.4656 | - | - | Fixed |
| Detector Depth [km] | 2.0 | - | - | Fixed |
| Prop Height [km] | 20.0 | - | - | Fixed |
| θ_{12} | 33.82° | - | - | Fixed |
| θ_{13} | 8.61° | - | - | Fixed |
| θ_{23} | 47.5047° | Uniform | [38°, 52°] | Free |
| δ_{CP} | 0 | - | - | Fixed |
| Δm_{21}^2 | $7.39 \times 10^{-5} \text{ eV}^2$ | - | - | Fixed |
| Δm_{31}^2 | $\pm 2.47467 \times 10^{-3} \text{ eV}^2$ | Uniform | $\pm [0.001, 0.004]$ | Free |
| Atmospheric Muons: | | | | |
| $\Delta\gamma_\mu$ | 0 | - | - | Fixed |
| N_μ | 1.0 | Gaussian, $\sigma = \pm 0.4$ | [0.1, 3.0] | Free |

Chapter 5

Gauging the Analysis Response

A series of checks are performed on the true NO and true IO MC simulation templates to gauge the response and behavior of the analysis prior to conducting any fits on the real data template. These checks consist of the Inject-Recover Test, the Parameter Ensemble Test, and the Ensemble Test. The first two tests consist in fluctuating the *parameter values* while the last test statistically fluctuates the template *bin counts*.

5.1 Inject-Recover Test

The Inject-Recover Test focuses on gauging the robustness of the optimizer described in Section 4.5 through its ability to recover the fluctuated oscillation parameter values for fits of the analysis templates. Note that only the true values of θ_{23} and Δm_{31}^2 are fluctuated in this test as these are the only two oscillation parameters that are kept free in the analysis. Given that there are no Gaussian priors imposed on these two parameters, a suitable optimizer is expected to recover all of the true values when fitting a theory of the same mass ordering as the assumed data. This is seen in Figure 5.1 for assumptions of true NO (left) and true IO (right).

Moreover, the same test is performed for a fit of a theory with the *opposite* mass ordering as the assumed data. As a result of the discrete nature of the two mass orderings, the

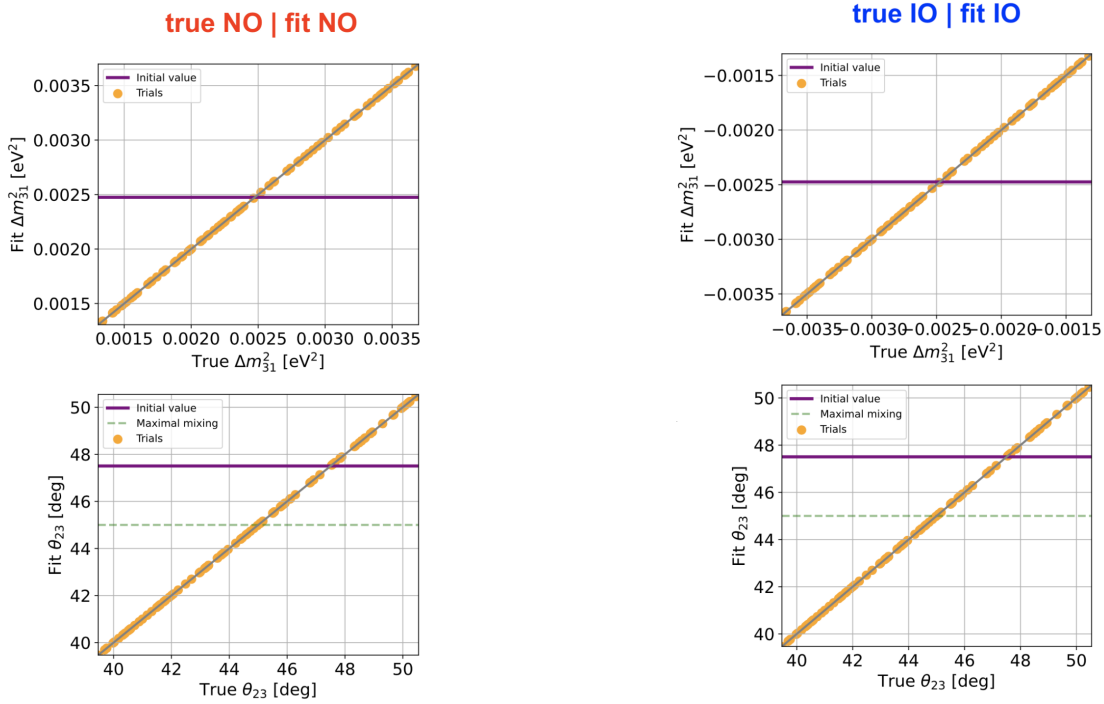


Figure 5.1: True values of θ_{23} and Δm_{31}^2 are fluctuated as part of the Inject-Recover Test, which gauges the optimizer's ability to recover each value.

optimizer is not necessarily expected to recover the true parameter values. Instead, an interesting pattern emerges for the θ_{23} parameter as shown in Figure 5.2, where the best fit θ_{23} value lies in the opposite octant for certain ranges of the parameter space. This characteristic pattern is due to a mass-ordering-octant degeneracy [2; 30], which is discussed in more detail in Section 6.2.

5.2 Parameter Ensemble Test

Similarly to the Inject-Recover Test, the Parameter Ensemble Test gauges the behavior of the best fit of a given parameter value with respect to its true value. However, in this test, *all* of the analysis parameters are fluctuated simultaneously as opposed to the oscillation parameters only. Thus, it is then possible to assess the overall analysis response (excluding any effects arising from statistical fluctuations).

In contrast to the Inject-Recover Test, a perfect recovery of the true values is not

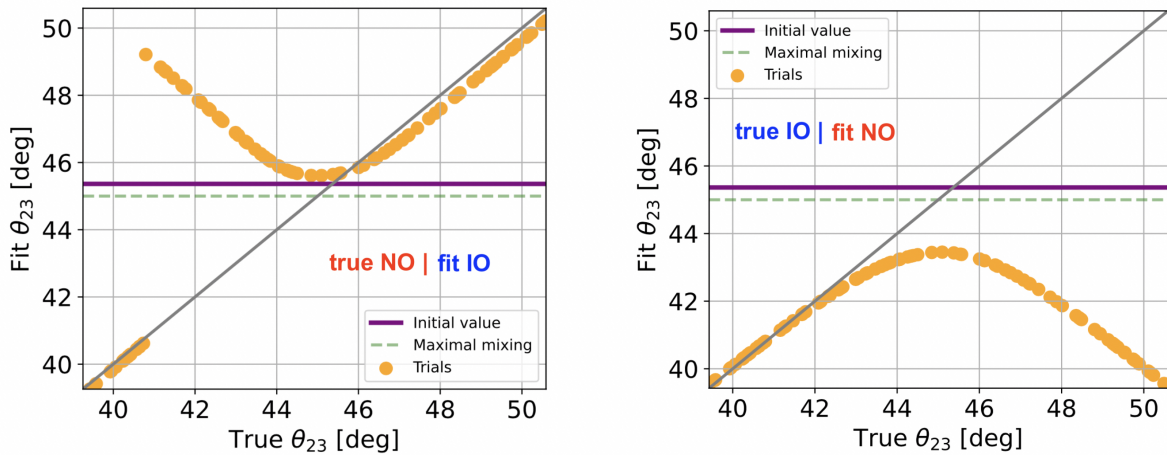


Figure 5.2: A characteristic pattern emerges for a fit of a theory with the opposite mass ordering as the assumed data for specific ranges in the θ_{23} parameter space. This occurs due to the mass-ordering-octant degeneracy [2; 30].

necessarily expected even for the case of fitting a theory with the same mass ordering as the assumed data. This is a result of correlations that exist between parameters as well as effects from the Gaussian priors imposed on some of the parameters. Figure 5.3 shows the results of this test for a fit of the NO theory template assuming an NO "observed" data template. All in all, a good recovery of the true values is observed for most parameters. A similar response is found in the case of fitting the IO theory assuming an IO data template.

For the case of fitting a theory with the opposite mass ordering as the assumed data, similar behavior is observed for all analysis parameters except for the two oscillation parameters as shown in Figure 5.4. As expected, the θ_{23} parameter shows the same characteristic pattern found in Figure 5.2 while Δm_{31}^2 produces a best fit in the off-diagonal due to the restriction in the parameter range imposed from fitting a theory of the opposite mass ordering.

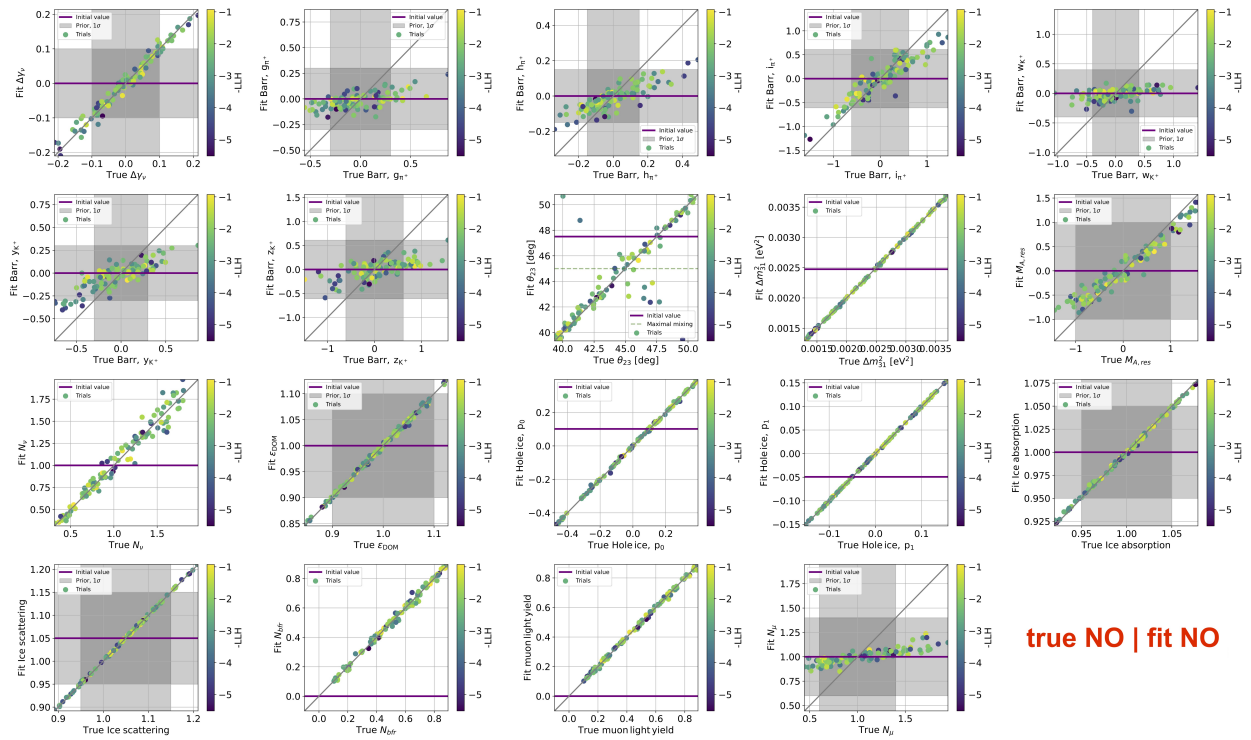


Figure 5.3: Parameter Ensemble Test for a fit of the NO theory value template assuming an NO "observed" data template. Good recovery is observed for most parameters, although not necessarily expected due to effects from correlations and Gaussian priors.

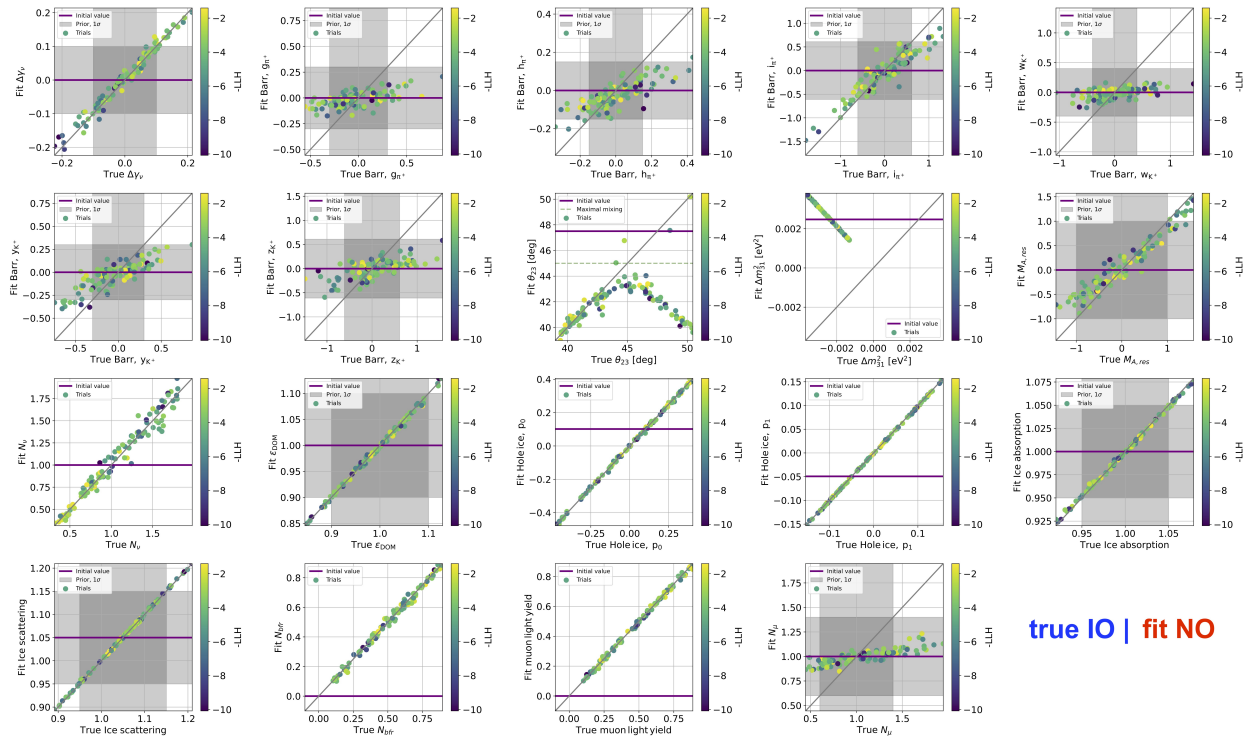


Figure 5.4: Parameter Ensemble Test for a fit of the NO theory template assuming an IO "observed" data template. The θ_{23} parameter shows the same characteristic pattern found in Figure 5.2.

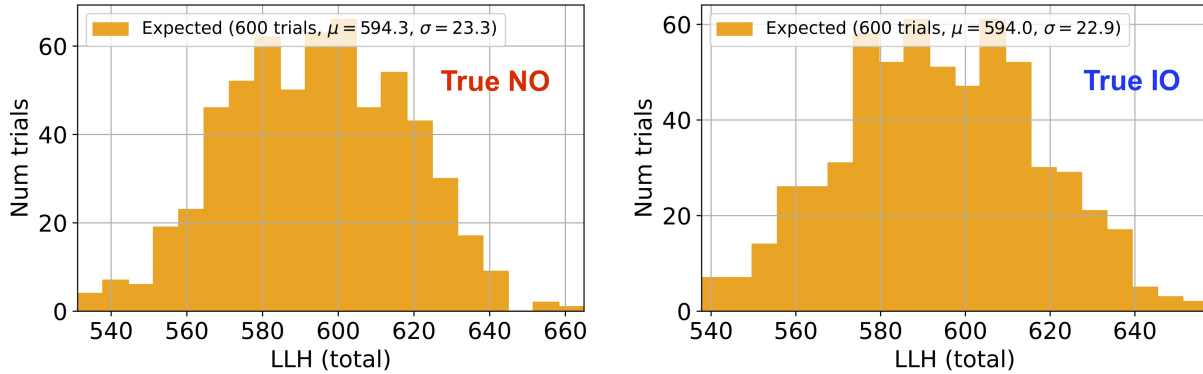


Figure 5.5: Expected distributions of the goodness of fit for true NO (left) and true IO (right) for a fit of the same mass ordering as the assumed data.

5.3 Ensemble Test

This test gauges the analysis behavior when incorporating statistical uncertainty from the limited detector livetime. Fluctuations of the nominal bin counts are performed on the assumed data template for 600 trials using a Poisson distribution. Figure 5.5 shows the expected distributions of the goodness of fit for true NO and true IO for a fit of the same mass ordering as the assumed data. The distributions are observed to follow the expected χ^2 relation of $\overline{\chi^2} \approx \text{DOF}$, where $\text{DOF} = N_{\text{bins}} - N_{\text{free params}}$ and $\chi^2 = 2|\text{LLH}|$ (Wilk's Theorem [68]).

Additionally, parameter pulls between the nominal and best fit values are assessed for all parameters with Gaussian priors. These are seen in Figure 5.6, where the median pull is shown along with the 1σ bands for 600 trials. Stable pulls are observed for both mass orderings with all medians lying close to zero and no bands surpassing a pull of 0.5σ in either direction.

Figures 5.7 and 5.8 show the expected best fit distributions for each parameter in the analysis for true NO and true IO, respectively. In general, each median value is observed to lie close to its nominal value. For the θ_{23} oscillation parameter, however, the median value is pulled towards the center, mainly, by a mirrored peak of the trials in the opposite

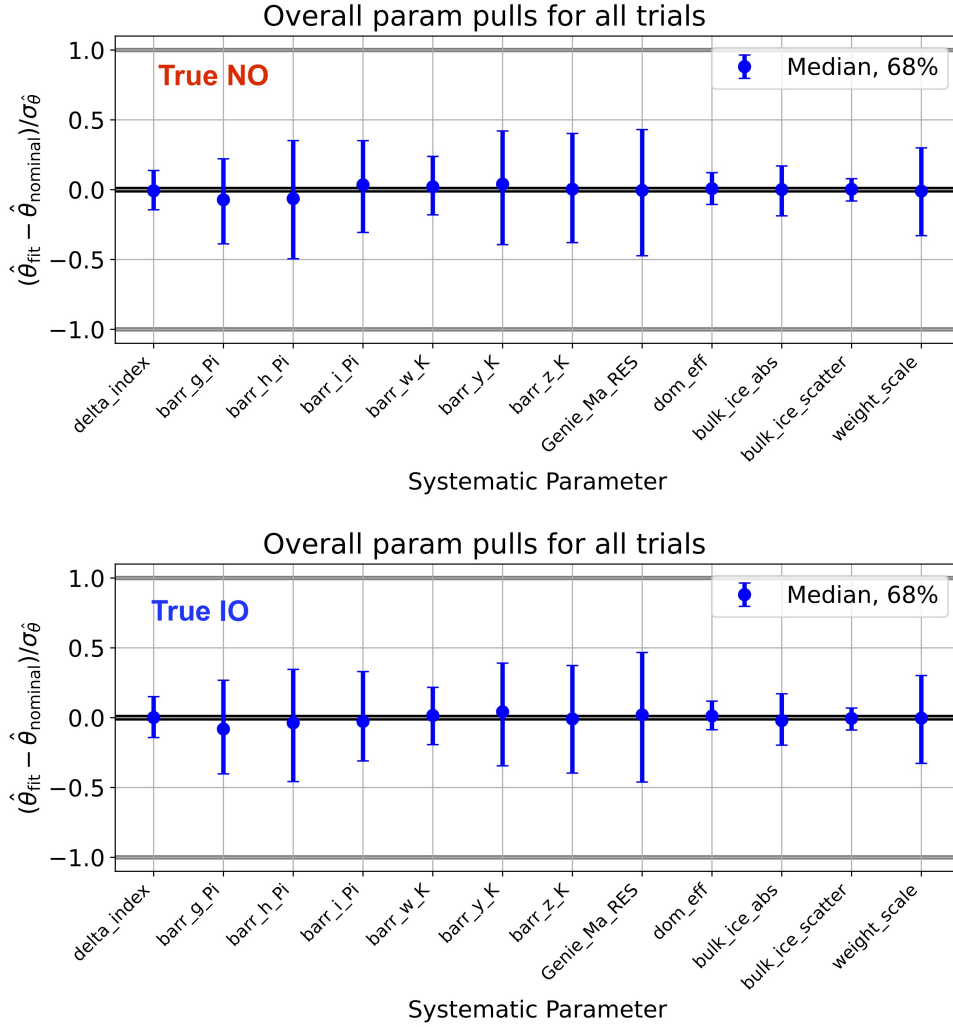


Figure 5.6: Parameter pulls between the nominal and best fit values for all parameters with Gaussian priors for true NO (top) and true IO (bottom). Stable pulls are observed with all medians lying close to zero and the 1σ bands lying below a pull of 0.5σ .

octant. This effect occurs due to the octant degeneracy discussed in Section 4.5. For some of the fluctuated trials, the bin counts are far away enough from nominal that the opposite octant of θ_{23} is a better fit.

Pearson correlation maps are shown for both mass orderings in Figure 5.9. Although these are found to be similar between the two orderings, parameter correlations with Δm_{31}^2 are observed to move in opposite directions. This is expected as the mass ordering is defined by the sign of Δm_{31}^2 . Furthermore, strong correlations are seen among the Barr parameters as well as detector parameters and $\{\Delta m_{31}^2, N_\nu, M_{A,RES} CC, \epsilon_{DOM}\}$.

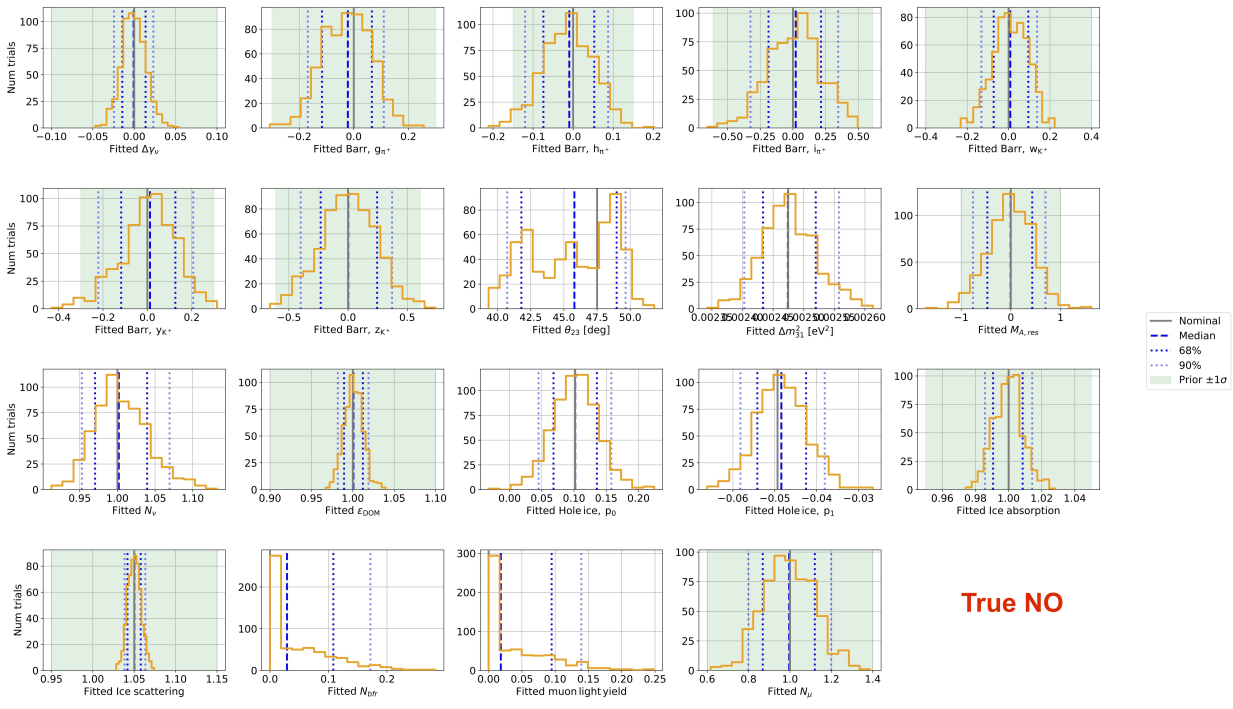


Figure 5.7: Expected best fit distributions for each parameter in the analysis for true NO. Median values are observed to lie close to their respective nominal value.

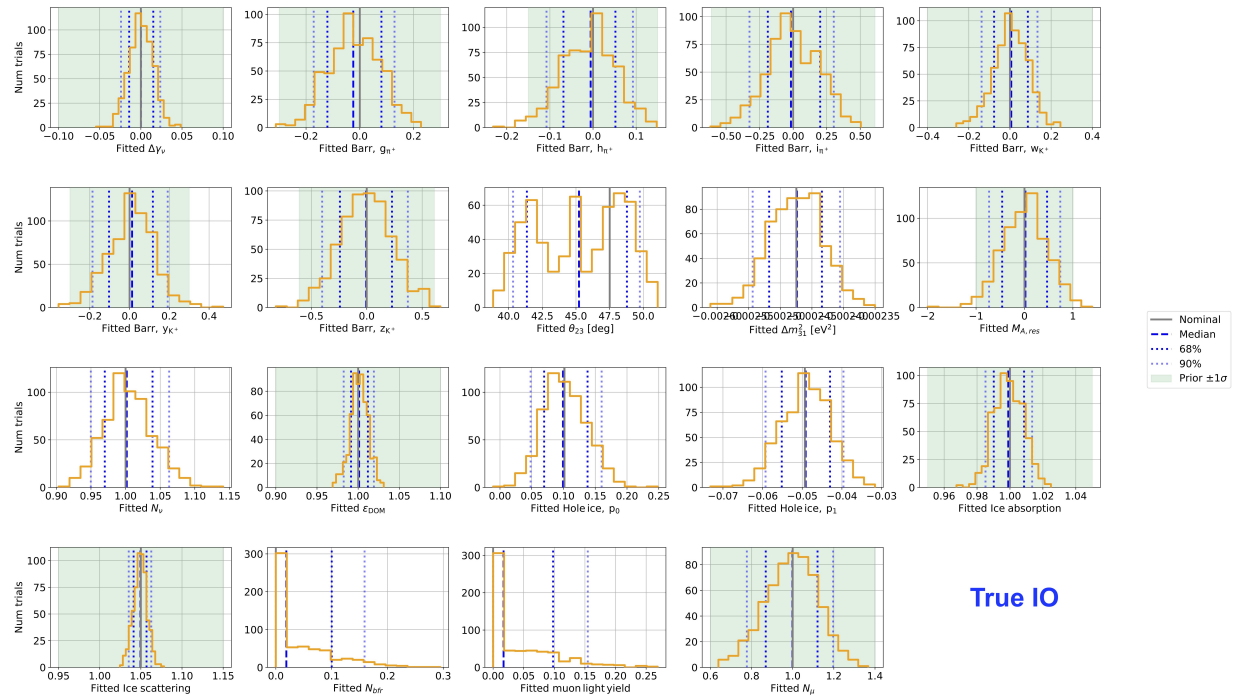


Figure 5.8: Expected best fit distributions for each parameter in the analysis for true IO. Median values are observed to lie close to their respective nominal value.

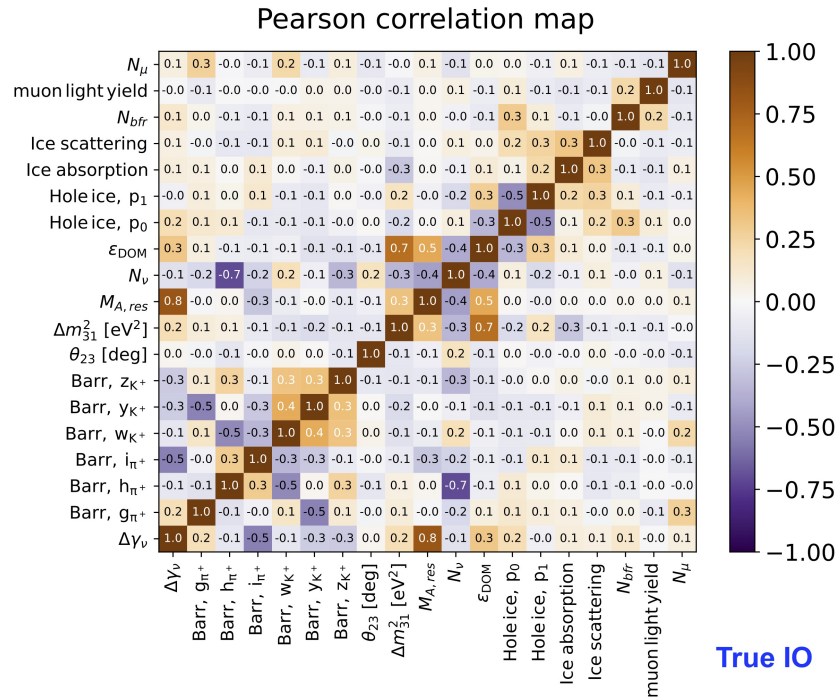
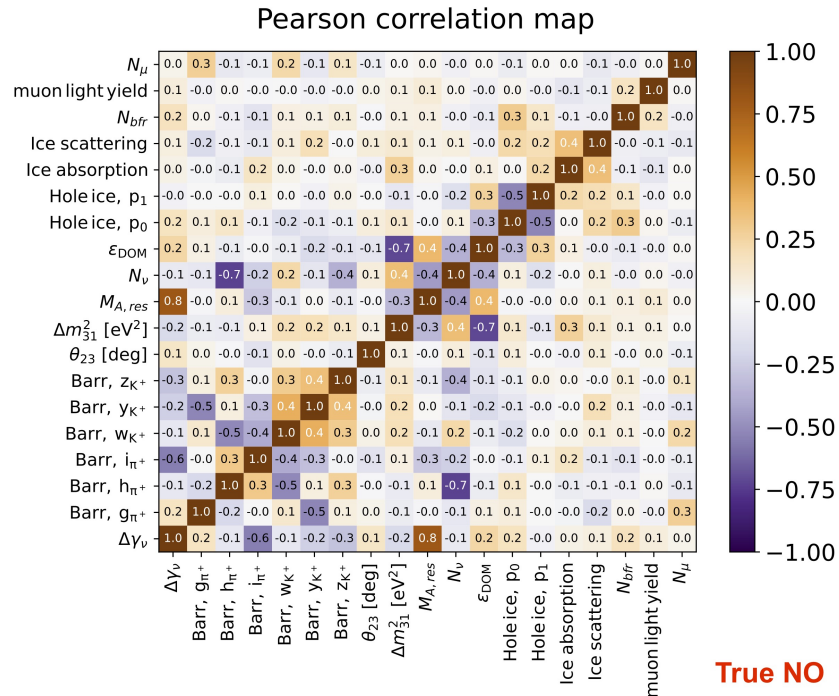


Figure 5.9: Correlations among parameters are observed to be similar for true NO (top) and true IO (bottom). Strong correlations are seen among the Barr parameters as well as detector parameters and $\{\Delta m_{31}^2, N_\nu, M_{A,RES} CC, \epsilon_{DOM}\}$.

Chapter 6

Sensitivity to the Neutrino Mass Ordering

6.1 Methodology

The following procedure, adopted from [3; 40], shows the steps taken to quantify the analysis sensitivity to the NMO. Due to the non-nested feature of the two hypotheses in question (NO and IO), the standard $\sqrt{\Delta\chi^2}$ (or $\sqrt{2|\Delta\text{LLH}|}$) Wilks' calculation [68] of the sensitivity proves to be simplistic and not entirely accurate. For non-nested hypotheses, Wilks' Theorem does not hold, meaning that, for a large sample size, the analysis test statistic does not follow a χ^2 distribution. Instead, the test statistic, mainly ΔLLH , is shown to follow a Gaussian distribution [3]. As a result, a different approach is used to quantify the sensitivity, where two separate ΔLLH distributions are constructed for each mass ordering.

Furthermore, as previously described, the sensitivity is highly dependent on the oscillation parameter, θ_{23} , due to its role in the oscillation probabilities. Although this is discussed in more detail in Section 6.2, it is important to mention at this point that, due to this dependence, the NMO sensitivity is quantified as a function of θ_{23} .

NMO sensitivity quantification procedure:

1. Assume a true ordering.
2. Label the MC simulation template generated at the nominal expectation of the true ordering as the *truth data template*.
3. Inject a chosen "true" θ_{23} value to the truth data template.
4. Statistically fluctuate the truth data template 1000 times to generate 1000 fluctuated trials.
5. Generate an NO and an IO *theory template* at the nominal expectation of each ordering.
6. Using an appropriate metric, fit both NO and IO theory templates to each fluctuated trial from Step 4.
7. Assemble a distribution of the test statistic from the difference between the NO and IO best fits. Label this as the *true ordering* distribution.
8. Generate a separate MC simulation template using the best-fit parameters from fitting the wrong-ordering theory to the *unfluctuated* truth data template. Label this as the *wrong-ordering best fit template*.
9. Repeat Steps 4-7 swapping the truth data template for the wrong-ordering best fit template. This should create a second distribution of the test statistic from the difference between the NO and IO best fits. Label this as the *wrong-ordering best fit* distribution.
10. Compute a one-tailed p-value using the *median* of the true ordering distribution with respect to the wrong-ordering best fit distribution. In this calculation, the median of the true ordering distribution is treated as the expectation of the observed value.

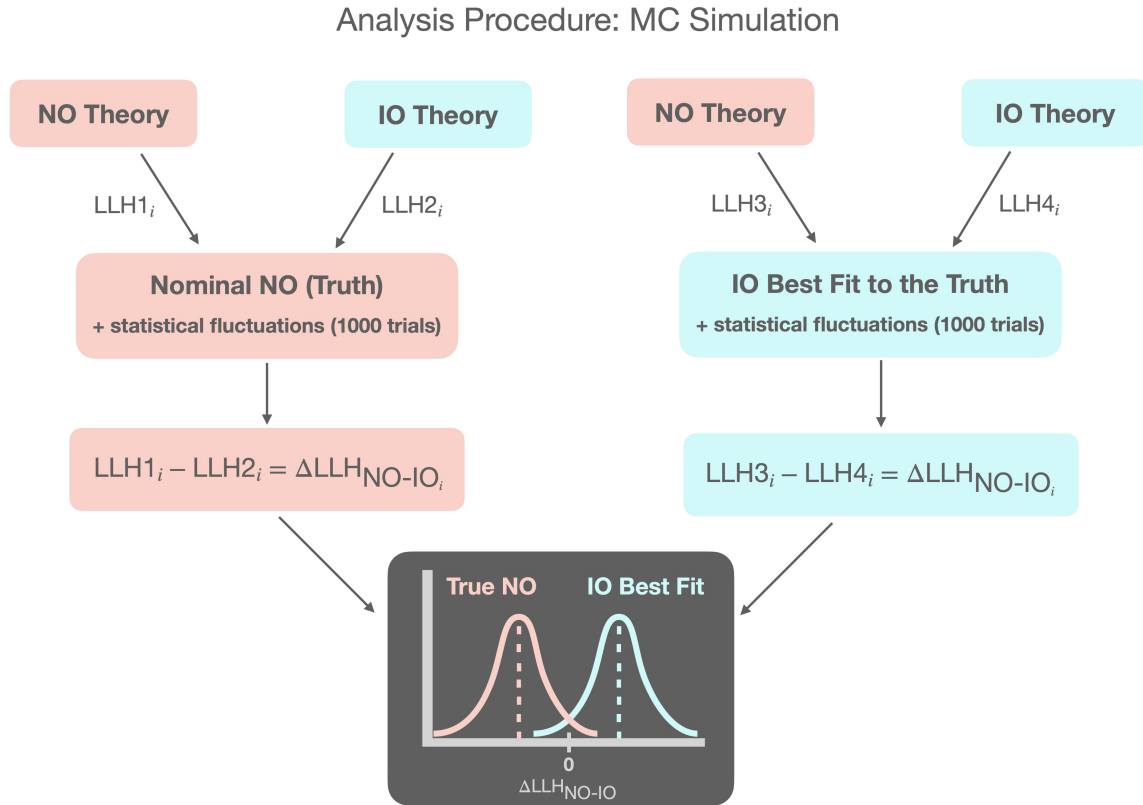


Figure 6.1: Diagram of the NMO sensitivity calculation using ΔLLH as the test statistic and assuming NO as the true ordering. When fitting to the real data, a similar but slightly different approach is used as shown in Figure 8.1.

11. Compute the NMO median sensitivity using

$$\eta_{\sigma} = \sqrt{2} \text{erfc}^{-1}(2p_{\text{one-tailed}}) \quad (6.1)$$

where $p_{\text{one-tailed}}$ is the one-tailed p-value.

12. Repeat Steps 1-11 assuming the opposite ordering as the true ordering.

Figure 6.1 shows a diagram of the NMO sensitivity calculation procedure using the analysis test statistic, ΔLLH , and assuming NO as the true ordering. This creates the two $\Delta\text{LLH}_{\text{NO-IO}}$ distributions from Steps 7 and 9, where $\Delta\text{LLH}_{\text{NO-IO}_i} = |\text{LLH}_{\text{NO}_i}| - |\text{LLH}_{\text{IO}_i}|$ and $i \in \{1, 2, 3, \dots, 1000\}$. As a result of the convention used for the test statistic—mainly,

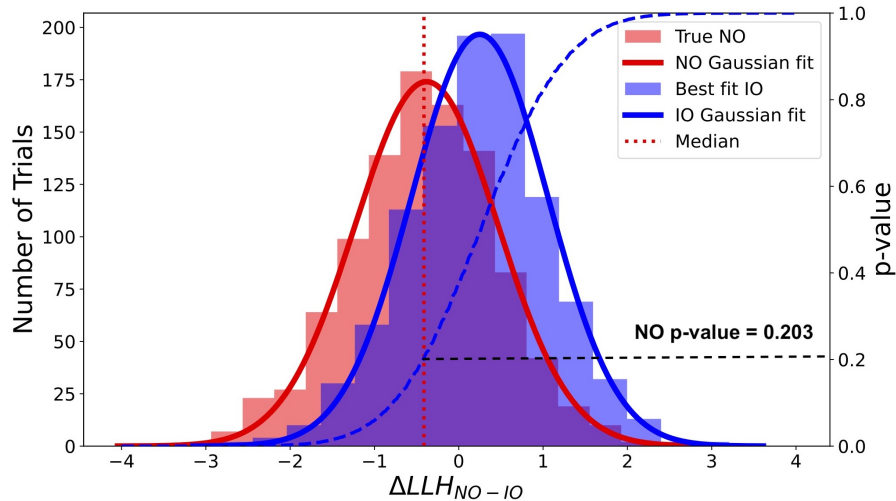


Figure 6.2: Example of the p-value calculation in the case where the observed value is at the median of the true ordering distribution (red). The p-value is then used to quantify the *median sensitivity*.

that $\Delta LLH = \Delta LLH_{NO-IO}$ and not ΔLLH_{IO-NO} —values of $\Delta LLH_{NO-IO} < 0$ indicate a preference for NO while values of $\Delta LLH_{NO-IO} > 0$ indicate a preference for IO. Thus, an assumed NO (IO) distribution will be shifted to the left (right) of zero as seen in the diagram.

The median sensitivity represents DeepCore’s expected ability to rule out each of the two mass orderings. In other words, provided an observed value at the median of the true ordering distribution, with how much confidence is DeepCore able to reject the most similar distribution of the wrong ordering? The sensitivity, of course, varies depending on the precise location of the “observed value” within the true ordering distribution. Mainly, the observed value does not necessarily need to lie at the median of the distribution, but instead, could lie to one of the sides. Depending on the side, the sensitivity can increase (decrease) as the observed value is now farther (closer) to the wrong-ordering distribution.

Figure 6.2 shows the one-tailed p-value for an assumption of true NO *with respect to the IO best fit distribution*. The p-value in this case lies to the *left* of the observed value, while for an assumed true IO, it lies to the *right*. The choice of a one-tailed test can be understood by thinking about a hypothetical scenario where DeepCore has no sensitivity to measuring

| CL = 1 - p | 25% | 50% | 68.27% | 90% | 95% | 99% |
|------------|----------------|---------------|---------------|---------------|---------------|---------------|
| one-tailed | -0.674σ | 0σ | 0.476σ | 1.282σ | 1.645σ | 2.326σ |
| two-tailed | 0.319σ | 0.674σ | 1σ | 1.645σ | 1.960σ | 2.576σ |

Table 6.1: The corresponding significance and confidence level (CL) calculated from one-tailed and two-tailed p-values. The significance is computed using Equation 6.1 for the one-tailed case. For the two-tailed case, the equation can be found in [3].

the mass ordering. Consequently, both NO and IO distributions would lie directly on top of each other, leading to a 50% p-value in both true NO and true IO cases. A 50% p-value, then, should correspond to a significance of 0σ . This is seen in Table 6.1 for a one-tailed test as opposed to a two-tailed test, where a 50% p-value yields a significance of 0.674σ . It is important to note, however, that this example as well as the choice of a one-tailed p-value assume that the observed value lies at the *median* of the true ordering distribution. For the case where the observed value lies to one of the sides of the true ordering distribution, a different approach is taken. This is discussed in more detail in Chapter 8.

6.1.1 The Pseudotrial Method

The frequentist procedure described above fluctuates the bin counts of the event distributions using Poisson statistics as a way of incorporating statistical uncertainty from the limited detector lifetime. This approach is called the *Pseudotrial Method* as it relies on the accuracy provided by performing many fluctuated trials, or *pseudotrials*.

This method, although robust, proves computationally exhaustive when performed for the full θ_{23} parameter space for which the NMO sensitivity is computed for. As a result, a substantially less computationally expensive approximation method is adopted from [3; 6; 40] to calculate the sensitivity. This method is called the *Asimov Method*.

The Asimov Method is used for modeling the behavior of the sensitivity curve and providing a close estimate of the sensitivity projection. The sensitivity is then computed using the Pseudotrial Method for four representative points throughout the θ_{23} parameter

space so as to both verify the validity of the Asimov Method and improve the accuracy of the projections at these values. It is important to note that when performing a fit to the true observed data, the more robust Pseudotrial Method is conducted.

6.1.2 The Asimov Method

At its core, the Asimov Method uses features derived from Wilks' theorem to approximate the medians of the $\Delta\text{LLH}_{\text{NO-IO}}$ distributions without the need to generate any fluctuated trials. Mainly, this method approximates the origin of the medians as the fits to the *unfluctuated* templates.

To understand the Asimov Method, one can think of the following simplified case where no nuisance parameters are involved. Let us first denote the number of expected events per bin with a vector \mathbf{y} . Label \mathbf{y}^{NO} as the NO theory template and, subsequently, \mathbf{y}^{IO} as the IO theory template. Assuming a true IO, we can denote the observed data template as

$$y_i^{\text{obs}} = y_i^{\text{IO}} + \sigma_i g_i, \quad (6.2)$$

where y_i^{obs} follows a Gaussian distribution with a mean (or median as these are equal here) of y_i^{IO} , a standard deviation of σ_i , and a Gaussian random variable, g_i . For simplicity, let us use the same σ_i for both NO and IO. It then follows that

$$\begin{aligned} \Delta\chi_{\text{NO-IO}}^2 &= \chi_{\text{NO}}^2 - \chi_{\text{IO}}^2 \\ &= \sum_i \frac{(y_i^{\text{obs}} - y_i^{\text{NO}})^2}{\sigma_i^2} - \sum_i \frac{(y_i^{\text{obs}} - y_i^{\text{IO}})^2}{\sigma_i^2} \\ &= \sum_i \frac{(y_i^{\text{IO}} + \sigma_i g_i - y_i^{\text{NO}})^2}{\sigma_i^2} - \sum_i \frac{(y_i^{\text{IO}} + \sigma_i g_i - y_i^{\text{IO}})^2}{\sigma_i^2} \\ &= \sum_i \frac{(y_i^{\text{IO}} - y_i^{\text{NO}})^2}{\sigma_i^2} + \sum_i \frac{2(y_i^{\text{IO}} - y_i^{\text{NO}})}{\sigma_i} g_i \end{aligned} \quad (6.3)$$

where the form of $\Delta\chi_{\text{NO-IO}}^2$ in the last line of Equation 6.3 obeys that of a Gaussian distri-

bution with the first term of the equation as the mean (or median) and the second term as the standard deviation multiplied by a Gaussian random variable. Therefore,

$$\begin{aligned}\overline{\Delta\chi^2} &= \sum_i \frac{(y_i^{\text{IO}} - y_i^{\text{NO}})^2}{\sigma_i^2} \\ \sigma &= \sum_i \frac{2(y_i^{\text{IO}} - y_i^{\text{NO}})}{\sigma_i}.\end{aligned}\tag{6.4}$$

From Equation 6.4, it is clear that the mean (or median), $\overline{\Delta\chi^2}$, is precisely equal to $\Delta\chi_{\text{NO-IO}}^2$ for the case of no statistical fluctuations ($y_i^{\text{obs}} = y_i^{\text{IO}}$). Furthermore, under certain conditions, the standard deviation term can be written as a function of the mean such that

$$\begin{aligned}\sigma &= \sum_i \frac{2(y_i^{\text{IO}} - y_i^{\text{NO}})}{\sigma_i} \\ &= \sqrt{\sum_i \frac{4(y_i^{\text{IO}} - y_i^{\text{NO}})^2}{\sigma_i^2}} \\ &= 2\sqrt{\overline{\Delta\chi^2}}.\end{aligned}\tag{6.5}$$

Equation 6.5 holds in the case that any or all of the following three conditions are met [3]:

- The NO and IO hypotheses are simple hypotheses (i.e. fixed parameters).
- The value of $\overline{\Delta\chi^2}$ is much greater than the number of free parameters (i.e. experiments with high sensitivity).
- The parameter hypersurfaces for NO and IO are parallel at the minimum.

Using the Wilks' relation of $\Delta\chi^2 = -2\Delta\text{LLH}$,

$$\sigma \approx 2\sqrt{-2\Delta\text{LLH}} = 2\sqrt{2|\Delta\text{LLH}|}.\tag{6.6}$$

Hence, the Asimov Method approximates $\Delta\text{LLH}_{\text{NO-IO}}$ as normally distributed with a mean (or median) generated from a fit to the unfluctuated template and a standard deviation of $2\sqrt{2|\Delta\text{LLH}|}$.

To compute the median sensitivity, a z-score is calculated such that

$$\begin{aligned}
 \eta_\sigma &= \frac{\overline{\Delta\chi^2_{\text{NO-IO}}(\text{true ordering})} - \overline{\Delta\chi^2_{\text{NO-IO}}(\text{wrong-ordering best fit})}}{\sigma_{\Delta\chi^2_{\text{NO-IO}}(\text{wrong-ordering best fit})}} \\
 &\approx \frac{2\overline{\Delta\text{LLH}}_{\text{NO-IO}}(\text{true ordering}) - 2\overline{\Delta\text{LLH}}_{\text{NO-IO}}(\text{wrong-ordering best fit})}{2\sqrt{2\overline{\Delta\text{LLH}}_{\text{NO-IO}}(\text{wrong-ordering best fit})}} \quad (6.7) \\
 &\approx \frac{\overline{\Delta\text{LLH}}_{\text{NO-IO}}(\text{true ordering}) - \overline{\Delta\text{LLH}}_{\text{NO-IO}}(\text{wrong-ordering best fit})}{\sqrt{2\overline{\Delta\text{LLH}}_{\text{NO-IO}}(\text{wrong-ordering best fit})}}
 \end{aligned}$$

where $\Delta\text{LLH}_{\text{NO-IO}} = |\Delta\text{LLH}_{\text{NO-IO}}|$.

6.2 Expected Sensitivity

Figure 6.3 shows the median sensitivity projection for a measurement of the neutrino mass ordering using 9.28 years of IceCube DeepCore data. The median sensitivity is plotted for four representative $\sin^2(\theta_{23})$ values for each ordering using the Pseudotrial Method. The behavior of the full curve is then gauged using the Asimov Method. The error bars in the pseudotrial values represent the uncertainty in the sensitivity arising from an uncertainty in the median of each $\Delta\text{LLH}_{\text{NO-IO}}$ distribution from having conducted a finite number of pseudotrial fits. This "standard error" is calculated as the standard deviation of the distribution of 10000 bootstrapped median sensitivities, which are obtained from bootstrapping both 1000-trial $\Delta\text{LLH}_{\text{NO-IO}}$ distributions 10000 times.

From the figure, it can be observed that the upper octant of θ_{23} is most favorable for resolving the ordering provided that the normal ordering is true. Conversely, the lower octant is most favorable provided that the inverted ordering is true. This feature of the sensitivity is attributed to a degeneracy in the oscillation probability occurring from the interplay of the θ_{23} octant and a discrete choice of the mass ordering [2; 30]. Mainly, the

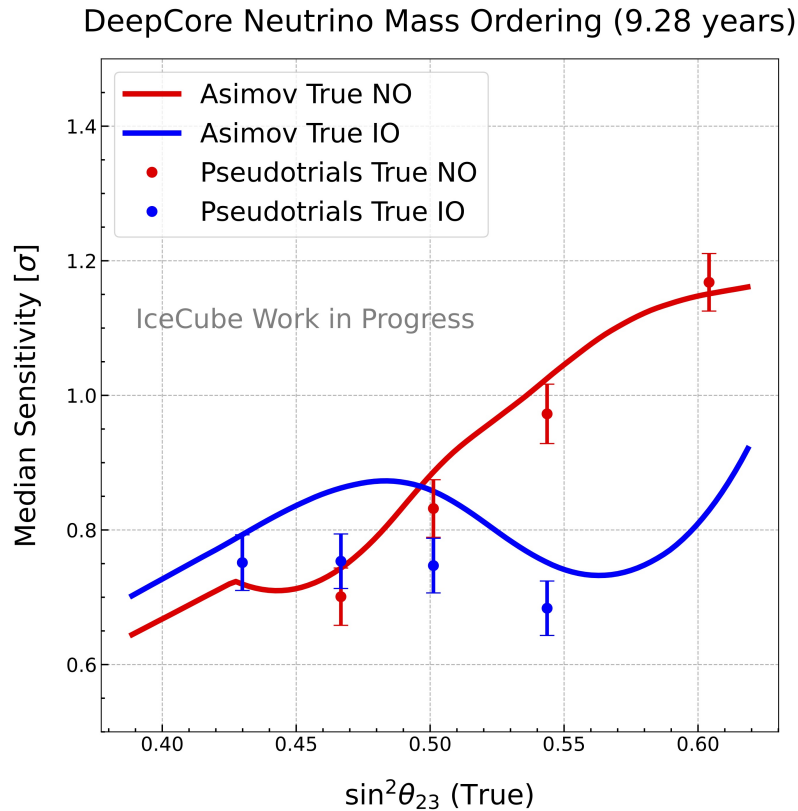


Figure 6.3: Median sensitivity projection for a measurement of the neutrino mass ordering using 9.28 years of IceCube DeepCore data. The plot shows the sensitivity for four representative $\sin^2(\theta_{23})$ values for each ordering using the Pseudotrial Method. Furthermore, the behavior of the full curve is gauged using the Asimov Method.

degeneracy flips the octant of the best fit θ_{23} as observed in Figure 5.2. This can occur if the matter effects of an experiment are too weak to break the degeneracy or, in the case of DeepCore, if high experimental uncertainties—greatly due to its inability to discriminate between neutrinos and anti-neutrinos—veil the contribution of the strong matter effects.

This effect can be better understood by looking at an example of the full three-flavor oscillation probability in the presence of matter effects for a neutrino/anti-neutrino average. This is shown in Figure 6.4 for tracks and cascades separately. The probability in the figure is plotted for two $\sin^2(\theta_{23})$ values representing the upper and lower octants for both true NO and true IO.

Let us now focus on cascade events as this is the main channel for resolving the

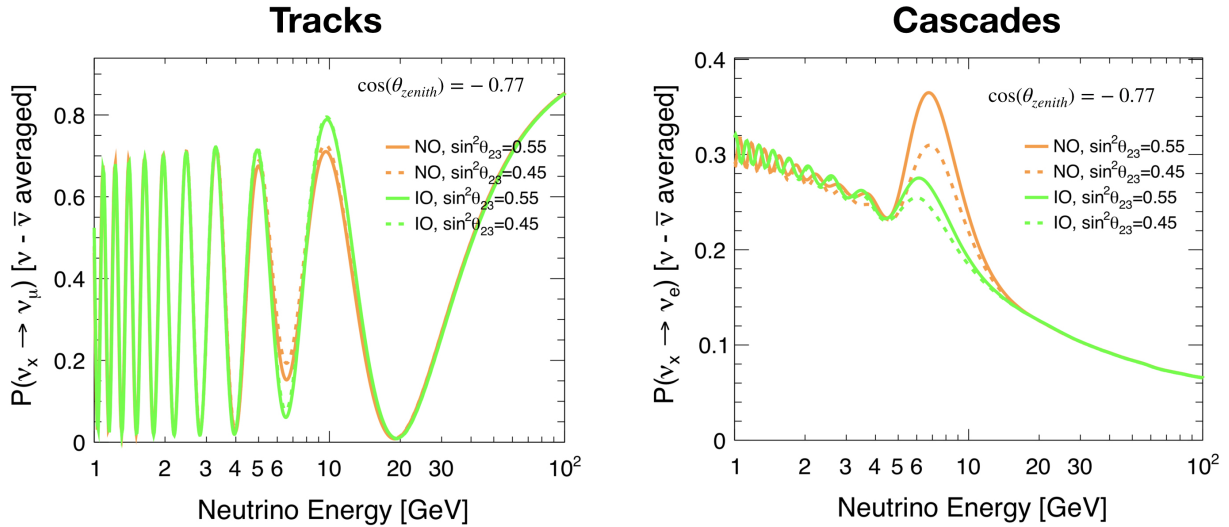


Figure 6.4: The full three-flavor oscillation probability in the presence of matter effects for a neutrino/anti-neutrino average. The probability is plotted separately for tracks and cascades for two $\sin^2(\theta_{23})$ values representing the upper and lower octants for both true NO and true IO.

degeneracy. Furthermore, let us assume the true value of $\sin^2(\theta_{23})$ to be 0.55. For the case of an NO "observed" data template (solid orange), a fit of the IO theory template will produce one of the two possible results—a best fit in the same θ_{23} octant (solid green) or a best fit in the opposite θ_{23} octant (dashed green) as seen in Figure 6.5 as choice 1 and 2, respectively. Due to the proximity of the curves, choice 1 is considered the best fit. Hence, the best fit θ_{23} value lies in the *same octant* as the true value.

Nevertheless, if this procedure is now performed assuming an IO "observed" data template (solid green), a fit of the NO theory template will yield a best fit θ_{23} value in the *opposite octant* to the true value (dashed orange). This gives rise to the difference seen in the left plot of Figure 6.6 between the true NO and true IO cases. Due to the closer fit produced in the case of a true IO, the sensitivity is lower compared to the case of a true NO, as seen in the right plot of Figure 6.6, since it is more difficult to distinguish between the two orderings. This "dip" in the true IO sensitivity is precisely created due to the favoring of the wrong octant. *The inability to resolve the θ_{23} octant due to the discrete mass ordering choice is called the mass-ordering-octant degeneracy.* For an experiment with strong matter

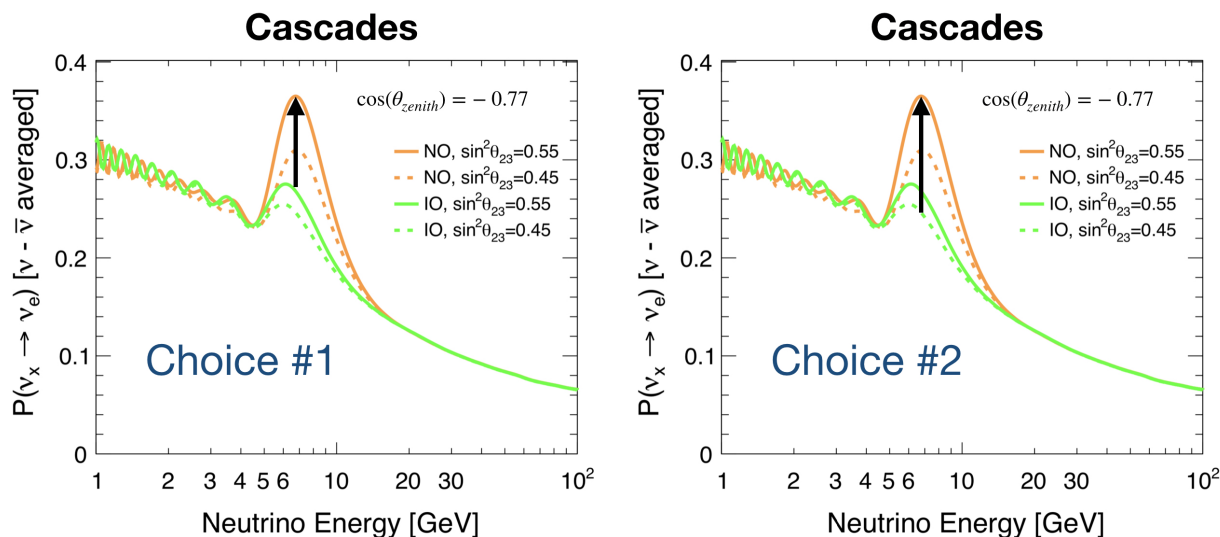


Figure 6.5: For the case of an NO "observed" data template (solid orange), a fit of the IO theory template will produce one of the two possible results, a best fit in the same θ_{23} octant (choice 1) or a best fit in the opposite θ_{23} octant (choice 2).

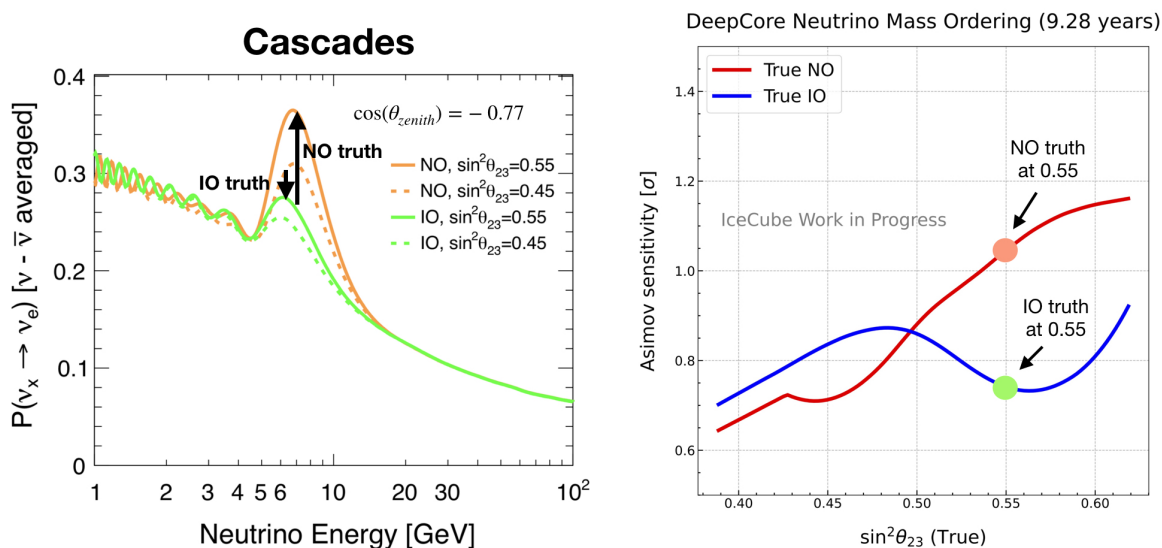


Figure 6.6: Due to the closer fit produced by the probability in the opposite octant for the case of a true IO (left plot), the sensitivity is lower compared to the case of a true NO (right plot).

effects and low uncertainties— especially in neutrino/anti-neutrino discrimination —the resulting fit would always favor the true θ_{23} octant.

Looking back at Figure 5.2, one can recognize the "dip" features in the sensitivity as the deviation in the best fit θ_{23} values from the diagonal. Hence, the kink observed in the

sensitivity for the case of a true NO is the result of a sharp resolve of the degeneracy. Without the effects caused by the mass-ordering-octant degeneracy, monotonically increasing sensitivity curves would be observed for both true NO and true IO.

6.2.1 Pseudotrial Distributions

Pseudotrial $\Delta LL_{H_{IO-NO}}$ distributions are shown in Figure 6.7 for true NO (6.7a) and true IO (6.7b) assuming atmospheric oscillation parameters at the DeepCore best fit point [42]. As expected, the distributions are well fitted by a Gaussian function. Furthermore, the median p-value is calculated from the median value of the true ordering distribution, which is then used to gauge the expected sensitivity in rejecting the wrong-ordering distribution.

6.2.2 δ_{CP} Dependence

As discussed in Section 1.8, atmospheric neutrino experiments are generally not sensitive to the δ_{CP} phase leading to δ_{CP} -independent measurements. To check this, the projected NMO median sensitivity is plotted for three representative values of δ_{CP} for the Asimov Method as shown in Figure 6.8. From the figure, only a negligible dependence on the δ_{CP} phase is observed confirming the above statement.

6.3 Comparison to the 3-Year DeepCore Sensitivity

As mentioned in Section 1.8, the goal of this work is to produce a more robust DeepCore measurement of the mass ordering in comparison to the previous 3-year measurement [40]. Figure 6.9 shows the projected boost in the DeepCore NMO sensitivity between the 3-year analysis and this work due to an increase in detector livetime by more than 3 times as well as improvements in the processing of the data sample, the modeling of uncertainties, and the analysis optimization. Despite these efforts, however, the sensitivity gain is seen to plateau due to the significant limitations imposed by the reconstruction and PID.

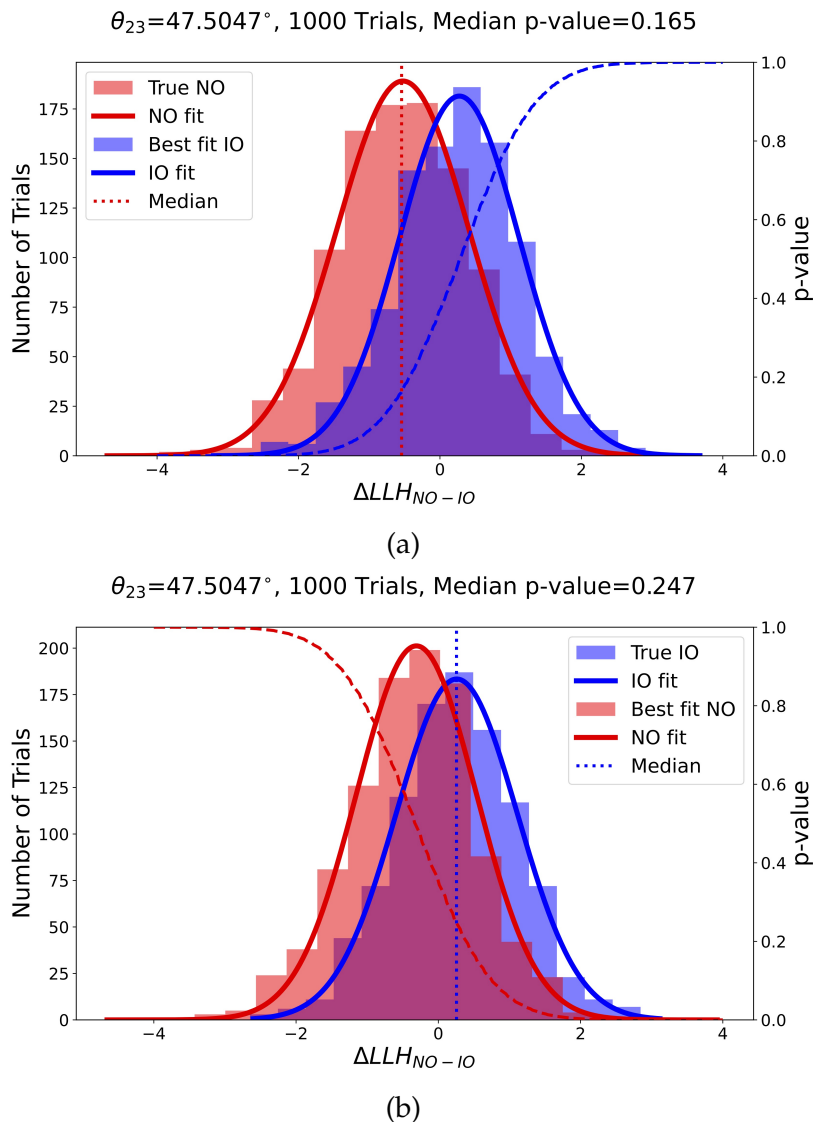


Figure 6.7: Pseudotrial ΔLLH_{IO-NO} distributions for true NO (top) and true IO (bottom) assuming atmospheric oscillation parameters at the DeepCore best fit point [42]. As expected, the distributions are well fitted by a Gaussian function.

Nevertheless, it is important to remember that this improvement is the projection at the median sensitivities. Figure 6.9 does not reflect possible cases of the observed value not lying at the median of the true ordering distribution.

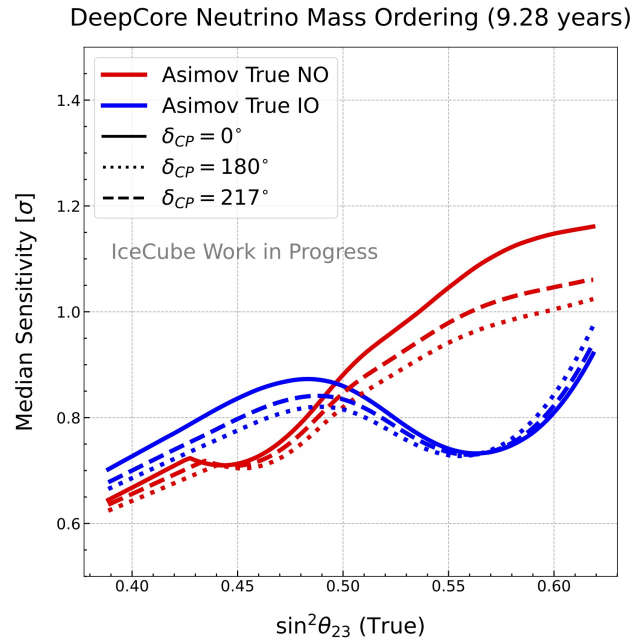


Figure 6.8: NMO sensitivity dependence on the δ_{CP} parameter. The sensitivity is plotted for three representative values of δ_{CP} . A negligible dependence on the phase is observed.

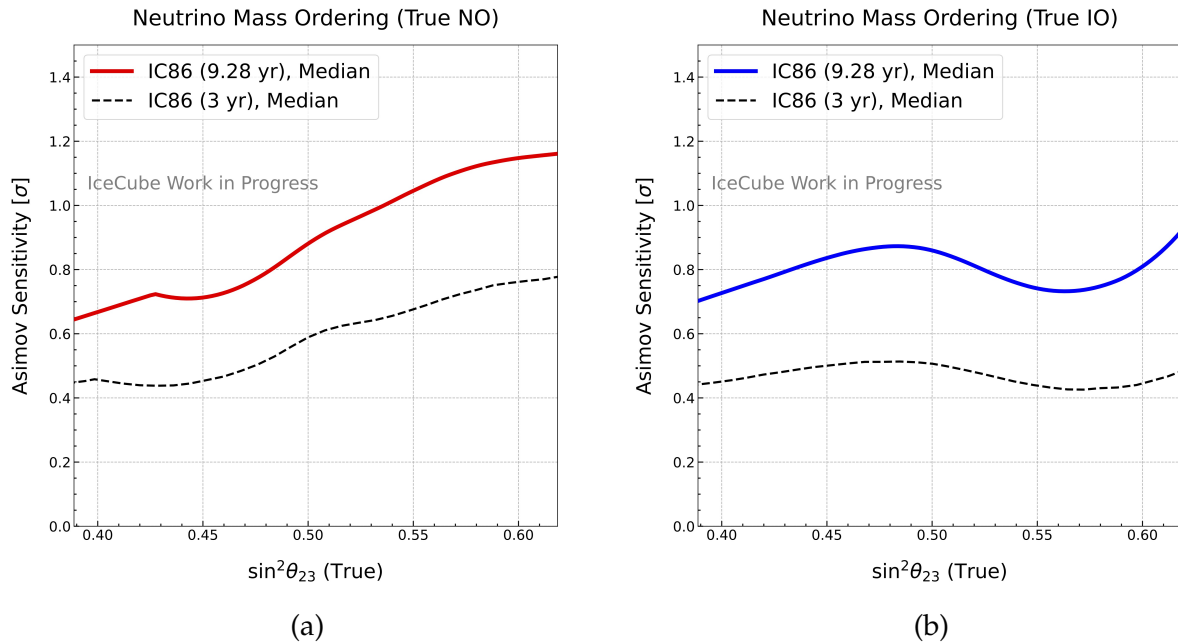


Figure 6.9: Comparison of the DeepCore NMO median sensitivity between the 3-year analysis [40] and this work. The sensitivity gain is a result of an increase in detector livetime by more than 3 times as well as improvements in the processing of the data sample, the modeling of uncertainties, and the analysis optimization.

Chapter 7

Blind Fit to the Data

7.1 Blind Fit Procedure

The term *blind fit* denotes a series of checks performed on the goodness of fit to the real data such that the analysis result is not unveiled. Blind fits represent an intermediate step before the full *unblinding* of the result to ensure that all analysis components are behaving in a sensible way. Table 7.1 shows the blind fit procedure performed for the NMO analysis consisting of six different steps. Each step includes a test and a corresponding stop condition, which denotes a bound for "needing further study". Surpassing this bound does not necessarily mean that something is wrong, but rather, it is an indication that one should look more closely at this component of the analysis. In general, the stop condition values are set using common statistical guidelines (i.e. p-value threshold of 5%). However, an analysis-specific study is performed to determine the particular values for the bin-wise pulls (Step 3). This is further discussed in Subsection 7.2.1.

7.2 Blind Fit Results

The first step of the blind fit procedure consists in performing a fit for each mass ordering of the MC template to the real observed data template. Any information revealing which

| Step | Test | Stop Condition | Report |
|------|---|--|---|
| 1 | Fit both orderings to the real data | N/A | Keep preference blind and use preferred ordering for next steps |
| 2 | Parameter pulls: Non-detector | one or more parameters pulling $> 2\sigma$ or at boundary for no prior | Absolute pulls in σ and distances to boundary |
| 2 | Parameter pulls: DOM efficiency | Fit outside of [-10%, +10%] | Absolute pull in σ |
| 2 | Parameter pulls: Detector (except DOM eff.) | At boundary | Distance to boundary |
| 3 | Bin-wise pulls | 1 or more bins pulling $> 4.5\sigma$ 2 or more bins pulling $> 3\sigma$ 3 or more bins pulling $> 2.2\sigma$ 4 or more bins pulling $> 1.8\sigma$ | Plot of 1D and 2D pulls |
| 4 | Goodness of fit | One sided p-value $< 5\%$ | Plot of LLH distribution Data p-value |
| 5 | Data-MC agreement | One sided p-value $< 5\%$ | Plots and p-value of energy, $\cos(\theta_{zenith})$, and PID |
| 6 | Unphysical fit check | $\sin^2(2\theta_{23}) > 95\%$ of trials | Yes/No |

Table 7.1: Blind fit procedure performed for the NMO analysis. The stop condition denotes a bound for "needing further study".

of the two mass orderings is the better fit is kept hidden to avoid unblinding the result. Thus, only the "blinded" preferred ordering fit is gauged in the following steps.

7.2.1 Parameter and Bin-wise Pulls

In the second step, parameter pulls for the preferred fit are assessed. These are expected to lie within the bounds of their corresponding stop condition denoting the stability of the best fit parameter value. Too large of a parameter pull is an indication that the fit prefers a value that is significantly different from the nominal value. For parameters that without a Gaussian prior, this is acceptable as all values in the parameter range are weighed equally. However, for parameters constrained by Gaussian priors, this can be an indication that something unexpected or interesting is occurring as the Gaussian prior is

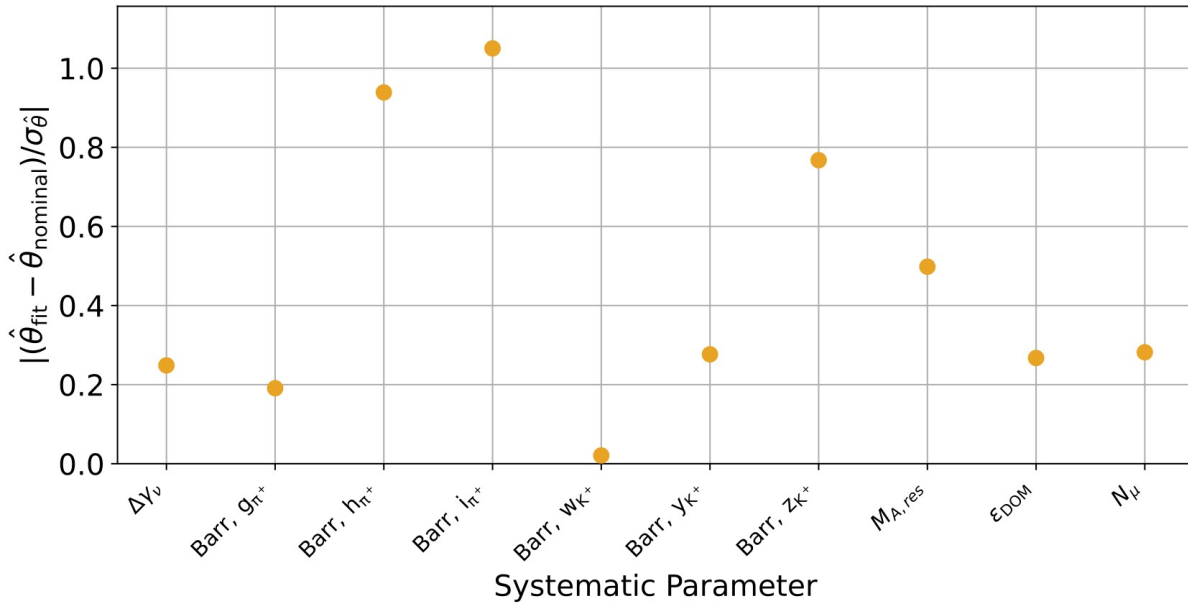


Figure 7.1: Best fit pulls for all parameters with Gaussian priors. As can be seen, no pulls hit their corresponding stop condition.

| Parameter | Distance to Nearest Boundary |
|---------------------|------------------------------|
| N_ν | 0.809 |
| Hole Ice p_0 | 0.380 |
| Hole Ice p_1 | 0.140 |
| Bulk Ice Absorption | 0.066 |
| Bulk Ice Scattering | 0.163 |
| Birefringence | 0.428 |
| Muon Light Yield | 0.273 |

Table 7.2: Distance to the nearest boundary for all analysis parameters with no prior.

based on well-founded external data. Figure 7.1 shows the best fit pulls for all parameters with Gaussian priors. As can be seen, no pulls hit their corresponding stop condition. Table 7.2 shows the distance to the nearest boundary for all analysis parameters with no prior. Note that the two oscillation parameters are excluded here as their values are measured and reported in Chapter 8 as part of the unblinding process of the analysis.

Bin-wise pulls between the observed data and the preferred fit are also gauged as part

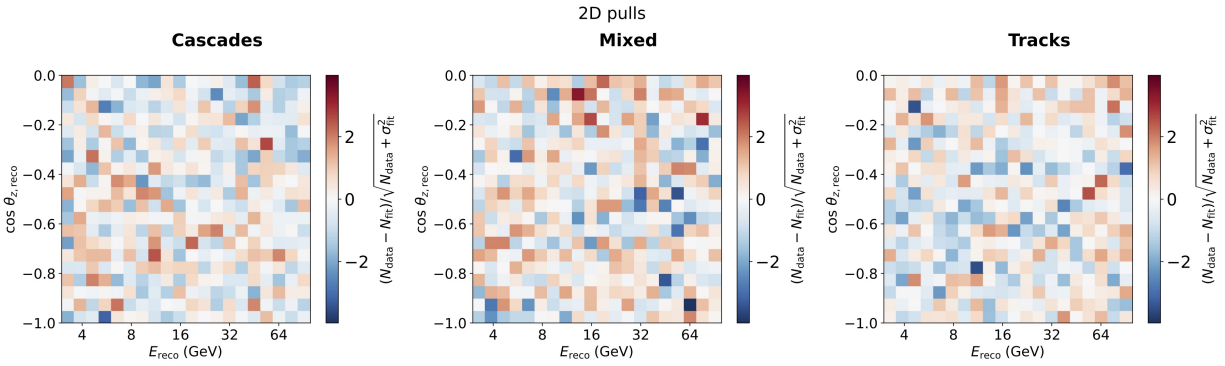


Figure 7.2: Best fit 2D bin-wise pulls. No pulls are found to hit the stop conditions.

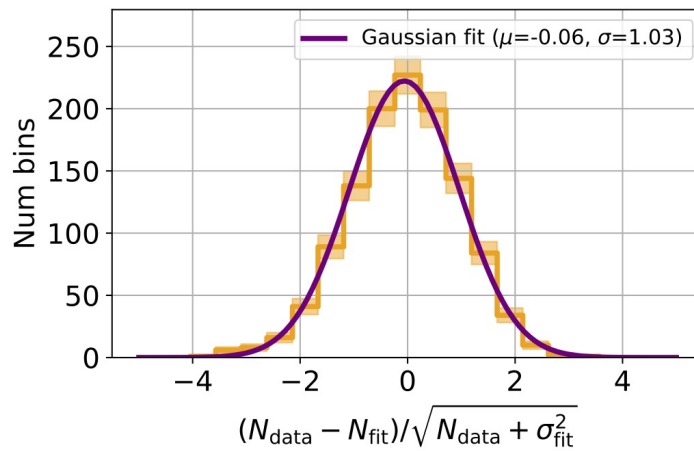


Figure 7.3: Best fit 1D bin-wise pulls. A Gaussian distribution is observed with a mean close to 0 and a standard deviation close to 1 in agreement with the expectation of bin-wise statistical fluctuations.

of Step 3 of the blind fit procedure. In general, bins should not pull past any of the stop conditions. If this occurs, it represents an unexpected difference between the data and the MC simulation, and thus, would be a cause for further study. Figure 7.2 shows the best fit 2-dimensional bin-wise pulls for the NMO analysis. No pulls are found to hit the stop conditions. Figure 7.3 shows the 1-dimensional distribution of the bin-wise pulls, where a Gaussian distribution with a mean close to 0 and a standard deviation close to 1 is observed in agreement with the expectation of bin-wise statistical fluctuations.

7.2.1.1 Bin-wise Pulls Stop Condition

A study is performed to determine the specific stop conditions set for the bin-wise pulls to ensure that these represent an accurate expectation of the analysis given the large number of bins. Thus, each stop condition is chosen such that the probability of hitting it is close to 1%. This probability is quantified in the following way:

1. Perform the Ensemble Test for 900 pseudotrials assuming an MC data template at nominal for both true NO and true IO.
2. Evaluate how many pseudotrial fits fail the given bin-wise pull stop condition.
3. Compute the probability to fail the given condition as

$$P = \frac{\text{Number of pseudotrials that failed}}{\text{Total number of pseudotrials}} . \quad (7.1)$$

Note that the probability for the condition of *observing 1 or more bins pulling* $> 4.5\sigma$ is calculated differently, mainly, using

$$P(\text{at least one bin} > 4.5\sigma) = 1 - P(\text{one bin} < 4.5\sigma)^N \quad (7.2)$$

where N is the total number of bins in the analysis.

7.2.2 Goodness of Fit

Step 4 consists in assessing the goodness of fit on the real data as compared to the expected pseudotrial distribution, which assumes an MC data template at nominal. This check is considered essential in the blind fit procedure as it compares the ability of the MC simulation to model the real data. Figure 7.4 shows the results of this test, and as can be seen, the p-value lies well within the bounds of statistical uncertainty, denoting an acceptable MC modeling.

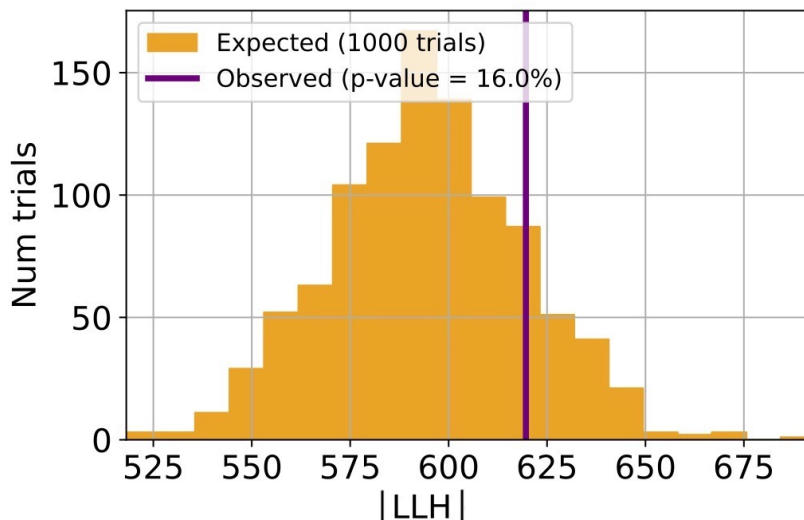


Figure 7.4: Goodness of fit on the real data as compared to the expected pseudotrial distribution, which assumes an MC data template at nominal. The p-value lies well within the bounds of statistical uncertainty, denoting an acceptable MC modeling.

7.2.3 Post Fit Data-MC Agreement

Step 5 of the blind fit procedure evaluates the data-MC agreement between the real data and the preferred fit for each of the three analysis bins— neutrino energy, $\cos(\theta_{zenith})$, and PID. The results of this test are found in Figure 7.5, where overall good agreement is seen between the data and MC. Nevertheless, the p-value stop condition is observed to fail slightly for the $\cos(\theta_{zenith})$ distribution. This effect arises from one outlier bin between $[-0.8, -0.65]$, which is found to be consistent with a statistical fluctuation. The p-value is re-calculated without this bin and is found to yield 25.6%— well above the stop condition. Figure 7.6 shows a "zoomed in" version of the $\cos(\theta_{zenith})$ distribution for the range around the outlier, subdivided into smaller bins. From the figure, one can see an oscillatory pattern emerge in the ratio, likely due to statistical fluctuations.

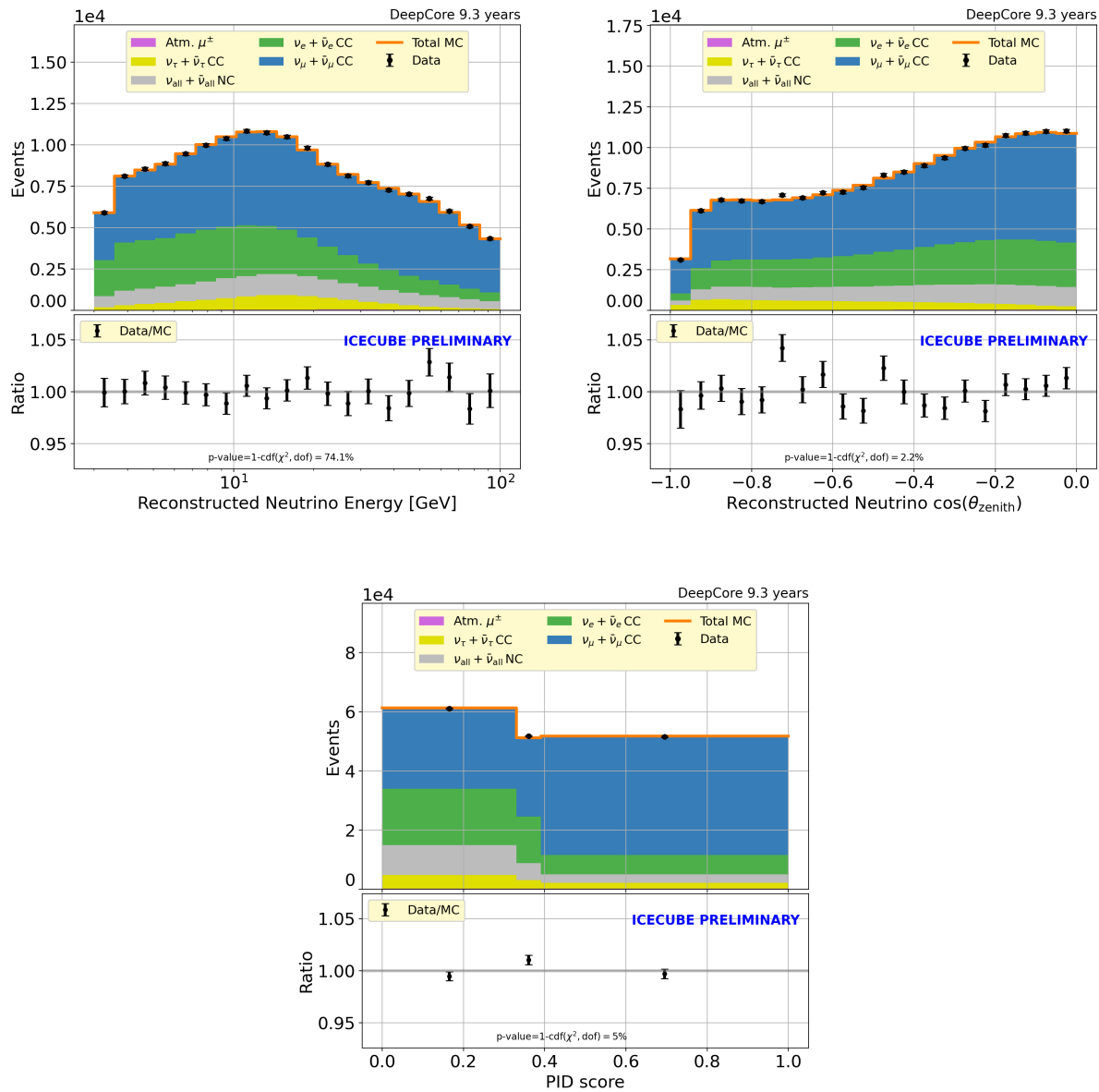


Figure 7.5: Data-MC agreement between the real data and the preferred fit for each of the three analysis bins. Although overall good agreement is seen between the data and MC, the p-value stop condition is observed to fail slightly for the $\cos(\theta_{\text{zenith}})$ distribution. This effect arises from one outlier bin between $[-0.8, -0.65]$, which is found to be consistent with a statistical fluctuation.

7.2.4 Unphysical Fit Check

The last step of the blind fit procedure checks for a possible unphysical fit of the MC template. An unphysical fit can occur if the background is underestimated, leading to an

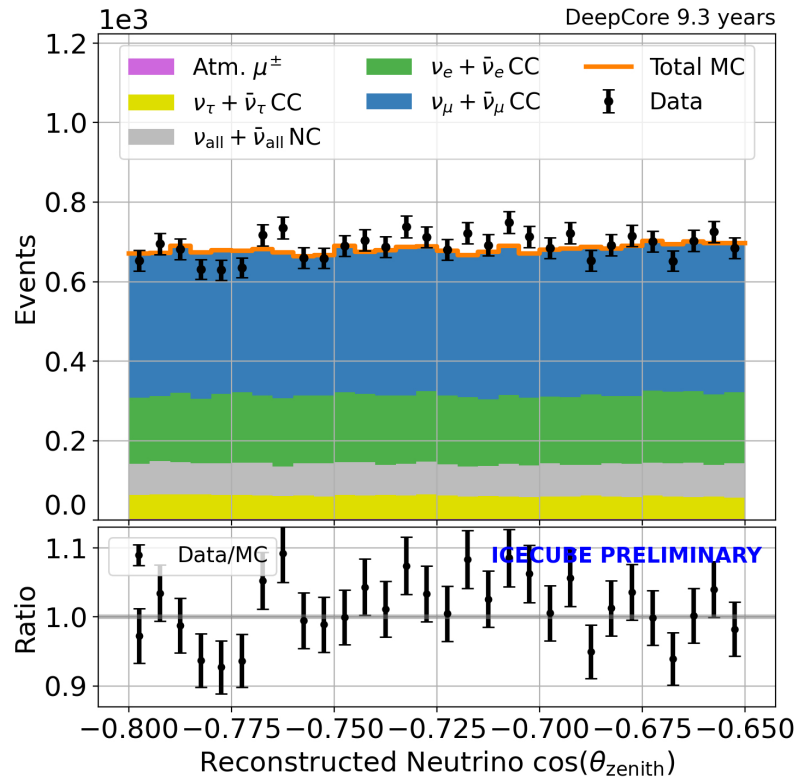


Figure 7.6: "Zoomed in" version of the $\cos(\theta_{zenith})$ distribution for the range around the outlier, subdivided into smaller bins. An oscillatory pattern emerges in the ratio, likely due to statistical fluctuations.

enhancement in the oscillation amplitude. Because a fit of the θ_{23} parameter creates an upper bound in the amplitude at 45° , the fit is performed instead using $\sin^2(2\theta)$, where this one is bounded between $[0, 1.75]$. The preferred $\sin^2(2\theta)$ fit to the real data is then compared to the corresponding $\sin^2(2\theta)$ distribution of pseudotrials. If the observed value lies within the bounds of a statistical fluctuation, the test returns "yes", meaning that there is no unphysical fit. Otherwise, it returns "no". For the NMO analysis, no unphysical fit is observed.

Chapter 8

Analysis Results

8.1 Unblinding Procedure

Figure 8.1 shows a diagram outlining the NMO unblinding procedure. Due to the non-nested feature of the NO and IO hypotheses, the *unblinding* procedure for quantifying the analysis result follows a different approach to the standard $\sqrt{\Delta\chi^2}$ (or $\sqrt{2|\Delta\text{LLH}|}$) Wilks' calculation [68] in a similar manner as the Pseudotrial Method discussed in Section 6.1. The procedure consists of the following steps:

1. Perform a fit of the NO and IO theory templates to the real data template and compute an *observed* test statistic value of $\Delta\text{LLH}_{\text{NO-IO}}$.
2. Generate a "true NO" MC simulation template using the NO best-fit parameters from the real data fit. Label this as the *NO best fit to the real data*.
3. Statistically fluctuate the "true NO" MC template 1000 times to generate 1000 fluctuated pseudotrials. This constitutes the distribution of statistically plausible data templates assuming that the real data is well-represented by the NO hypothesis.
4. Perform a fit of the NO and IO theory templates to each pseudotrial and assemble a true NO $\Delta\text{LLH}_{\text{NO-IO}}$ distribution.

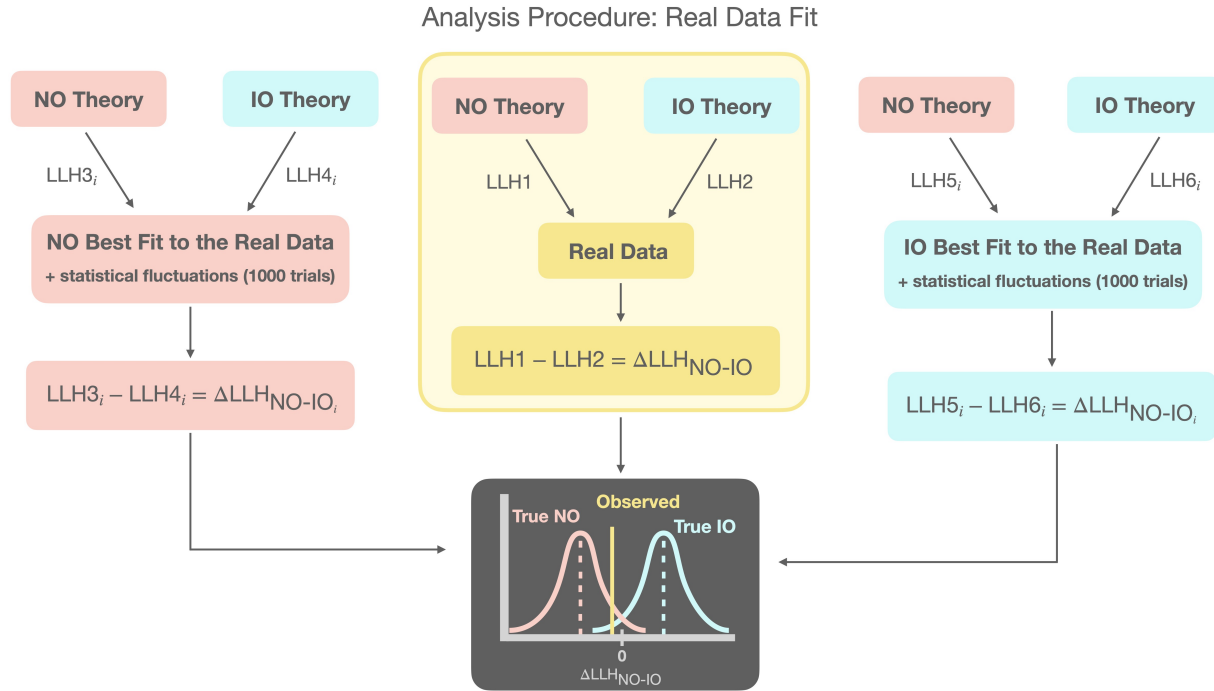


Figure 8.1: Diagram of the NMO analysis unblinding procedure for quantifying the results of the fit to the real data.

5. Repeat Steps 2 through 4 for "true IO".
6. Compute a one-tailed p-value for each mass ordering with respect to the observed ΔLLH_{NO-IO} value in the same way as in the Pseudotrial Method.
7. Calculate a CL_s value [60; 61] using

$$CL_s = \frac{P_{\text{opposite}}}{1 - P_{\text{preferred}}} \quad (8.1)$$

where $p_{\text{preferred}}$ and p_{opposite} are the p-values corresponding to the preferred and opposite mass ordering, respectively.

8. Quantify the exclusion interval using $CL = 1 - CL_s$.

In general, p_{opposite} denotes the probability of having observed the given result by random chance under the assumption of a true opposite (non-preferred) ordering. This alone can be inserted into Equation 6.1 to calculate a significance provided that the observed value of

$\Delta LLH_{\text{NO-IO}}$ is at the *median* of the preferred ordering distribution as discussed in Chapter 6. However, when evaluating a fit to the real data, it is likely that the observed value will not lie precisely at the median of the distribution due to statistical fluctuations in the data or slight differences between the data and the MC simulation. To account for this in models that are not highly sensitive, a conservative CL_s Method [60; 61] is performed instead, which incorporates *both* mass ordering p-values, as shown in Equation 8.1, to calculate an exclusion interval and significance. The CL_s value spans a range of $[0, 1]$, where a value close to zero denotes a strong disfavoring of the opposite ordering while a value close to one does not necessarily indicate any favoring. The CL_s Method imposes a correction factor on the value of p_{opposite} to generate an *effective* p-value based on the positioning of the observed value relative to both mass ordering distributions. This effective p-value, p_{CL_s} , can be denoted as

$$p_{\text{CL}_s} = \text{CL}_s = \left(\frac{1}{1 - p_{\text{preferred}}} \right) p_{\text{opposite}} \quad (8.2)$$

where the term in front of p_{opposite} represents the correction factor and $\text{CL} = 1 - p_{\text{CL}_s}$. To calculate a significance value, it is appropriate to modify the sensitivity (or significance) calculation from Equation 6.1 to follow that of a two-tailed Gaussian approach [3] such that

$$\eta_\sigma = \sqrt{2} \text{erfc}^{-1}(p_{\text{two-tailed}}) \quad (8.3)$$

where $p_{\text{two-tailed}}$ is the two-tailed p-value. To understand this, one can think about an example where the observed value lies at exactly the median of the preferred ordering distribution. In this case, $p_{\text{preferred}}$ would equal 50%. Inserting this value into Equation 8.2, one obtains $p_{\text{CL}_s} = 2p_{\text{opposite}}$ which, using Equation 8.3, yields

$$\eta_{\sigma} = \sqrt{2}\operatorname{erfc}^{-1}(p_{\text{CL}_s}) \quad (8.4)$$

$$= \sqrt{2}\operatorname{erfc}^{-1}(2p_{\text{opposite}}) \quad (8.5)$$

$$= \sqrt{2}\operatorname{erfc}^{-1}(2p_{\text{one-tailed}}) \quad (8.6)$$

precisely recovering Equation 6.1 for the median sensitivity.

Moreover, one can also reconcile the CL_s Method to the example discussed in Section 6.1, where having no sensitivity to the mass ordering (both NO and IO distributions lie on top of each other) should yield a significance of 0σ no matter where the observed value lies. For an observed value lying to one of the sides of the true ordering distribution, $p_{\text{preferred}} = 1 - p_{\text{opposite}}$ leading to $p_{\text{CL}_s} = 1$. Using Equation 8.4, this yields exactly 0σ . On the contrary, for an observed value at the *median*, $p_{\text{preferred}} = p_{\text{opposite}} = 50\%$, equally leading to $p_{\text{CL}_s} = 1$. Thus, the CL_s Method yields the same median sensitivity values as the one-tailed approach from Chapter 6, but furthermore, it also corrects an otherwise overstated p-value in the case where the observed value lies to one of the sides of the true ordering distribution.

One example denoting the importance of the CL_s Method consists in thinking about the case where the observed value lies completely outside of either of the two distributions. This would indicate that there is no consistency between the observed value and either of the analysis predictions. In this case, using only the opposite ordering p-value would show a disproportionately large significance in rejecting the opposite ordering while not at all considering the preferred ordering distribution. Hence, it is imperative to consider the positioning of the true ordering distribution with respect to the observed value *unless* the observed value lies precisely at the center.

DeepCore Neutrino Mass Ordering (9.28 years)

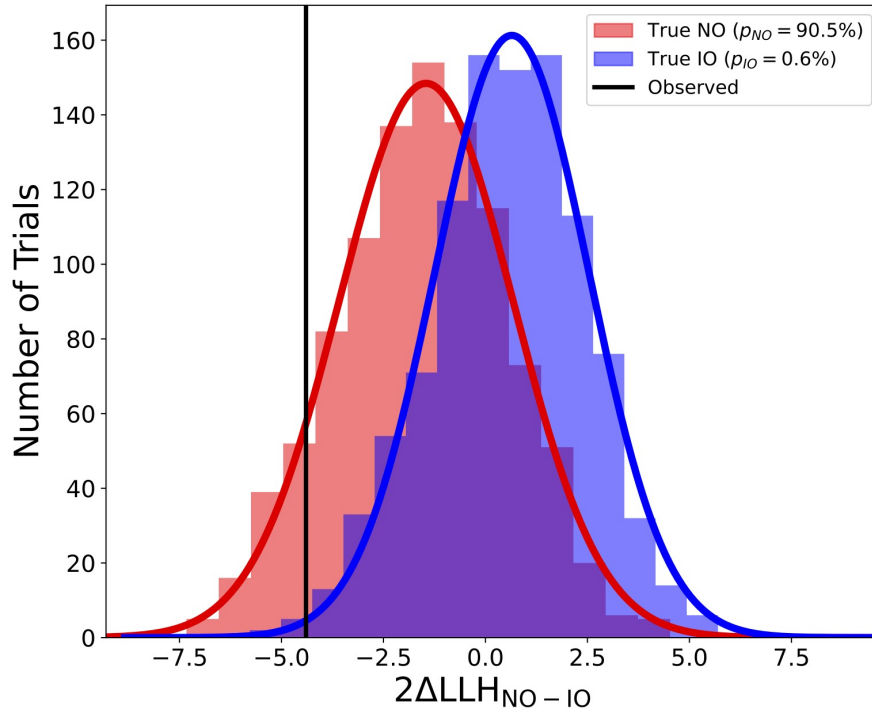


Figure 8.2: Results of the NMO analysis using 9.28 years of IceCube DeepCore data. The analysis observes a preference for the normal ordering over the inverted ordering at $2\Delta\text{LLH}_{\text{NO-IO}} = -4.398$, leading to a disfavoring of the inverted ordering at a 93.7% exclusion level, or 1.86σ .

8.2 Results

Figure 8.2 shows the results of the neutrino mass ordering analysis using 9.28 years of IceCube DeepCore data. The analysis observes a preference for the normal ordering over the inverted ordering at $2\Delta\text{LLH}_{\text{NO-IO}} = -4.398$ based on the presented frequentist method. The corresponding p-values consist of

$$p_{\text{IO}} = 0.6\% \quad (8.7)$$

$$p_{\text{NO}} = 90.5\% \quad (8.8)$$

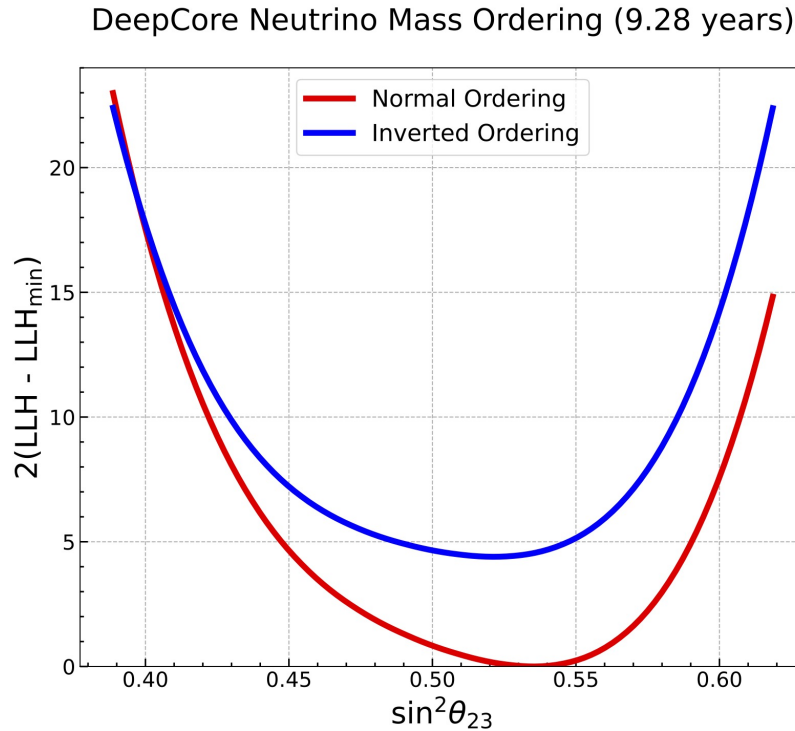


Figure 8.3: Difference between the LLH calculated at a given injected $\sin^2(\theta_{23})$ value and the global LLH minimum, or the best fit LLH. The normal ordering is preferred for values of $\sin^2(\theta_{23}) > 0.4$.

where p_{NO} is the preferred ordering p-value and p_{IO} is the opposite ordering p-value. This yields a CL_s value of

$$p_{\text{CL}_s} = \text{CL}_s = 6.3\% \quad (8.9)$$

leading to a disfavoring of the inverted ordering hypothesis at an exclusion level of 93.7%, or 1.86σ (using a two-tailed conversion as discussed in Section 8.1). Furthermore, Figure 8.3 shows the difference between the LLH calculated at a given injected $\sin^2(\theta_{23})$ value and the global LLH minimum, or the best fit LLH. As can be seen in the figure, the normal ordering is preferred for values of $\sin^2(\theta_{23}) > 0.4$.

Table 8.1 shows the best fit parameters for a fit of the NO and IO theory to the real data, where all parameters are observed to lie to close to their respective nominal values. An

Table 8.1: List of the NO and IO best fit parameter values for a fit to the real data for all free analysis parameters. The nominal value and the allowed bound is included for reference.

| Parameter | Nominal Value | Prior | Range | NO Best Fit | IO Best Fit |
|--------------------------------|---|-------------------------------|------------------------------|---------------------------------------|--|
| Flux: | | | | | |
| $\Delta\gamma_V$ | 0 | Gaussian, $\sigma = \pm 0.1$ | [-0.5, 0.5] | -0.0249 | -0.0286 |
| Barr g_ π^+ | 0 | Gaussian, $\sigma = \pm 0.3$ | [-1.5, 1.5] | -0.0572 | -0.0435 |
| Barr h_ π^+ | 0 | Gaussian, $\sigma = \pm 0.15$ | [-0.75, 0.75] | -0.1408 | -0.1428 |
| Barr i_ π^+ | 0 | Gaussian, $\sigma = \pm 0.61$ | [-3.05, 3.05] | 0.6406 | 0.6738 |
| Barr w_ K^+ | 0 | Gaussian, $\sigma = \pm 0.4$ | [-2.0, 2.0] | -0.0083 | -0.0495 |
| Barr y_ K^+ | 0 | Gaussian, $\sigma = \pm 0.3$ | [-1.5, 1.5] | -0.0830 | -0.0979 |
| Barr z_ K^+ | 0 | Gaussian, $\sigma = \pm 0.61$ | [-3.05, 3.05] | -0.4681 | -0.4531 |
| Neutrino Normalization: | | | | | |
| N_V | 1.0 | Uniform | [0.1, 2.0] | 0.9091 | 0.9019 |
| Cross Section: | | | | | |
| $M_{A,RES,CC}$ | 0 | Gaussian, $\sigma = \pm 1.0$ | [-2.0, 2.0] | -0.4981 | -0.4671 |
| Detector: | | | | | |
| DOM Efficiency | 1.0 | Gaussian, $\sigma = \pm 0.1$ | [0.8, 1.2] | 1.0267 | 1.0350 |
| Hole Ice p_0 | 0.102 | Uniform | [-0.6, 0.5] | -0.2196 | -0.2323 |
| Hole Ice p_1 | -0.0493 | Uniform | [-0.2, 0.2] | -0.0602 | -0.0579 |
| Bulk Ice Absorption | 1.0 | Uniform | [0.9, 1.1] | 0.9661 | 0.9675 |
| Bulk Ice Scattering | 1.05 | Uniform | [0.85, 1.25] | 1.0132 | 1.0136 |
| Birefringence | 0 | Uniform | [0, 1.0] | 0.4281 | 0.4190 |
| Muon Light Yield | 0 | Uniform | [0, 1.0] | 0.2730 | 0.2621 |
| Oscillations: | | | | | |
| θ_{23} | 47.5047 $^\circ$ | Uniform | [38 $^\circ$, 52 $^\circ$] | 47.0239 $^\circ$ | 46.2233 $^\circ$ |
| Δm_{31}^2 | $\pm 2.47467 \times 10^{-3} \text{ eV}^2$ | Uniform | $\pm [0.001, 0.004]$ | $2.44933 \times 10^{-3} \text{ eV}^2$ | $-2.30715 \times 10^{-3} \text{ eV}^2$ |
| Atmospheric Muons: | | | | | |
| N_μ | 1.0 | Gaussian, $\sigma = \pm 0.4$ | [0.1, 3.0] | 0.8873 | 0.8561 |

interesting check, then, consists in roughly comparing the $\Delta\text{LLH}_{\text{NO-IO}}$ MC distributions in Figure 6.7a— generated at the nominal true NO and best fit IO parameter values —to the MC distributions generated at the real data best fit point of each mass ordering. Figure 8.4 shows the p-value for the hypothetical case of the observed value lying at the median of the best fit NO distribution. Comparing the two figures, one can see that both p_{IO} values are similar as expected.

Table 8.2 shows a comparison between the 3-year DeepCore NMO results [40] and this work. As can be seen from the sign of the observed $2\Delta\text{LLH}_{\text{NO-IO}}$ value in the table, the 3-year result observed a preference for the normal ordering over the inverted ordering similarly to the 9.28-year result; therefore, the CL_s value represents the degree of disfavoring of the inverted ordering.

DeepCore Neutrino Mass Ordering (9.28 years)

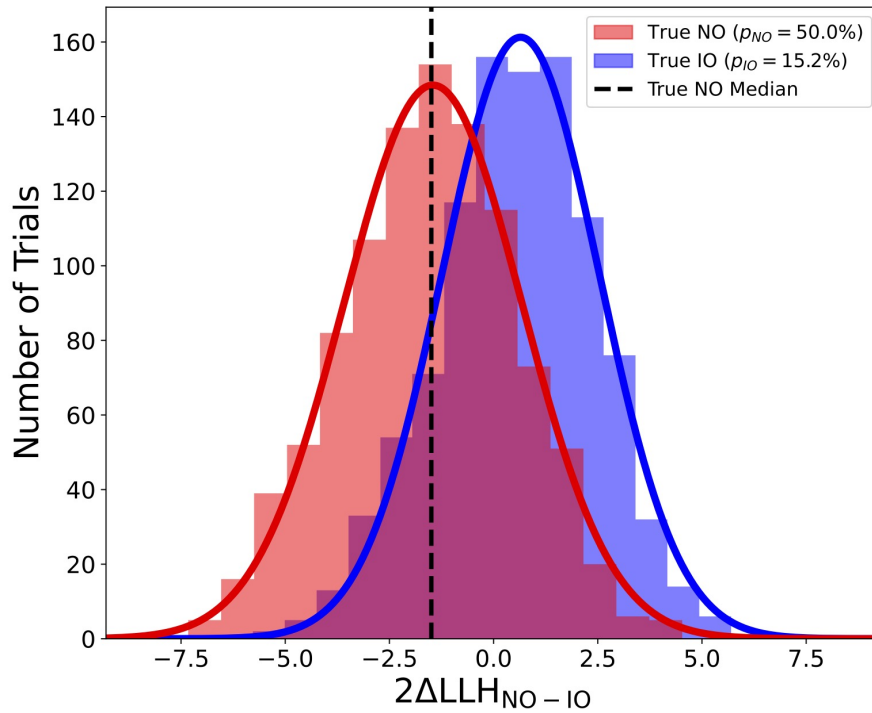


Figure 8.4: IO p-value for the hypothetical case of the observed value lying at the NO median, where each distribution is generated at its respective real data best fit point. As expected, the p-value is similar to the one found in Figure 6.7a for distributions generated at the nominal true NO and best fit IO parameter values.

| | 3-Year DeepCore | 9.28-Year DeepCore (this work) |
|---------------------------------------|-----------------|--------------------------------|
| Observed $2\Delta LLH_{\text{NO-IO}}$ | -0.738 | -4.398 |
| P_{IO} | 15.7% | 0.6% |
| P_{NO} | 71.1% | 90.5% |
| CL_s | 53.3% | 6.3% |

Table 8.2: Comparison between the 3-year DeepCore NMO results [40] and this work. Clear improvement in the robustness of the results can be observed, where a stronger preference for the normal ordering is now found.

All in all, a clear improvement in the robustness of the results can be observed, where a stronger preference for the normal ordering is now found. Nevertheless, it is important to note that, due to the location of the observed value line in Figure 8.2— mainly, at the tail of the true IO distribution —the results presented in this dissertation are contingent upon the generation of more pseudotrials. With the current number of pseudotrials, there is a 1σ uncertainty on the value of p_{IO} of roughly 40%, meaning that the value of p_{IO} could vary by $\pm 0.24\%$.

Chapter 9

Conclusion and Outlook

As discussed throughout this dissertation, the IceCube experiment provides a new window into the measurement of the neutrino mass ordering. Through its atmospheric baseline and its specific arrangement, DeepCore lies in a favorable position to contribute an NMO result that is both independent of the δ_{CP} phase and generated at neutrino energies greater than those observed by any other experiment.

The work presented in this dissertation showed the latest IceCube DeepCore measurement of the NMO using a 9.28-year data sample. Clear improvement in the robustness of the measurement is seen in comparison to the 3-year DeepCore NMO results [40] as well as a preference for the normal ordering that is consistent with the latest Super-Kamiokande results [44].

Looking ahead towards the future, the IceCube experiment expects to conduct a measurement of the neutrino mass ordering with the new IceCube Upgrade [58]— a low-energy extension of the DeepCore subarray scheduled for deployment between the years of 2025 and 2026. The Upgrade will add 7 more compact Upgrade strings to the DeepCore region with 20 m horizontal spacing and a 3 m vertical DOM spacing. Due to the smaller spacing, it is expected that IceCube will have the ability to detect neutrino events with energies down to about 1 GeV, greatly improving the robustness of an NMO measurement. This

improvement arises mainly from both a better coverage of the NMO signal region as well as a more accurate event reconstruction and PID.

To conclude, a very promising outlook exists for the neutrino mass ordering in the coming years. A range of upcoming experiments such as the IceCube Upgrade [58], the Hyper-Kamiokande experiment [69], the Jiangmen Underground Neutrino Observatory (JUNO) [8], and the Deep Underground Neutrino Experiment (DUNE) [23] are currently being developed with a goal of measuring this elusive ordering. If just one of these is successful, it would not only greatly improve our understanding of neutrinos but also of the workings of our universe as a whole.

Appendix A

Lowering the Analysis Energy Range

A.1 MC Simulation Threshold

Because MC simulation was not generated for events with *true* energies below 1 GeV, a check was made to ensure that only a negligible amount of these unsimulated events can be incorrectly reconstructed in the observed data sample to energies greater than 3 GeV. Figure A.1 shows a distribution of the raw MC event counts (as opposed to the weighted *expected* events discussed in Subsection 3.1.1) as a function of the true neutrino energy for both the analysis and default reconstructed energy lower limits. An extrapolation fit shows that roughly 300 unsimulated events can enter the sample as a result of lowering the energy threshold, denoting 0.01% of the sample. Thus, any impact from these unsimulated events is negligible.

A.2 Study on Cross-Section Systematics

As a result of lowering the energy range of the analysis to 3 GeV, a study was performed to ensure that no cross-section parameters with potential to impact events at low energies were unaccounted for. The following cross-section parameters were assessed:

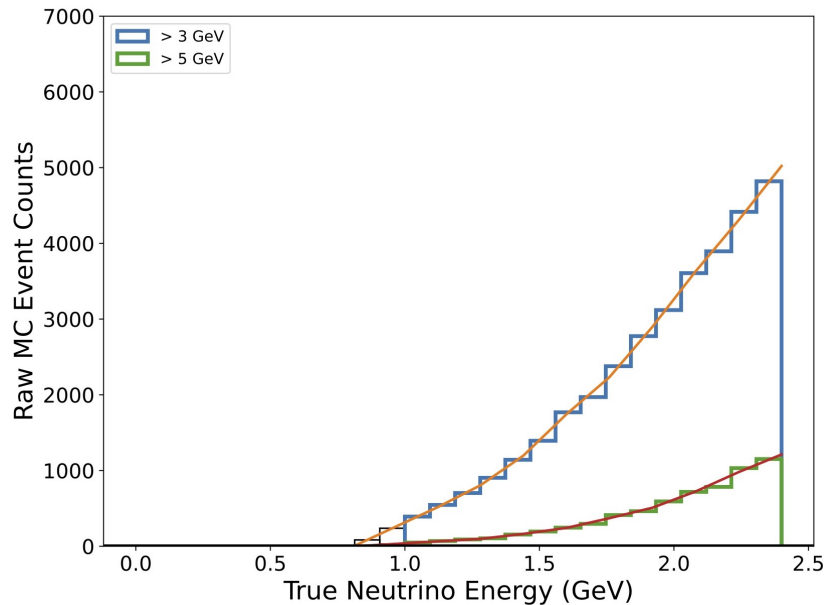


Figure A.1: Distribution of the raw MC event counts for both the analysis and default reconstructed energy lower limits. An extrapolation fit shows that a negligible 300 unsimulated events can enter the observed data (0.01% of the sample).

- $M_{A,QE}$ NC
- $M_{A,C0-\pi}$, CC and NC
- Bodek-Yang variables (A_{HT} , B_{HT} , C_{v1u} , and C_{v2u}), CC and NC

For each parameter, events were re-weighted to their corresponding $\pm 2\sigma$ parameter variation. Thus, one can plot the relative percentage difference in the expected events between the distribution generated using the parameter's nominal and $\pm 2\sigma$ variation values and gauge the impact of the parameter.

Figure A.2 shows the relative percentage difference obtained for the Bodek-Yang variables. The value inside each plot shows the largest relative difference found in any given bin. A minimum value of 5% relative difference was imposed to study the parameter further. All of the above-mentioned parameters either fell below this threshold or contained one or two bins slightly above the threshold, which, given the total number of bins, can easily occur due to statistical fluctuations.

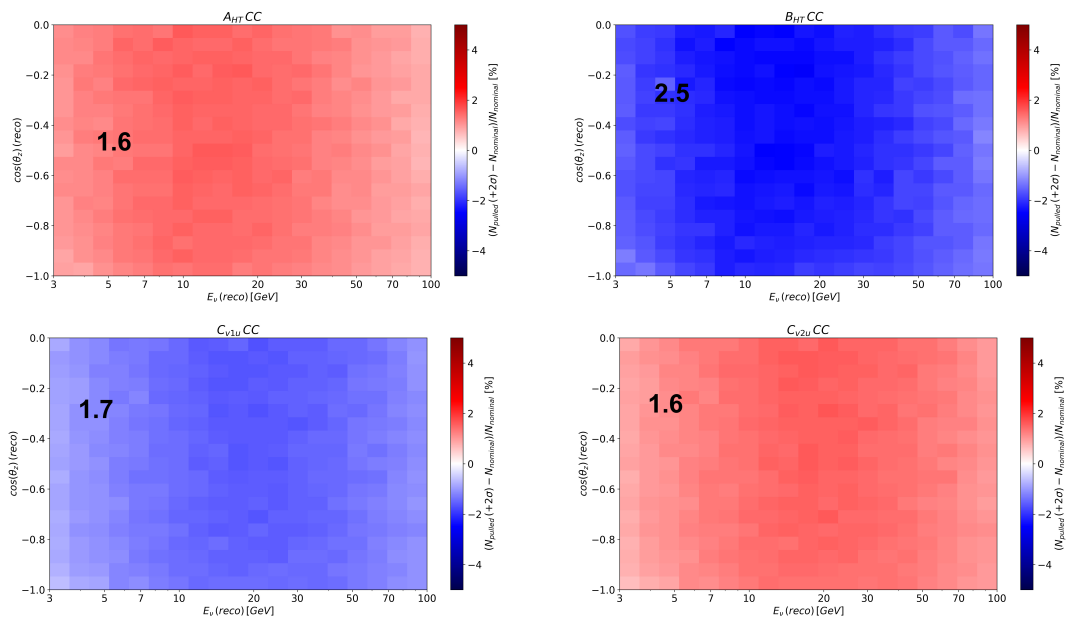


Figure A.2: The relative percentage difference for the Bodek-Yang variables for a 2σ variation in comparison to the nominal values of the parameters. The value inside each plot shows the largest difference found in any given bin of the distribution.

Appendix B

Check on the Hypersurfaces

To ensure that effects such as the tau production energy threshold do not affect the validity of the hypersurface fits, a minimum threshold condition is placed on $N_{\text{fitted points}}$, mainly, that $N_{\text{fitted points}} > N_{\text{params}}$ (refer back to Subsubsection 4.3.1.3). To further elaborate, the value of $N_{\text{fitted points}}$ decreases as a result of a dropped re-weight factor, which occurs whenever a bin in either the nominal or MC set has zero expected counts. The minimum threshold, then, ensures that the number of unpopulated bins obtained by further separating the PID bins by flavor signature do not jeopardize the fit.

Bibliography

- [1] IceCube Gallery. <http://gallery.icecube.wisc.edu>. Accessed: May 3rd, 2024.
- [2] V. Barger, D. Marfatia, and K. Whisnant. Breaking eightfold degeneracies in neutrino CP violation, mixing, and mass hierarchy. *Phys. Rev. D*, 65:073023, 2002. doi: 10.1103/PhysRevD.65.073023.
- [3] M. Blennow, P. Coloma, P. Huber, and T. Schwetz. Quantifying the sensitivity of oscillation experiments to the neutrino mass ordering. *J. High Energ. Phys.*, 2014(28), 2014. doi: 10.1007/JHEP03(2014)028.
- [4] L. M. Brown. The idea of the neutrino. *Physics Today*, 31(9):23–28, 1978. doi: 10.1063/1.2995181.
- [5] J. Chadwick. Intensitätsverteilung im magnetischen spectrum der β -strahlen von radium B + C. *Verhandl. Dtsc. Phys. Ges.*, 16, 1914. URL <https://cds.cern.ch/record/262756?ln=en>.
- [6] E. Ciuffoli, J. Evslin, and X. Zhang. Confidence in a neutrino mass hierarchy determination. *J. High Energ. Phys.*, 2014(95), 2014. doi: 10.1007/JHEP01(2014)095.
- [7] T.E. Coan and J. Ye. Muon physics. <http://www.phys.utk.edu/labs/Muon%20Physics/Coan%20&%20Ye%20Muon%20Physics%20Manual.pdf>. Accessed: May 3rd, 2024.
- [8] JUNO Collaboration. JUNO physics and detector. *Progress in Particle and Nuclear Physics*, 123:103927, 2022. ISSN 0146-6410. doi: 10.1016/j.pnpnp.2021.103927.
- [9] The Borexino Collaboration. Comprehensive measurement of pp -chain solar neutrinos. *Nature*, 562:505–510, 2018. doi: 10.1038/s41586-018-0624-y.
- [10] The KATRIN Collaboration. Direct neutrino-mass measurement with sub-electronvolt sensitivity. *Nat. Phys.*, 18:160–166, 2022. doi: 10.1038/s41567-021-01463-1.

- [11] J. Conrad, A. de Gouvêa, S. Shalgar, and J. Spitz. Atmospheric tau neutrinos in a multikiloton liquid argon detector. *Phys. Rev. D*, 82:093012, 2010. doi: 10.1103/PhysRevD.82.093012.
- [12] A. Cooper-Sarkar, P. Mertsch, and S. Sarkar. The high energy neutrino cross-section in the Standard Model and its uncertainty. *J. High Energ. Phys.*, 2011(42), 2011. doi: 10.1007/JHEP08(2011)042.
- [13] M. Ubieta Diaz. *Off-line commissioning of a non-destructive FT-ICR detection system for monitoring the ion concentration in the KATRIN beamline*. PhD thesis, Heidelberg University, Heidelberg, Germany, 2011.
- [14] A. M. Dziewonski and D. L. Anderson. Preliminary reference Earth model. *Physics of the Earth and Planetary Interiors*, 25(4):297–356, 1981. ISSN 0031-9201. doi: 10.1016/0031-9201(81)90046-7.
- [15] I. Esteban, M. Gonzalez-Garcia, and M. Maltoni et al. The fate of hints: updated global analysis of three-flavor neutrino oscillations. *J. High Energ. Phys.*, 2020(178), 2020. doi: 10.1007/JHEP09(2020)178.
- [16] A. Fedynitch et al. Calculation of conventional and prompt lepton fluxes at very high energy. *EPJ Web of Conferences*, 99:08001, 2015. doi: 10.1051/epjconf/20159908001.
- [17] A. Zhang et al. *Dive into Deep Learning*. Cambridge University Press, 2023. URL <https://D2L.ai>.
- [18] C. Andreopoulos et al. *The GENIE Neutrino Monte Carlo Generator: Physics and User Manual*, 2015. URL <https://arxiv.org/pdf/1510.05494>.
- [19] C. Kopper et al. *Clsim*, . URL <https://github.com/claudiok/clsim>.
- [20] G. D. Barr et al. Uncertainties in atmospheric neutrino fluxes. *Phys. Rev. D*, 74:094009, 2006. doi: 10.1103/PhysRevD.74.094009.
- [21] G. Ke et al. Lightgbm: A highly efficient gradient boosting decision tree. In I. Guyon et al., editor, *Advances in Neural Information Processing Systems*, volume 30. Curran Associates, Inc., 2017. URL https://proceedings.neurips.cc/paper_files/paper/2017/file/6449f44a102fde848669bdd9eb6b76fa-Paper.pdf.
- [22] H. R. Sharma et al. Study of pion production in ν_μ interactions on ^{40}Ar in DUNE using GENIE and NuWro event generators. *Phys. Part. Nuclei Lett.*, 19:724–739, 2022. doi: 10.1134/S1547477122060267.
- [23] J. Butler et al. Report of the 2021 U.S. community study on the future of particle physics (Snowmass 2021). *Snowmass, Seattle, WA (United States), September 2021*, 2023. doi: 10.2172/1922503. URL <https://www.osti.gov/biblio/1958170>.
- [24] J. Hewett et al. Neutrino scattering. In *2011 workshop on Fundamental Physics at the Intensity Frontier*, Rockville, MD, USA, 2012. doi: 10.2172/1042577.

- [25] K. J. Kelly et al. Neutrino mass ordering in light of recent data. *Phys. Rev. D*, 103:013004, 2021. doi: 10.1103/PhysRevD.103.013004.
- [26] M. Dunsch et al. Recent improvements for the lepton propagator PROPOSAL. *Computer Physics Communications*, 242:132–144, 2019. ISSN 0010-4655. doi: 10.1016/j.cpc.2019.03.021.
- [27] M. G. Aartsen et al. Measurement of South Pole ice transparency with the IceCube LED calibration system. *Nuclear Instruments and Methods in Physics Research Section A: Accelerators, Spectrometers, Detectors and Associated Equipment*, 711:73–89, 2013. ISSN 0168-9002. doi: 10.1016/j.nima.2013.01.054.
- [28] M. G. Aartsen et al. The IceCube Neutrino Observatory: instrumentation and online systems. *JINST*, 12:P03012, 2017. doi: 10.1088/1748-0221/12/03/P03012.
- [29] M. G. Aartsen et al. PINGU: a vision for neutrino and particle physics at the South Pole. *J. Phys. G: Nucl. Part. Phys.*, 44:054006, 2017. doi: 10.1088/1361-6471/44/5/054006.
- [30] M. Ghosh et al. New look at the degeneracies in the neutrino oscillation parameters, and their resolution by T2K, NO ν A and ICAL. *Phys. Rev. D*, 93:013013, 2016. doi: 10.1103/PhysRevD.93.013013.
- [31] M. Honda et al. Atmospheric neutrino flux calculation using the NRLMSISE-00 atmospheric model. *Phys. Rev. D*, 92:023004, 2015. doi: 10.1103/PhysRevD.92.023004.
- [32] Particle Data Group et al. Review of particle physics. *Progress of Theoretical and Experimental Physics*, 2022(8):083C01, 2022. doi: 10.1093/ptep/ptac097.
- [33] Q. R. Ahmad et al. Measurement of the rate of $\nu_e + d \rightarrow p + p + e^-$ interactions produced by ^8B solar neutrinos at the sudbury neutrino observatory. *Phys. Rev. Lett.*, 87:071301, Jul 2001. doi: 10.1103/PhysRevLett.87.071301.
- [34] R. Abbasi et al. Calibration and characterization of the IceCube photomultiplier tube. *Nuclear Instruments and Methods in Physics Research Section A: Accelerators, Spectrometers, Detectors and Associated Equipment*, 618(1):139–152, 2010. doi: 10.1016/j.nima.2010.03.102.
- [35] R. Abbasi et al. In situ estimation of ice crystal properties at the South Pole using LED calibration data from the IceCube Neutrino Observatory. *The Cryosphere*, 18(1):75–102, 2024. doi: 10.5194/tc-18-75-2024.
- [36] R. Wendell et al. Prob3++. The Super-Kamiokande Collaboration, . URL <https://github.com/rogerwendell/Prob3plusplus>.
- [37] S. Agostinelli et al. Geant4—a simulation toolkit. *Nuclear Instruments and Methods in Physics Research Section A: Accelerators, Spectrometers, Detectors and Associated Equipment*, 506(3):250–303, 2003. ISSN 0168-9002. doi: 10.1016/S0168-9002(03)01368-8.

- [38] Y. Fukuda et al. Evidence for oscillation of atmospheric neutrinos. *Phys. Rev. Lett.*, 81: 1562–1567, 1998. doi: 10.1103/PhysRevLett.81.1562.
- [39] M. G. Aartsen et al. (IceCube Collaboration). Measurement of atmospheric tau neutrino appearance with IceCube DeepCore. *Phys. Rev. D*, 99:032007, 2019. doi: 10.1103/PhysRevD.99.032007.
- [40] M. G. Aartsen et al. (IceCube Collaboration). Development of an analysis to probe the neutrino mass ordering with atmospheric neutrinos using three years of IceCube DeepCore data. *Eur. Phys. J. C*, 80(9), 2020. doi: 10.1140/epjc/s10052-019-7555-0.
- [41] R. Abbasi et al. (IceCube Collaboration). Measurement of atmospheric neutrino mixing with improved IceCube DeepCore calibration and data processing. *Phys. Rev. D*, 108:012014, 2023. doi: 10.1103/PhysRevD.108.012014.
- [42] S. Yu et al. (IceCube Collaboration). Recent neutrino oscillation results with the IceCube experiment. In *Proceedings of 38th International Cosmic Ray Conference — PoS(ICRC2023)*, volume 444, page 1143, 2023. doi: 10.22323/1.444.1143.
- [43] M. A. Acero et al. (The NOvA Collaboration). Improved measurement of neutrino oscillation parameters by the nova experiment. *Phys. Rev. D*, 106:032004, 2022. doi: 10.1103/PhysRevD.106.032004.
- [44] T. Wester et al. (The Super-Kamiokande Collaboration). Atmospheric neutrino oscillation analysis with neutron tagging and an expanded fiducial volume in Super-Kamiokande I–V. *Phys. Rev. D*, 109:072014, 2024. doi: 10.1103/PhysRevD.109.072014.
- [45] M. Rongen for the IceCube Collaboration. Measuring the optical properties of IceCube drill holes. *EPJ Web of Conferences*, 116:06011, 2016. doi: 10.1051/epjconf/201611606011.
- [46] J. Formaggio and G. Zeller. From eV to EeV: Neutrino cross sections across energy scales. *Reviews of Modern Physics*, 84, 2013. doi: 10.1103/RevModPhys.84.1307.
- [47] A. Garfagnini. Neutrinoless double beta decay experiments. *International Journal of Modern Physics: Conference Series*, 31:1460286, 2014. doi: 10.1142/S2010194514602865.
- [48] F. James. *MINUIT – Function Minimization and Error Analysis*, 1998. URL <https://cds.cern.ch/record/2296388/files/minuit.pdf>.
- [49] C. Jensen. *Controversy and Consensus: Nuclear Beta Decay 1911–1934*. Birkhäuser Basel, 1999. doi: 10.1007/978-3-0348-8444-0.
- [50] P. Kaelo and M. M. Ali. Some variants of the controlled random search algorithm for global optimization. *J. Optim. Theory Appl.*, 130:253–264, 2006. doi: 10.1007/s10957-006-9101-0.

- [51] E. Kearns, T. Kajita, and Y. Totsuka. Detecting massive neutrinos. *Scientific American*, 281(2):64–71, 1999. URL <https://www.jstor.org/stable/26058368>.
- [52] J. Kónya and N. M. Nagy. Chapter 5 - Interaction of radiation with matter. In J. Kónya and N. M. Nagy, editors, *Nuclear and Radiochemistry (Second Edition)*, pages 85–131. Elsevier, second edition, 2018. ISBN 978-0-12-813643-0. doi: 10.1016/B978-0-12-813643-0.00005-6.
- [53] M. F. L’Annunziata. 9 - Cherenkov counting. In M. F. L’Annunziata, editor, *Handbook of Radioactivity Analysis (Second Edition)*, pages 719–797. Academic Press, San Diego, second edition, 2003. ISBN 978-0-12-436603-9. doi: 10.1016/B978-012436603-9/50014-4.
- [54] M. J. Larson. Simulation and identification of non-poissonian noise triggers in the IceCube neutrino detector. Master’s thesis, The University of Alabama, Tuscaloosa, Alabama, 2013. URL <https://inspirehep.net/files/147e9132d1d0245895dc407c4dd7505f>.
- [55] M. Leuermann. *Testing the Neutrino Mass Ordering with IceCube DeepCore*. PhD thesis, RWTH Aachen University, 2018. URL <https://publications.rwth-aachen.de/record/751704/files/751704.pdf>.
- [56] M. Maltoni and A. Yu. Smirnov. Solar neutrinos and neutrino physics. *Eur. Phys. J. A*, 52:87, 2016. doi: 10.1140/epja/i2016-16087-0.
- [57] J. Micallef. *Measurement of atmospheric muon neutrino disappearance with IceCube using convolutional neural network reconstructions*. PhD thesis, Michigan State University, 2022. URL <https://d.lib.msu.edu/etd/50693>.
- [58] A. Ishihara on behalf of the IceCube Collaboration. The Icecube Upgrade - design and science goals. In *Proceedings of 36th International Cosmic Ray Conference — PoS(ICRC2019)*, volume 358, page 1031, 2019. doi: 10.22323/1.358.1031.
- [59] M. Prado Rodriguez on behalf of the IceCube Collaboration. Neutrino mass ordering with IceCube DeepCore. *Phys. Sci. Forum*, 8(1):7, 2023. doi: 10.3390/psf2023008007.
- [60] X. Qian, A. Tan, J. J. Ling, Y. Nakajima, and C. Zhang. The Gaussian CLs method for searches of new physics. *Nuclear Instruments and Methods in Physics Research Section A: Accelerators, Spectrometers, Detectors and Associated Equipment*, 827:63–78, 2016. ISSN 0168-9002. doi: 10.1016/j.nima.2016.04.089.
- [61] A. L. Read. Presentation of search results: the CLs technique. *Journal of Physics G: Nuclear and Particle Physics*, 28(10):2693, 2002. doi: 10.1088/0954-3899/28/10/313.
- [62] J. Schechter and J. W. F. Valle. Neutrinoless double- β decay in $SU(2)\times U(1)$ theories. *Phys. Rev. D*, 25:2951–2954, 1982. doi: 10.1103/PhysRevD.25.2951.
- [63] R. A. Serway and J. S. Faughn. *College Physics, with Physics Now: 6th Edition*. Brooks Cole, 2003.

- [64] C. Sutton. Neutrinos and nucleons. *CERN Courier*, 2014. URL <https://cerncourier.com/a/neutrinos-and-nucleons/>.
- [65] S. Tavernier. *Experimental Techniques in Nuclear and Particle Physics*. Springer Berlin, Heidelberg, 2010. doi: 10.1007/978-3-642-00829-0.
- [66] A. Trettin. *Search for eV-scale sterile neutrinos with IceCube DeepCore*. PhD thesis, Humboldt University of Berlin, 2023. URL https://bib-pubdb1.desy.de/record/603805/files/dissertation_alexander_trettin.pdf.
- [67] J. van Santen. *Neutrino Interactions in IceCube above 1 TeV*. PhD thesis, University of Wisconsin-Madison, 2014. URL <https://inspirehep.net/files/0e3b115636f2c3348eb2ba7970b167ab>.
- [68] S. S. Wilks. The large-sample distribution of the likelihood ratio for testing composite hypotheses. *Ann. Math. Statist.*, 9(1):60–62, 1938. doi: 10.1214/aoms/1177732360.
- [69] J. R. Wilson and the Hyper-Kamiokande Collaboration. The Hyper-Kamiokande experiment. *J. Phys.: Conf. Ser.*, 2156(1):012153, 2021. doi: 10.1088/1742-6596/2156/1/012153.